Influence of biochemical environments on surface fatigue of additive manufactured Ti-6Al-4V

By

Muhammad Qasim Riaz

Submitted in Partial Fulfillment of the Requirements

for the Degree of

Master of Science

in the

Mechanical Engineering

Program

Youngstown State University

December, 2016

Influence of biochemical environments on surface fatigue of additive manufactured Ti-6Al-4V

Muhammad Qasim Riaz

I hereby release this thesis to the public. I understand that this thesis will be made available from the OhioLINK ETD Center and the Maag Library Circulation Desk for public access. I also authorize the University or other individuals to make copies of this thesis as needed for scholarly research.

Signature:

Muhammad Qasim Riaz, Student Date

Approvals:

Dr. Jae Jong Ryu, Thesis Advisor Date

Dr. Virgil Solomon, Committee Member Date

Dr. Kyosung Choo, Committee Member Date

Dr. Salvatore A. Sanders, Associate Dean of Graduate Studies Date

Abstract

Unstable joint lubrication has been identified as a critical factor initiating the wear and corrosion that significantly limits the useful life of joint replacements. It occurs when the healthy synovial fluid is degraded by surgical wound healing and adverse physiological reaction of surrounding tissue against wear and corrosion products of implant materials. It is critical to know mechanical properties of the degraded unhealthy joint fluid to understand the joint implant lubrication. While a large number of studies have been undertaken to characterize the wear and corrosion behavior of artificial joints, the direct influence of biochemical conditions of synovial fluid on joint lubrication and implant surface damage mechanism are still not clearly understood. Titanium alloys are widely used for implant materials in the medical and dental fields because of their superior strength-to-weight ratio, greater ductility, and electrochemical stability compared to other metallic materials. Therefore, the objective is to identify the surface tension and viscosity evolution of unhealthy synovial fluid and implant surface fatigue wear responses.

This master's thesis describes the mechanical property analysis of additive manufactured Ti-6Al-4V samples based on their build orientation and also their mechanical wear analysis in different biochemical environments. In order to achieve this two samples of Ti-6Al-4V were additive manufactured in transversely isotropic and anisotropic surfaces using electron beam melting (EBM). Nanoindentation and microbending tests were performed to

determine their mechanical properties. The results showed higher modulus and hardness values for vertically oriented transversely isotropic sample. Three synovial fluids were then prepared using different concentrations of bovine serum albumin (BSA) and chondroitin sulfate in phosphate buffered saline (PBS). A novel nanoindentation scheme in wet condition was employed to characterize properties of synovial fluids including surface tension and viscosity. The surface tension was observed to decrease and the viscosity to increase with the increase in BSA and chondroitin sulfate. Standard pin on disk tests were conducted on both the Ti-6Al-4V samples in dry conditions and the three synovial fluid mediums. The results were analyzed by measuring the wear using optical profilometry. The results showed the highest wear for dry conditions and the lowest for the synovial fluid with highest concentration of BSA in PBS, with the vertically aligned transversely isotropic sample giving overall lesser wear than the lateral anisotropic sample. Also it was observed that increase in viscosity and decrease in surface tension resulted in lesser wear and better lubrication.

Acknowledgements

I would like to first thank my thesis advisor Dr. Jae Joong Ryu for his endless help and support. He was always there to help and guide me throughout my research even though having his own busy schedule. He sparked my interest to this field of mechanical engineering in the first place and then encouraged me to give it my full. I would also like to thank Dr. Vrigil Solomon and Dr. Kyosung Choo for being in my research committee and revising my work and advising countless times, with a special thanks to Dr. Solomon for also letting me use his lab every time I needed to.

I would particularly thank the Nanovea support team for their help and guidance using the nanoindenter for my research and their support whenever I had any issue with the machine. I also want to thank John Dodson, Laboratory Machinist for his support and help in preparing the equipment for my research whenever I needed.

In the end a special thanks to my family for always having confidence in me. Shout out to my sisters for always believing that nothing is hard for me and that I can achieve anything in my life that I seriously aim for.

Table of Contents

List of Figures

List of Tables

Chapter 1: Introduction

1.1 Hip Joint and its replacement

The hip joint is the body's second largest joint after the knee joint. It is a ball and socket joint between the leg and pelvis. The rounded head of the femur forms the ball that fits into the acetabulum, which is the cup-shaped socket in the pelvis. Ligaments connect the ball to the socket and usually provide tremendous stability to the joint. The bone surfaces of the femoral head and acetabulum have a smooth durable layer of articular cartilage that cushions the ends of the bones and allows for smooth movement [23].

The articular cartilage contains the synovial fluid, which is a thick fluid that cushions bone ends and acts as shock absorber, reduces friction during joint movement in the synovial joints in knees, shoulders, hips, hands, and feet and also acts as a nutrient medium. All of the various components of the joint assist in the mobility of the joint. Damage to any single component can negatively affect range of motion and ability to bear weight on the joint. Hip joint is of particular importance when it comes to the damage and joint replacement as it is the second most replaced joint in the USA by arthroplasty after the knee joint [52]. In a total hip replacement both the thigh bone (femur) and the socket are replaced with artificial hip parts called an implant or prosthesis. The materials used for these implants range from metals to plastics and ceramics.

The viscous-elastic cartilage tissue that covers bone ends accommodates severe impact loadings and shear forces. However, total joint replacement removes the natural articular cartilage and replaces it with a synthetic joint material. It is inevitable to lose a smooth

mobility and wear protection of the artificial joints as it significantly affects the joint synovial fluid. its useful life is seriously restricted due to continuous surface fatigue and corrosion at the joint interface. Wear and fretting corrosion in the artificial joint, particularly with metal-on-metal prostheses, result in the formation of soluble and particulate debris that can migrate in locally or systemically and may induce a cascade of inflammatory events that may ultimately result in bone loss by osteolysis and subsequent implant failure. The adverse tissue reaction lowers pH level and increase protein concentration in the synovial fluid, and therefore the unhealthy joint fluid further impacts the tribological effect on the joint interface. The unstable lubrication seems to increase the friction fatigue on the implant surface and accelerate implant damage. Consequently, it is very important to understand how the metallic implant surface damage is accelerated during the synergistic combination of contact fatigue and environmental corrosion.

Overall there is an increase in the joint damage observed by the changed concentration of the synovial fluid, which includes both the mechanical and chemical effects on the joint. This research focuses on the mechanical effects of the synovial fluid concentration on the wear of the Ti-6Al-4V alloy. A series of experiments were conducted to understand mechanisms of fluid wettability and viscosity with variable biochemical constituents of synovial fluid to elucidate the ultimate synovial lubrication effect on knee joint implant surface damage. The material used for the research is additive manufactured Titanium alloy, Ti-6Al-4V.

1.2 Using Titanium Alloy

Metal-on-metal prostheses have gotten really popular for total hip replacement. It includes metals cobalt chromium alloy, titanium alloy or sometimes stainless steel. Due to their strengths they offer the potential for greatly reduced wear, with less inflammation and less bone loss. However, an unusual damage has been observed in metal prosthesis due to their debris which are the small bits of metal produced when the metal parts rub on each other. They shed into the articular cartilage and bloodstream, which has brought some negative attention to metal-on-metal [33]. But on the other side metal-on-metal implants allow the largest heads throughout the entire range of implant sizes. Large ball heads provide increased range of motion and greater stability, which can significantly reduce the risk of hip dislocation, which is a crucial factor in the long term success of an implant.

Pure titanium and its alloys are now the most attractive metallic materials for biomedical applications. Ti-6Al-4V is the most widespread of those alloys [1]. Due to its chemical and biological inertness its application has been expanded in food industry as well as orthopedic and dental surgery [2]. The major properties of Titanium alloys that make them ideal for biomedical use are biocompatibility, superior strength-to-weight ratio, greater ductility, better fatigue characteristics, electrochemical stability and corrosion resistance The excellent chemical and corrosion resistance of titanium is to a large extent due to the chemical stability of its solid oxide surface layer to a depth of 10 nm [10].

In biomedical applications these alloys are mainly used for substituting materials for hard tissues, therefore fracture and wear of these alloys are amongst the major challenges for their sustainable functioning in the human body. So in this research the mechanical properties and mechanical wear of additive manufactured Ti-6Al-4V samples are analyzed.

1.3 Additive Manufacturing

Additive manufacturing (AM) is the process of making a physical product directly from a Computer Aided Drafting (CAD) model. Direct digital manufacturing technologies have rapidly evolved over the past decade and are gaining applications in aerospace, functional components and biomedical implant manufacturing. Today, manufacturing industries struggle with long lead times and high fixed costs for critically low-volume and highly custom parts. In applications such as custom complex parts such as biomedical implants, where custom parts and fixtures are not readily available, this is a significant challenge. Recent surveys on AM technologies have demonstrated the high probability of adopting AM technologies to significantly increase in all aspects of production and manufacturing industries. Especially, for manufacturing of the total joint replacements (TJR), it is often required to produce a custom-design for optimum anatomic restorations.

Additive Manufacturing (AM) technology has been employed to produce custom total joint replacements (TJRs) that cannot be produced by conventional manufacturing technologies. While AM offers a high geometric flexibility and great potential of cost savings, the additive layered metal deposition results in directionally solidified structure which is undesirable for bearing components of TJRs. Therefore, it is extremely important to identify the direct influence of microstructures on tribo-corrosion behaviors of AM built TJRs. The research objective of this proposal is to acquire fundamental knowledge of tribological response of AM; specifically powder bed fusion based medical grade alloys in biochemical environment. In powder bed fusion, spread layers of powders are selectively melted using an energy source (laser or electron beam). Unlike bulk properties, in order to accurately identify the tribological and chemical behavior of AM built TJR in human body,

we plan to use a multiscale experimental approach. The newly acquired knowledge will precisely describe the relationship between the crystalline orientation and durability and reliability of AM built TJRs. With growing number of studies on the processing and mechanical testing of metal parts manufactured by AM technologies such as Electron Beam Melting (EBM) process and Selective Laser Melting (SLM) have been conducted, the tribological nature and electrochemical response of the surfaces for biomedical applications have not yet been studied. Therefore, this research investigated the influence of the anisotropic microstructures of electron beam AM-made Ti-6Al-4V materials on wear and corrosion resistance in synovial environment. Findings from this research will help understand overall surface damage mechanism of AM-made orthopedic implants under fatigue surface loading and help identify optimal AM build orientation for implants.

1.4 Research Objectives

With the increasing demand for joint replacements and growing challenges in material selection and production, there is a clear need to explore the different material options and their manufacturing methods to find the optimum material. While most of the materials are manufactured by conventional ways for joint replacements, the purpose of this research is to investigate the behavior of additive manufactured titanium alloy for total hip replacement.

Ti-6Al-4V samples were additive manufactured using electron beam melting (EBM) according to ASTM standards. The samples were in two different orientations of horizontal (y-direction) and vertical (z-direction) to analyze the impact of AM process-induced surface anisotropy. First mechanical tests were performed to determine their properties including modulus of elasticity, hardness value and yield strength. These tests included nanoindentation tests and 4-point and 3-point bending tests. Then pin on disk wear tests were performed to compare the tribological response of the samples. The wear tests were then repeated in wet conditions to correlate the concentration of the bodily synovial fluid with the wear response of the samples.

Chapter 2: Material Characterizations

Abstract

Titanium alloys are very commonly being used as biomedical implant materials. They have several qualities which make them compatible for use in biological medium. For a biomechanical use of any material its mechanical properties and strengths play a vital role. The materials have to be in a specific range of moduli and hardness to function properly. In this chapter the mechanical property analyses of the Ti-6Al-4V alloy are discussed.

Mechanical tests are conducted on Ti-6Al-4V samples, additive manufactured in two different orientations. The samples are manufactured using Electron Beam Melting (EBM) in horizontal and vertical orientations. The results are then analyzed by comparing their moduli values from the different types of tests conducted. The results show that the vertically aligned sample shows overall higher modulus and yield strength compared to the horizontally built sample by an average 13.5% and 6.18% respectively.

2.1 Introduction

2.1.1 Titanium Alloy

Pure titanium and its alloys are now the most attractive metallic materials for biomedical applications. Ti-6Al-4V is the most widespread of those alloys [1]. Thanks to its chemical and biological inertness its application has been expanded in food industry as well as orthopedic and dental surgery [2]. The major properties of Titanium alloys making them ideal for biomedical use are biocompatibility, superior strength-to-weight ratio, greater ductility, better fatigue characteristics, electrochemical stability and corrosion resistance. The chemical and corrosion resistance observed in the Titanium and its alloys is largely due to the 10nm deep oxide layer on its surface which has a good chemical stability [10].

Most of the implants done in the bodies are to replace the hard tissues, therefore fracture and wear of these alloys are amongst the major challenges for their sustainable functioning in the human body. These properties of the alloys are greatly affected by changes in their microstructure. Whereas the microstructures are greatly affected by the route of production of the metals so the production process indirectly strongly relate to the mechanical properties of these alloys [1].

Presently most of the Ti-6Al-4V biomedical parts are produced by hot working and machining of wrought semi-products. In those processes the microstructure is determined both by the strain rate and temperature [2]. A newly developed direct digital manufacturing (DDM) involves a process of joining materials making a physical product from a 3D CAD (Computer Aided Drafting) model. This process is known as additive manufacturing (AM) and it has several types.

2.1.2 Additive Manufacturing and Electron Beam Melting

Additive manufacturing (AM) is used to describe the technologies that build 3D objects by adding layer-upon-layer of material, whether the material is plastic, metal, concrete and several other prospective materials. 3D printing is a subset of AM in which the part is created from a computer-aided design (CAD) file by depositing or fusing a layer of material. AM technologies have rapidly evolved over the past decade and gained widespread usage in aerospace, functional components and biomedical implant manufacturing. The major advantages of AM systems include; reduced part development time, lower or no process engineering time, lower material consumption and faster design-to-part production. 3D printable models may be created with a computer-aided design (CAD) package, via a 3D scanner, or by a plain digital camera and photogrammetry software. 3D printed models created with CAD result in reduced errors and can be corrected before printing, allowing verification in the design of the object before it is printed [6].

While the adding of layer-upon-layer approach is simple, there are many applications of AM technology with degrees of sophistication to meet diverse needs including:

- It acts as a visualization tool in design
- It is used to create highly customized products for consumers and professionals alike
- It is used as industrial tooling
- It is used for small scale production parts
- In the future it promises to even produce human organs [7].

The additive manufacturing systems can be classified by the energy source used or the way the material is being joined, for example using a binder, laser, heated nozzle etc. Classification is also possible by the group of materials being processed, such as plastics, metals or ceramics. Significant AM processes for metals are broadly classified into the following two types [8]

1. Powder-bed systems
2. Powder-fed systems

2.1.2.1 Powder-bed systems

Powder-bed systems use a powder deposition method that consists of a coating mechanism to spread a powder layer onto a substrate plate and a powder reservoir. Usually the layers have a thickness of 20 to 100 µm. In this process the powder layer is distributed and a 2D slice is either bound together, known as 3D-Printing, or melted using an energy beam applied to the powder bed. In the second case the energy source is normally one high-power laser [8].

The two main techniques are direct metal laser sintering and selective laser melting.

2.1.2.1.1 Direct Metal Laser Sintering

Direct metal laser sintering involves spreading a very thin layer of metal powder across the surface that is to be printed. A laser is slowly and steadily moved across the surface to sinter this powder. During the sintering process the particles inside the metal are fused together. In this process the metal is not heated enough to allow it to melt completely. One cross section of the product is printed at a time and then additional layers of powder are

then applied and sintered, repeating the process for next layer. In this way, DMLS gradually builds up a 3D object through a series of very thin layers. After all the layers are printed, e the DMLS process is completed and the printed object is left to cool. Excess powder can be recovered from the build chamber and recycled [9].

The major benefit of DMLS is that it produces objects free from the residual stresses and internal defects that are seen in the traditionally manufactured metal components. For the parts being used under high stress, this is a big advantage. Due to being free from any internal stresses the metals made from DMLS don't need to be heat treated like the traditionally made metals. This saves both the cost and time.

However, the major disadvantage with the DMLS is the cost. Due to it being very expensive it has a very limited use, only to very high-end applications. These application includes manufacturing parts for the aerospace industry. Which suits best since the metals are free from any internal stresses and defects as mentioned earlier. However, scientists working at Michigan Technological University have developed a 3D metal printer that costs just $1,500 to build. In comparison, most commercial metal 3D printers cost more than half a million dollars each. The printer is still very early in development; however, this breakthrough could make DMLS technology much more affordable in the future [9].

2.1.2.1.2 Selective Laser Melting

Another method of 3D metal printing is selective laser melting (SLM). The major difference of this from the last process is that in this process the laser beam completely

melts the metal powder. Selective laser melting produces printed objects that are extremely dense and strong [9].

Currently, selective laser melting can only be used with certain metals. The technique can be used for the additive manufacturing of stainless steel, tool steel, titanium, cobalt chrome and aluminum parts. Researchers hope that the SLM will one day be used to manufacture parts made of other metals, but there are difficulties that still need to be resolved. Many other metals do not have the correct flow characteristics that are needed to make them suitable for SLM.

Selective laser melting is a very high-energy process, as each layer of metal powder must be heated above the melting point of the metal. The high temperature gradients that occur during SLM manufacturing can also lead to stresses and dislocations inside the final product, which can compromise its physical properties.

NASA stated that one of the big advantages offered by SLM is that it allows workers to manufacture metal equipment as a whole, rather than having to produce individual components and assemble them to create the final product. For example, the engine injector that was tested in August 2013 was made up of just two parts, compared to 115 parts in a similar injector that was previously tested. Having fewer parts means that complex equipment is easier to assemble [9].

2.1.2.1.3 Electron Beam Melting

Electron beam melting (EBM) is an additive manufacturing process that is very similar to selective laser melting. Like SLM, it produces models that are very dense. The difference

between the two techniques is that EBM uses an electron beam rather than a laser to melt the metal powder [9].

Currently, electron beam melting can only be used with a limited number of metals. Titanium alloys are the main starting material for this process, although cobalt chrome can also be used. The technique is used primarily to manufacture parts for the aerospace industry.

Electron beam melting (EBM) has been successfully established in biomedical engineering applications. Powder bed-based EBM technique uses a high-energy electron beam to selectively melt the metal powder as defined by a CAD model in a vacuum [9].

The electron beam melting machine translates a three dimensional model into several layers, with a thickness of some tens of microns. Each layer is drawn through melting onto a bed of spread out metal powder. The part is then built up layer by layer.

Formerly, a 4 kW electron beam gun pre-heats the powder layer using a relatively low-beam current and a relatively high scan speed. This results in two effects. First of them, the partial sintering of the powder, which holds it in place during the following melting; moreover, the pre-heat reduces the thermal gradient between the just-melted layer and the yet built up body of the part (Cormier et al., 2002). The substantial high-temperature maintenance allows the reduction of residual stresses.

After the melting of a layer, the build plate is lowered by a step equal to one-layer thickness, and another powder layer is spread out and then melted, and the process is repeated in order to obtain the three-dimensional part. Once the build process is completed, the art is blasted

with the same processed powder in order to remove partially sintered particles from the surface [2]

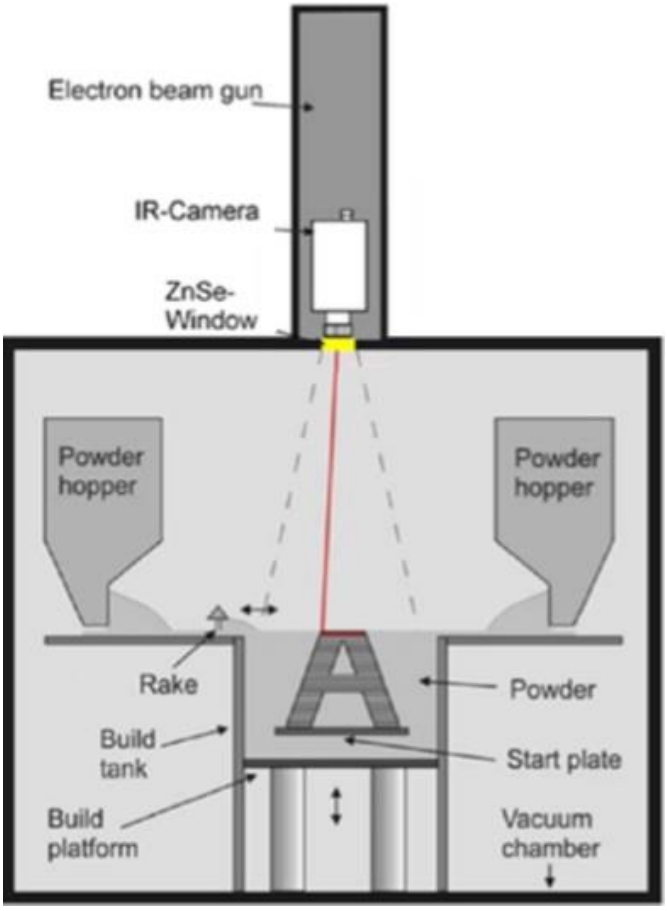

Figure 1: Electron Beam Melting Process [4]

The major advantages of EBM are that it produces extremely dense and strong parts also the process takes place in vacuum build chamber. Using this vacuum minimizes the problems of atmospheric contamination and porosity to a large extent which makes it suited to manufacture parts in reactive materials with a high affinity for oxygen, e.g. titanium [5]. Another main advantage of additive manufacture (AM) is the geometric freedom involved in fabricating components. Due to that complex internal features with graded material compositions can be fabricated without much difficulty [12]. There can be a difference in

part properties with respect to the orientation at which the part has been built [3]. So AM and particularly EBM processing has the potential to control these microstructural features and create orientation-dependent properties that are desired in certain applications and locations [11].

2.1.2.2 Powder-fed systems

The powder-fed system uses the same type of powder raw material like the powder-bed system but the way of adding material to each layer is different. The powder flows through a nozzle being melted from a beam right on the surface of the treated part. Powder-fed systems are also known as Laser Cladding, Directed Energy Deposition and Laser Metal Deposition. The process is highly precise and based on an automated deposition of a layer of material with a thickness varying between 0.1mm and several centimeters. The metallurgical bonding of the cladding material with the base material and the absence of undercutting are some features of this process [8].

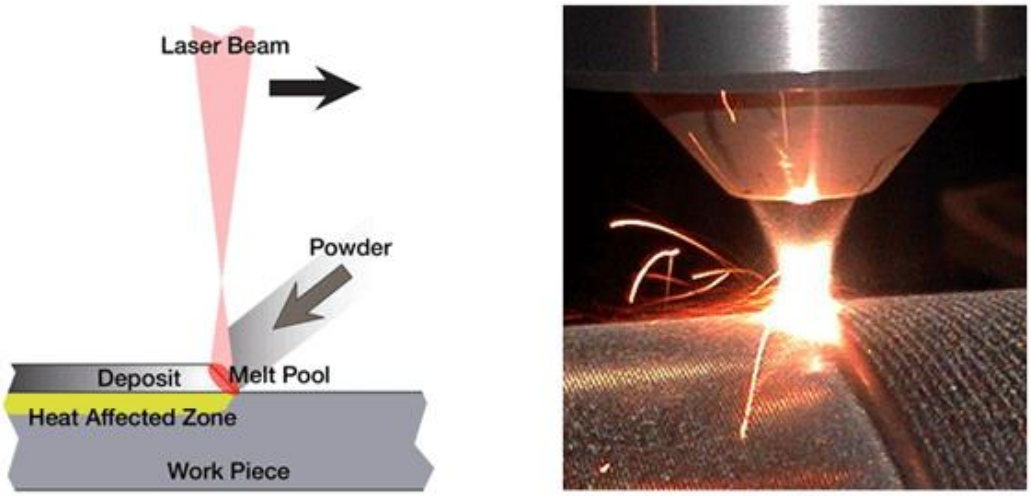

Figure 2: Laser cladding process [8]

The overall comparison of these methods is given in the table below.

Table 1: Comparison of common AM methods for metals [13]

	Laser Beam Melting	Electron Beam Melting	Powder-fed system
Max size (mm)	630 x 400 x 500	dia. 350 x 380	900 x 1500 x 900
Layer Thickness (µm)	30 – 60	50	130 – 600
Min Wall thickness (mm)	0.2	0.6	0.6
Accuracy (mm)	± 0.1	± 0.3	N/A
Build rate (cm^3/h)	5 – 20	80 – 100	2 – 30
Surface roughness (µm)	5 – 15	15 – 20	15 – 20
Geometric limitations	Supports needed everywhere (thermal anchorage)	Less supports but powder sintered	No powder bed. Same limitations as 5 axes milling
Materials	Stainless steel, tool steel, titanium, aluminum, ceramics	Only conductive materials (Ti6Al4V, CoCr, TiAl, Tool steel, Cu alloy)	Steel, Ti, Ni-base alloys, composites, ceramics
Energy source	Laser	Electron Beam	Laser
Cost efficiency	Poor	Medium	Good
Residual Stress	High	Low	Medium
Part complexity	High	Medium	Low
Typical applications	Tooling, implants, all meta type components	Implants, Near-net-shape manufacturing	Near-net-shape manufacturing, shafts, ducts etc.

2.1.3 Mechanical Testing

Samples of engineering materials are subjected to a wide variety of mechanical tests to measure their mechanical properties and behavior. This involves applying some type of force and measuring some kind of response. Mechanical testing reveals the properties such as elasticity, tensile strength, elongation, hardness, yield strength, fracture toughness, impact resistance, stress rupture and the fatigue limit when force is applied dynamically or statically. The results of such tests are used for two primary purposes [14]:

1) Engineering design, which is to determine the mechanical behaviors of the materials in conditions of their final applications
2) Quality control, to check that the raw material is being produced to a required standard either by the materials producer or by the end user.

Some common forms of test specimens and loading situations are shown in Fig 3.

Out of these types, indentation hardness testing, 4-point bending and 3-point bending are performed on the samples. These are explained as follows.

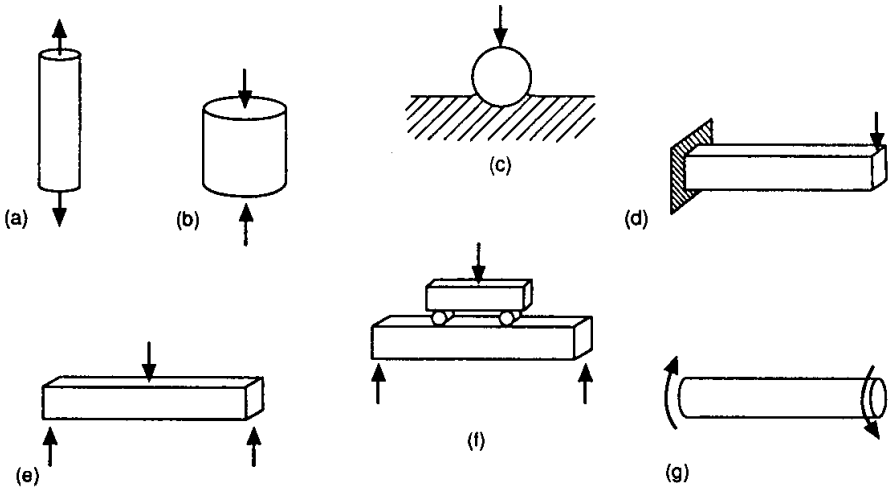

Figure 3: Typical Mechanical loading situations [14]

a) tension, b) compression, c) indentation hardness, d) cantilever flexure, e) three-point flexure, f) four-point flexure and g) torsion

2.1.3.1 Nanoindentation Test

Nanoindentation is based on the standards for instrumented indentation, ASTM E2546 and ISO 14577. It uses an established method where an indenter tip with a known geometry is driven into a specific site of the material to be tested, by applying an increasing normal load. When reaching a pre-set maximum value, the normal load is reduced until complete relaxation occurs. The load is applied by a piezo actuator and the load is measured in a controlled loop with a high sensitivity load cell. During the experiment the position of the indenter relative to the sample surface is precisely monitored with high precision capacitive sensor.

Nanoindentation tests are mostly performed to determine the elastic modulus and hardness of a material and in some cases to determine the yield strength. Conventional

indentation hardness tests involve the measurement of the size of a residual plastic impression in the specimen as a function of the indenter load. This provides a measure of the area of contact for a given indenter load. In a nanoindentation test, the size of the residual impression is often only a few microns and this makes it very difficult to obtain a direct measure using optical techniques. In nanoindentation testing, the depth of penetration beneath the specimen surface is measured as the load is applied to the indenter. The known geometry of the indenter then allows the size of the area of contact to be determined. The procedure also allows for the modulus of the specimen material to be obtained from a measurement of the "stiffness" of the contact, that is, the rate of change of load and depth [15].

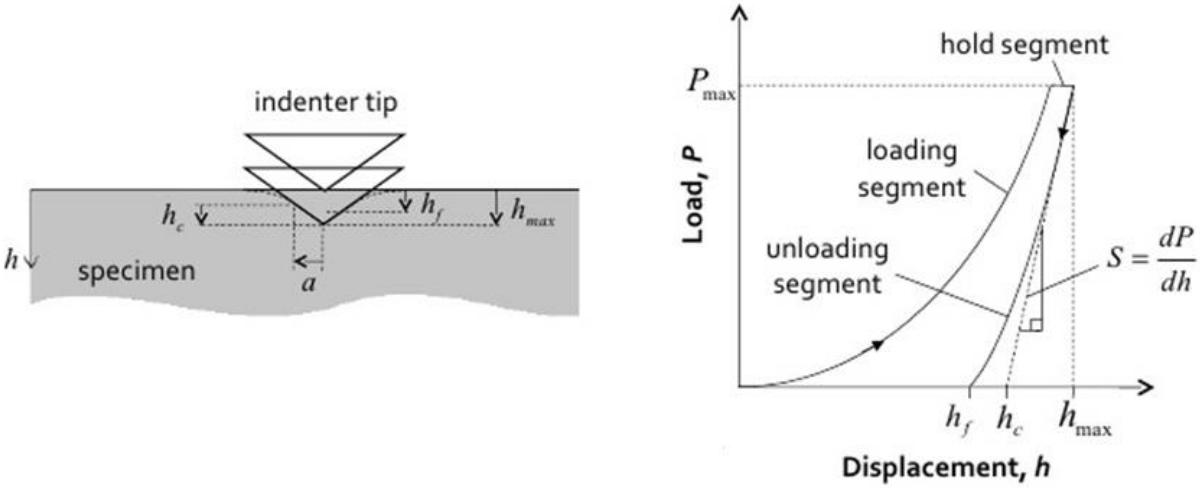

Figure 4: Nanoindentaion schematic with Load-depth curve

2.1.3.1.1 Indentation Hardness and Modulus

A particularly meaningful quantity in indentation hardness in the mean contact pressure of the contact, and is found by dividing the indenter load by the projected area of the contact. The mean contact pressure, when determined under conditions of a fully developed plastic zone, is usually defined as the indentation hardness, H of the specimen material. In nanoindentation testing, the displacement of the indenter is measured and the size of the contact area (at full load) is estimated from the depth of penetration with the known geometry of the indenter. For an extreme case of a rigid-plastic solid, where there is little elastic recovery of material, the mean contact pressure at a condition of a fully developed plastic zone is a true representation of the resistance of the material to permanent deformation. When there is substantial elastic recovery, such as in ceramics where the ratio of E/H is low, the mean contact pressure, at a condition of a fully developed plastic zone, is not a true measure of the resistance of the material to plastic deformation but rather measures the resistance of the material to combined elastic and plastic deformations. The distinction is perhaps illustrated by a specimen of rubber, which might deform elastically in an indentation test but undergo very little actual permanent deformation. In this case, the limiting value of mean contact pressure (the apparent indentation hardness) may be very low but the material is actually very resistant to permanent deformation and so the true hardness is very high.

In depth-sensing indentation techniques used in nanoindentation, the elastic modulus of the specimen can be determined from the slope of the unloading of the load-displacement response as shown in Fig 4. The modulus measured in this way is formally called the indentation modulus, E of the specimen material. Ideally, the indentation modulus has

precisely the same meaning as the term elastic modulus or Young's modulus but this is not the case for some materials. The value of indentation modulus may be affected greatly by material behavior (e.g. piling-up) that is not accounted for in the analysis of load-displacement data. For this reason, care has to be taken when comparing the modulus for materials generated by different testing techniques and on different types of specimens [15].

2.1.3.1.2 Load – displacement curves

In a typical test, force and depth of penetration are recorded as load is applied from zero to some maximum and then from maximum force back to zero. If plastic deformation occurs, then there is a residual impression left in the surface of the specimen. Unlike conventional indentation hardness tests, the size (and hence the projected contact area) of the residual impression for nanoindentation testing is too small to measure accurately with optical techniques. The depth of penetration together with the known geometry of the indenter provides an indirect measure of the area of contact at full load, from which the mean contact pressure, and thus hardness, may be estimated. When load is removed from the indenter, the material attempts to regain its original shape, but it prevented from doing so because of plastic deformation. However, there is some degree of recovery due to the relaxation of elastic strains within the material. An analysis of the initial portion of this elastic unloading response gives an estimate of the elastic modulus of the indented material. The form of the compliance curves for the most common types of indenter are very similar and is shown in Fig. 8.

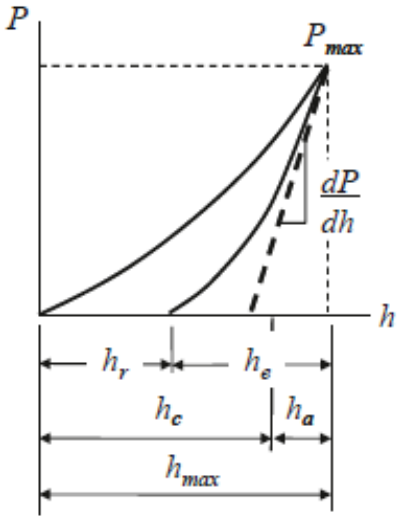

Figure 5: Load-displacement curve of sample nanoindentation test [15]

2.1.3.1.3 Berkovich Indenter

The Berkovich indenter is used routinely for nanoindentation testing because it is more readily fashioned to a sharper point than the four-sided Vickers geometry, thus ensuring a more precise control over the indentation process. The mean contact pressure is usually determined from a measure of the contact depth of penetration, hc in (see Fig.4), such that the projected area of the contact is given by:

$$A = 3\sqrt{3}\, h_c^{\,2}\, tan^2\theta \qquad (1)$$

For Berkovich $\theta = 65.27^{O}$, so

$$A = 24.494\, h_c^2 \qquad (2)$$

So the mean contact pressure is:

$$H = \frac{P}{24.5\ {h_c}^2} \tag{3}$$

The expected relationship between load and depth for an elastic-plastic contact is given by:

$$h = \sqrt{P}\left[(3\sqrt{3}\,H\,tan^2\theta)^{-\frac{1}{2}} + \left[\frac{2\,(\pi-2)}{\pi}\right]\frac{\sqrt{H\,\pi}}{2\,\beta\,E^*}\right] \tag{4}$$

Upon elastic unloading we have:

$$h = \sqrt{P}\,\left(\frac{\pi}{2\,E^*}\right)^{\frac{1}{2}}\left(\frac{\pi}{3\sqrt{3}}\right)^{\frac{1}{4}}\frac{1}{tan\,\theta'} \tag{5}$$

The indentation modulus is determined from the slope of the unloading curve at the maximum load. That is given by

$$E^* = \frac{1}{2}\,\frac{\sqrt{\pi}}{\sqrt{A}}\,\frac{d\,P}{d\,h} \tag{6}$$

where

$$\frac{1}{E_r} = \frac{1-\nu^2}{E} + \frac{1-\nu_i^2}{E_i} \tag{7}$$

2.1.3.1.4 Yield Strength Measurement

The yield strength (YS) is the stress at which a material begins to deform plastically and will not returns to its original shape when the applied stress is removed. In practical applications it indicates the upper limit to the load that can be applied to mechanical parts and structure, and play important roles in materials production including annealing, forging, rolling and pressing [16].

Traditionally the YS and ultimate tensile strength (UTS) have been tested using a tensile testing machine, a large instrument requiring enormous strength to pull apart the test specimen. It is both costly and time-consuming to properly machine many test coupons for a material – each sample can only be tested once. Small defects in the sample could possibly create noticeable variance in the test result. The different configuration and alignment of the tensile testers in the market often result in substantial variations in the mechanics of testing and their outcomes. Modern indenters directly provide the YS and UTS values comparable to that measured by conventional tensile tests. This measurement opens up a whole new realm of possibilities for all industries. The simple experimental setup significantly cuts the time and cost for sample preparation, compared to the coupons with a complex shape for tensile tests. The small indentation size makes it possible to perform multiple measurements on one single sample. It can prevent the influence of defects in the tensile test coupons created during sample machining. Moreover, it allows YS measurements on small samples and localized areas, vital for YS mapping and local defect detection of pipelines or auto structure [16].

The YS/UTS tests are performed on the same nanoindenter as the hardness test. During the indentation test, a cylindrical flat tip with a known surface area is used as the indenter.

Unlike the hardness test for the YS determination the yielding part of the loading portion of the load – displacement curve is taken. After reaching a preset maximum value, the normal load is reduced until partial or complete relaxation occurs. This procedure is repeated using different initial loads and depth versus load is recorded. The resulting curve showing the change from increasing slope to decreasing slope is related to the load at which plastic deformation occurs. This load over area of contact gives the yield strength of the material [17].

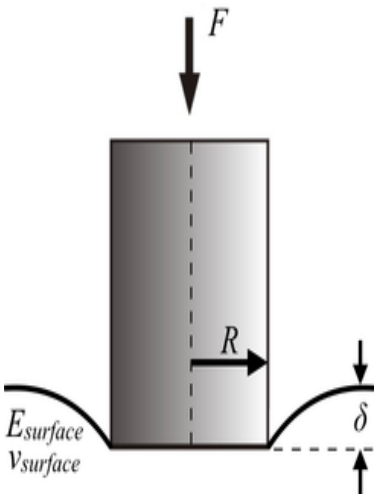

Figure 6: Yield strength indentation test with cylindrical flat tip

A typical load displacement curve using a cylindrical flat tip is shown in figure 9. The inflection point of the first derivative, or a change from positive to negative of the second derivative, corresponds to the measured yield point. Physically, as the load increases, the local roughness is squeezed, and the sample is squeezed down more slowly (because of the flat surface) as the depth increases. As the yield point is reached, the flat tip starts penetrating at increased speed because the supporting load capacity of the material has

been passed [17]. Using the following equation, the yield strength of the sample is determined:

$$\sigma_y = \frac{4P}{\pi d^2} \tag{8}$$

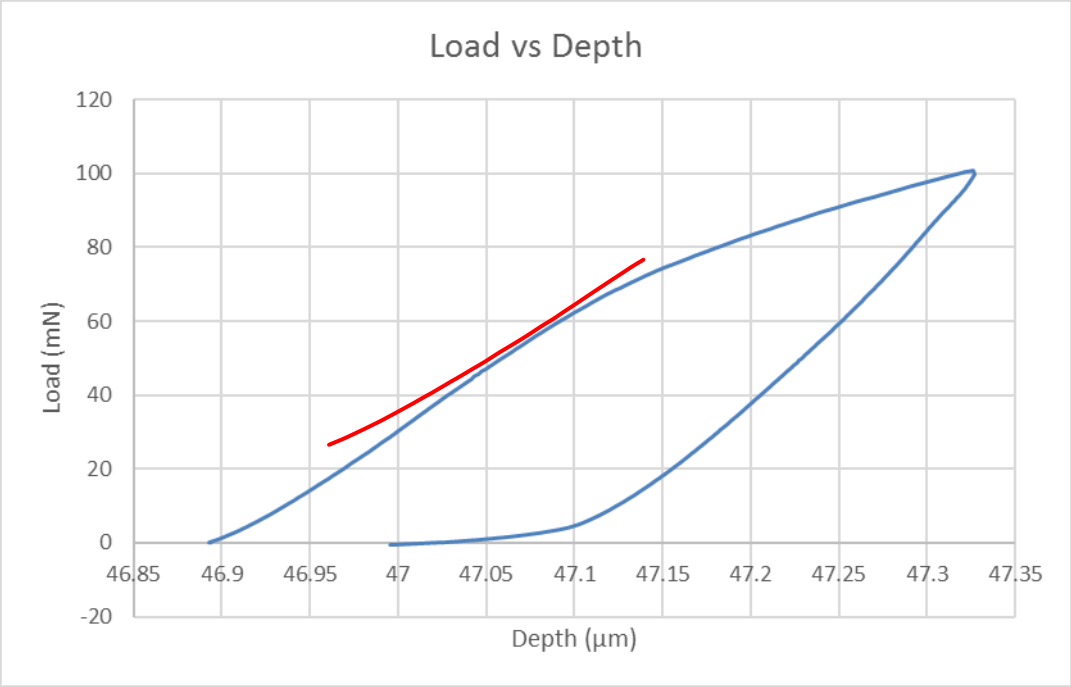

Figure 7: Load-displacement curve of nanoindentation of bulk Ti-6Al-4V with cylindrical flat tip

This technology now permits a more precise yield strength measurement through nano or microindentation. The method provides the precision needed to allow yield strength measurement of micro-sized localized areas, small and diverse-shaped samples, as well as coatings and films. Yield strength measurement has never been easier, more precise, or more capable of precise results [17].

2.1.3.2 Three Point bending test

Bend testing (also flex or flexural testing) is commonly performed to measure the flexural strength and modulus of all types of materials and products. This test is performed on a universal testing machine (tensile testing machine or tensile tester) with a 3 point or 4-point bend fixture.

There are several good reasons why the three-point-bend test is used extensively in material characterization: economy, simplicity of specimen preparation and testing, ease of adaptability to environmental testing, suitability for cyclic loading and fatigue testing, convenience for fracture toughness studies, and the availability of well documented simple formulas for analyzing materials having equal tension and compression properties. Another important reason is that the three-point-bend test is a simple way to subject a specimen to tension, compression, and shear simultaneously. In this sense, a three-point-bend test provides a direct measure of the structural integrity of the material [20].

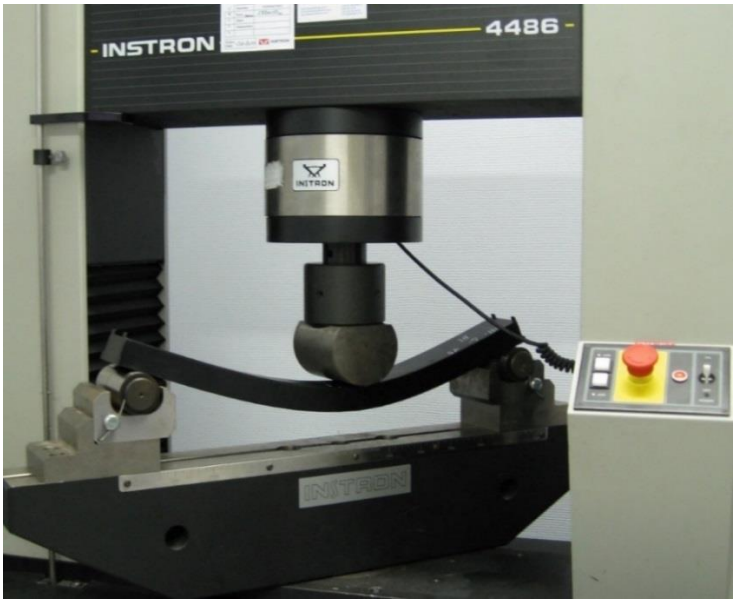

Figure 8: Flexural test with 3-point loading [21]

A flexure test produces tensile stress in the convex side of the specimen and compression stress in the concave side. This creates an area of shear stress along the midline. To ensure the primary failure comes from tensile or compression stress the shear stress must be minimized. This is done by controlling the span to depth ratio; the length of the outer span divided by the height (depth) of the specimen. For most materials S/d=16 is acceptable. Some materials require S/d=32 to 64 to keep the shear stress low enough [19].

The key analysis when performing bend testing are [18]:

(i) Flexural Modulus – This measures the slope of a stress / strain curve and is an indication of a material's stiffness

(ii) Flexural Strength – This measures the maximum force that a material with withstand before it breaks or yields. Yield is where you have pushed a material past its recoverable deformation and it will no longer go back to the shape it once was.

(iii) Yield Point – The yield point is the point where the material essentially "gives up" or the point where if you were to continue to bend the product, the force will not continue to increase and will then start to decrease or break.

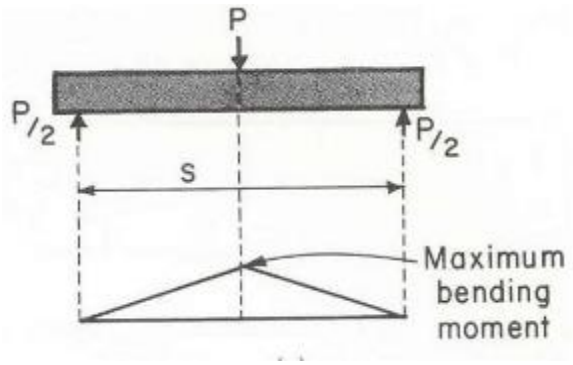

Figure 9: Bending moment in sample in 3-point bending [19]

$$\sigma_{max} = \frac{3\,P\,S}{2\,b\,h^2} \tag{9}$$

$$\delta_c = \frac{P\,S^3}{48\,E\,I} \tag{10}$$

$$I = \frac{b\,h^3}{12} \tag{11}$$

2.1.3.3 Four Point bending test

The 4-point flexural test measures the force required to bend a plastic beam under a four-point loading system. The test method is used for reinforced or unreinforced materials including high modulus composites and for materials that do not fail within the limits of ASTM D790 (a three-point loading test). The major difference between the three point and four point flexural tests is the location of the bending moment. The four-point bending method allows for uniform distribution between the two loading noses, whilst the three-point bending method's stress is located under the loading nose.

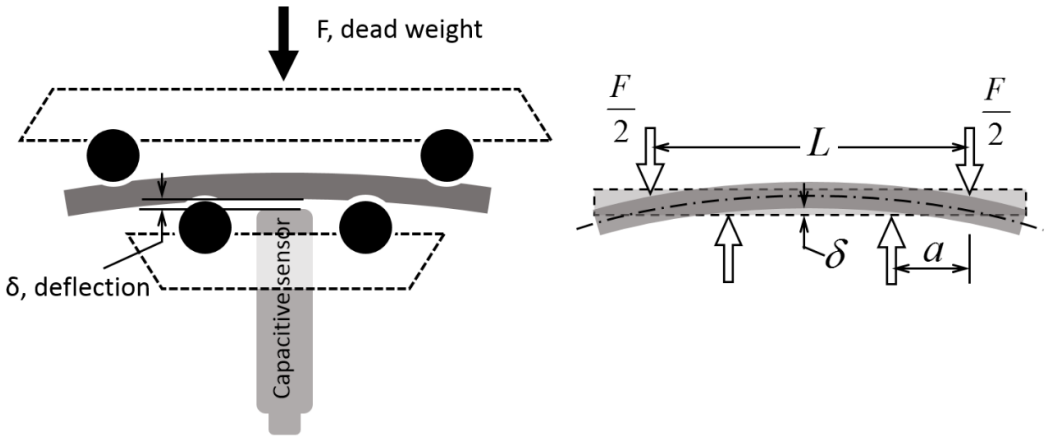

Figure 10: 4-point bending test

Measuring the applied dead loads F and the corresponding deflections in the beam specimen δ, a linear relationship is to be observed within the elastic limit of the specimen. After determining the slope, m of the straight line the following relations are used to determine the modulus of the specimen:

$$F = m\,\delta \tag{12}$$

$$E = m\,\frac{a^2(3L-4a)}{12\,I} \tag{13}$$

2.2 Materials and Methods

2.2.1 Materials

The material used in the research was a titanium alloy, Ti-6Al-4V. The material was additive manufactured using standard electron beam melting (EBM) print parameters (layer thickness of 50µm with powder size distribution of 45 - 106µm) using Arcam Q10.

Table 2: Ti-6Al-4V chemical composition [36]

Element	Percentage weight composition
Aluminum, Al	6%
Vanadium, V	4%
Carbon, C	0.03%
Iron, Fe	0.10%
Oxygen, O	0.15%
Nitrogen, N	0.01%
Hydrogen, H	0.00%
Titanium, Ti	~89.7%

The selected particle size led to ideal process and optimum microstructure. Studies on the microstructure of EBM built Ti-6Al-4V have reported superior microstructure compared to cast Ti-6Al-4V. Microstructures of EBM built Ti-6Al-4V contained a lamellar α-phase with larger β-grains, and with a higher density and significantly finer grain. The chemical composition of the alloy as given by the manufacturer is shown below in Table 2 [36].

2.2.2 Build

For the research to determine the process induced anisotropic properties of Ti-6Al-4V there were two sets of samples manufactured. Two sets of samples, lateral and vertical are based on the direction of layer deposition of EBM process. They are named as EBM-x and EBM-z for the samples with layers being deposited on the side and one above the other respectively.

This results in the sample EBM-x to have anisotropic layers. That shows different mechanical properties in the two axes of x and y. Whereas the sample EBM-z has isotropic layers showing similar mechanical properties in both the axes on the deposited layer. The samples are shown in the following figure:

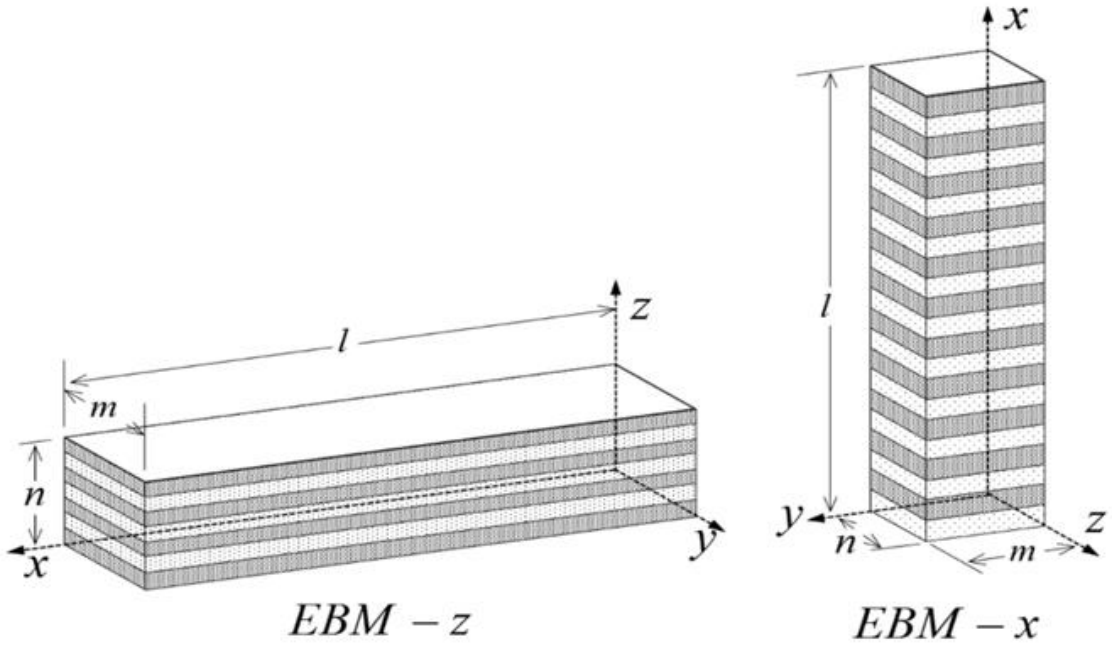

Figure 11: Ti-6Al-4V, EBM-x and EBM-z samples, l = 50mm, m=n=2.5mm

2.2.3 Mechanical Testing

In order to understand the effect of build orientations of EBM process on systemic and local properties, a variety of mechanical tests were performed. For local property measurements the sample surfaces were mirror finished. The test environment was controlled to maintain consistent test conditions at the temperature 25 ± 3 °C and the humidity 27 ± 3 %.

2.2.3.1 Preparation of samples

The samples taken from the manufacturer were inspected for any defects and dimensional errors. After that the samples were prepared for testing by metallographic sample preparation [37]. It was done by grinding and polishing the samples on a Planopol-2 polishing table using different grade polishing papers.

The process started with rough polishing with a 180 grit paper to make the surface flatter and then with 320, 800, 1000, 2400 and 4000 grit papers. During the polishing the samples were rotated 90^{o} to remove the scratches produced during the polishing to achieve a near mirror finish. After that final polishing was done using Chemomet micro fiber with 0.05 µm silica suspension. In the end the samples were cleaned with chemicals. The samples were thoroughly sonicated in acetone, methanol and distilled water to clear the surface from the residues. After finalizing the sample surfaces, they were inspected under a microscope before performing the tests.

2.2.3.2 Nanoindentation testing

Nanoindentation tests were performed on both EBM-x and EBM-z samples in the nanoindentation lab in Youngstown State University. The tests were performed using a

nano-module M1 indenter from Nanovea. The tests were performed using a standard Berkovich indenter and a cylindrical flat tip indenter for hardness and yield strength tests respectively.

2.2.3.2.1 Berkovich indenter

The standard Berkovich indenter was used to perform the hardness analyses on the EBM-x and EBM-z samples. The test parameters used were according to ASTM E2546 and ISO14577 [38] as described in the table below:

Table 3: Nanoindentation test parameters

Parameter	Value
Peak load	140 mN
Loading rate	160 mN/min
Unloading rate	160 mN/min
Creep time	0 sec

A total of 9 indentation tests were performed using Berkovich indenter on randomly selected areas of each sample. The load-displacement curves of the tests were examined and the unloading curve of the load-displacement was used to determine indentation stiffness (slope of load-displacement curve during unloading process). The elastic modulus was determined from indentation stiffness and the hardness was found using the force per projected area relation ASTM E2546 [38]. The values were inspected and the mean of all 9 values was calculated for each the elastic modulus and hardness values for both the samples and taken as final results. The elastic modulus and hardness values were compared for the samples and the reported values.

2.2.3.2.2 Cylindrical flat tip indenter

After the nanoindentation hardness test, yield strength tests were performed. The yield strength is also determined using the nanoindentation test on the same ASTM E2546 and ISO14577 standards [38].

For that a cylindrical flat tip indenter was used on the samples. The test was performed with the following parameters.

Table 4: Nanoindentation test parameters

Parameter	Value
Indenter diameter	5 µm
Peak load	50 mN
Loading rate	160 mN/min
Unloading rate	160 mN/min
Creep time	0 sec

Unlike the hardness test, for yield strength the loading part of the test is of primary importance, since the material starts to yield during loading. The software exported the force and depth values for the test. The yield point is the point of maximum slope in the loading part of the load-depth curve. This point of inflexion corresponded to a load value close to 20mN for both the samples. So the stress values were calculated by using the force per unit area relation. These stress values were the yield strengths of the samples.

2.2.3.3 Microbending testing

The nanoindentation test was used to determine the nano-scale elastic modulus and indentation hardness of the samples. After that micro-scale bending tests were performed to determine the overall elastic modulus of the samples. The microbending tests involved applying measured loads on both the samples and measuring the resulting displacement in the form of bending. Using that the modulus of elasticity was determined.

There were two types of bending tests performed on both the samples.

i. 4-point bending

ii. 3-point bending

2.2.3.3.1 4-point bending

The 4-point bending was used to determine the bulk modulus of elasticity of both the EBM-x and EBM-z samples. The experiment was set up in the lab in Youngstown State University

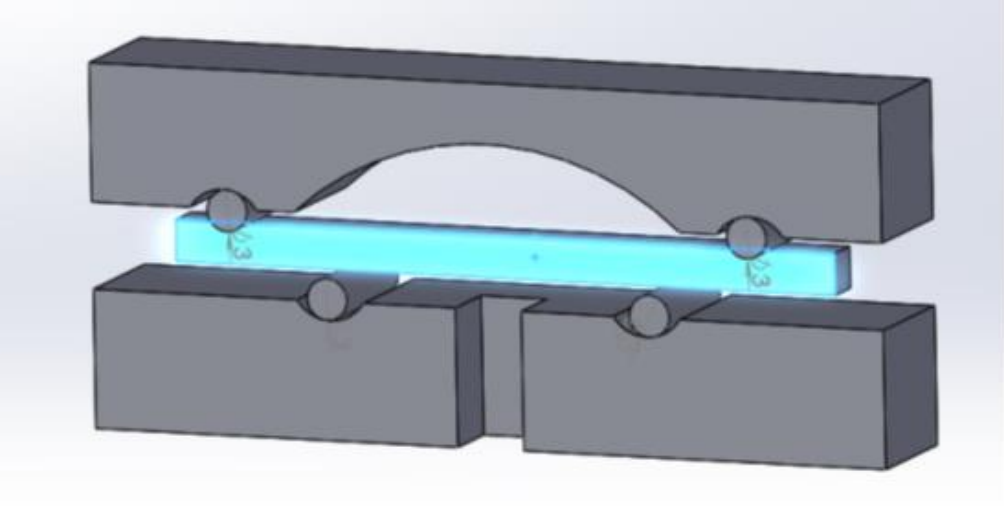

.

Figure 12: 4-point bending experiment setup

The parts used in the setup were made on campus, in the machine shop of the engineering department. The dimensions of the parts were pre-calculated based on the deflections using the expected values of the modulus of elasticity in the Stoney's bending equation. The force values were also estimated for the calculation to have them in the safe range. The parts were milled with an allowance of 1.5mm. After making the parts were inspected and made ready for the tests.

The following image shows the schematic of the 4-point bending test.

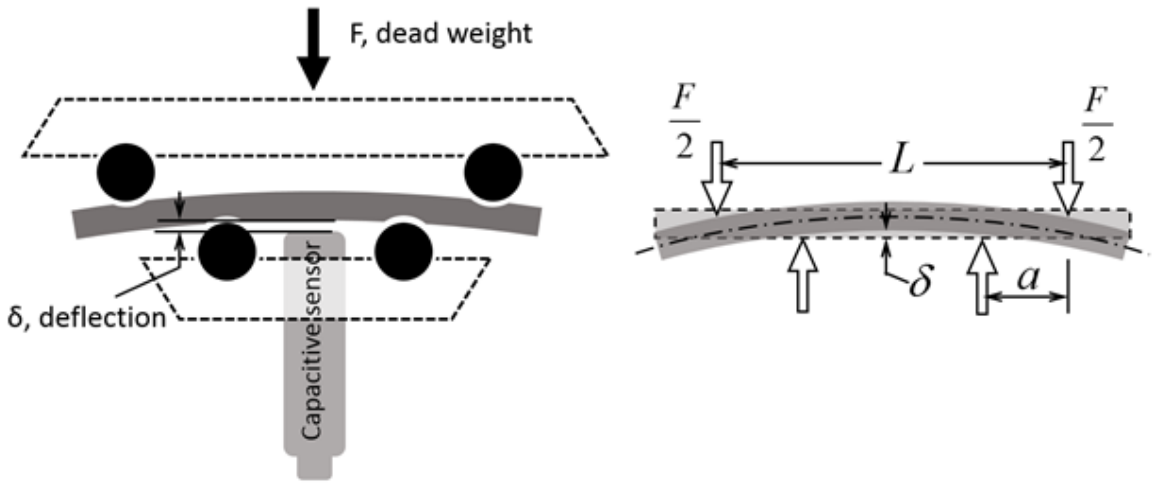

Figure 13: 4-point bending schematic

There were 2 sets of both top and bottom parts made for the 4-point bending experiment, with different distance between the notches. It allowed for 2 settings with different values for 'L' and 'a' to perform the experiment several times to get more accurate results.

Table 5: 4-point bending part parameters

First set up	L_1	35 mm
	a_1	5.5 mm
Second set up	L_2	40 mm
	a_2	8 mm
	Roller diameter	4 mm

For measuring the deflection, a MicroSense capacitive sensor was used. It included a MicroSense model 2807 passive capacitive probe with 1mm diameter sensor with range ±100 µm and a MicroSense model 4810 passive gauging module with ±15V DC power supply. The sensor was installed at the center of the bottom part. This sensor measured the displacement in terms of voltage so there was a need for a relation to convert the voltage value into displacement. For that a test was setup using the MicroSense sensor and the Nanovea nanoindenter. The indenter was moved a measured distance in the vertical direction above the sensor and the corresponding voltage value was measured from a connected voltmeter. This was repeated for several other values to get a set of values of the displacement and their corresponding voltages. These values were used to make a plot on excel and the straight line equation was found.

The 4-point bending test was then performed using different loads and measuring their corresponding deflections. This test was performed a total of 3 times on each sample with each of the set of parts mentioned above. So a total of 12 tests were performed with 6 on each sample. From the measurements a load-deflection plot was made for each case. The slope was calculated and the Stoney's Bending equation was used to determine the moduli of elasticity of the samples.

2.2.3.3.2 3-point bending

3-point bending tests were performed to determine the mechanical properties including the elastic modulus of the EBM-x and EBM-z samples. This test was performed on an Instron 4206 universal testing machine with a 150 kN load cell set in an Instron 5500R mounting. In order to control, record, and export necessary data, Instron's Bluehill 3 software was used. The support rollers were kept at a distance of 1.5in. The test was performed upto a load of 140 N. The software measured the deflection in the sample and its corresponding force values. This test was performed on a total of 3 of each of EBM-x and EBM-z samples.

A set of values for the whole test was exported out of the software. It was used to create a plot on excel. The slope of the straight elastic part of the curve was taken and used to determine the flexural elastic modulus of the samples. In the end the mean of all the tests of each of the samples was taken as the final result of the test.

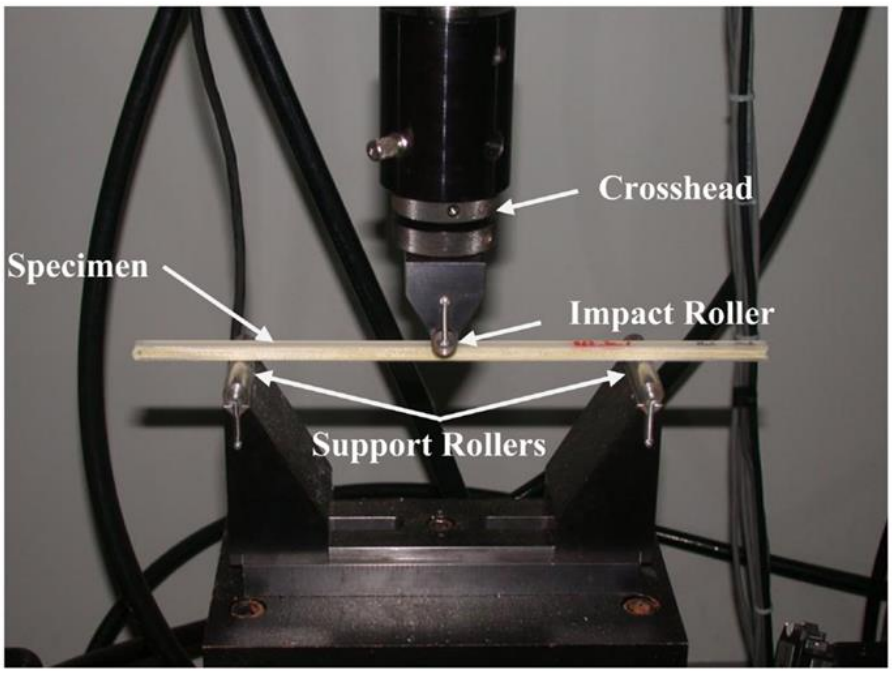

Figure 14: Instron 3-point bending setup [40]

2.3 Results and Discussion

2.3.1 Nanoindentation tests

The series of nanoindentation hardness tests performed on the EBM-x and EBM-z samples gave the following load-depth curves.

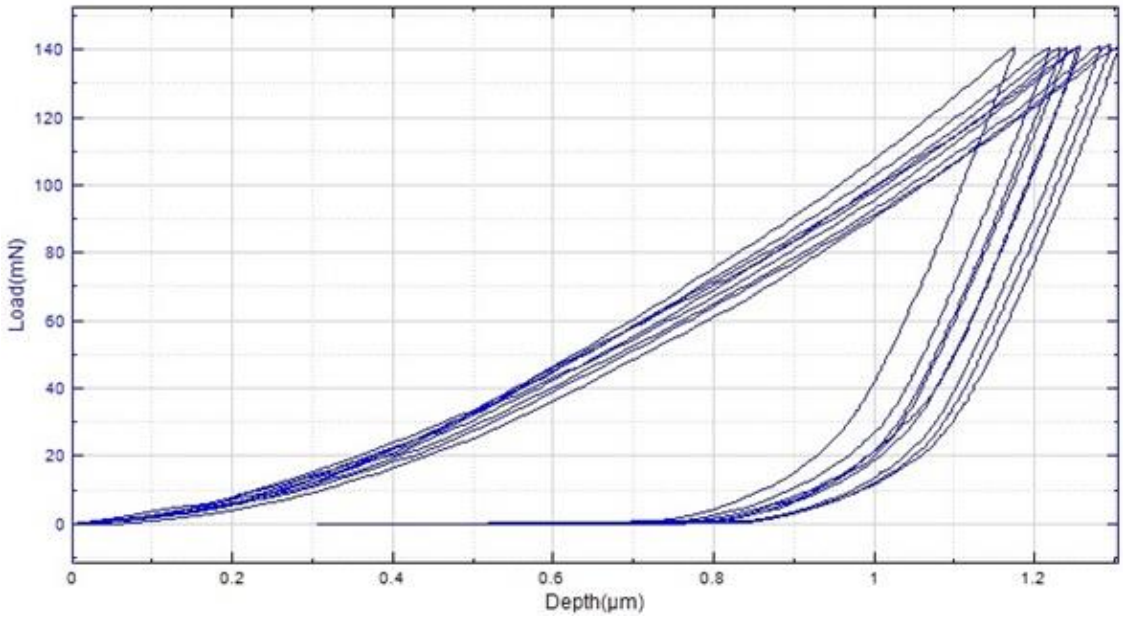

Figure 15: First set of hardness tests EBM-x

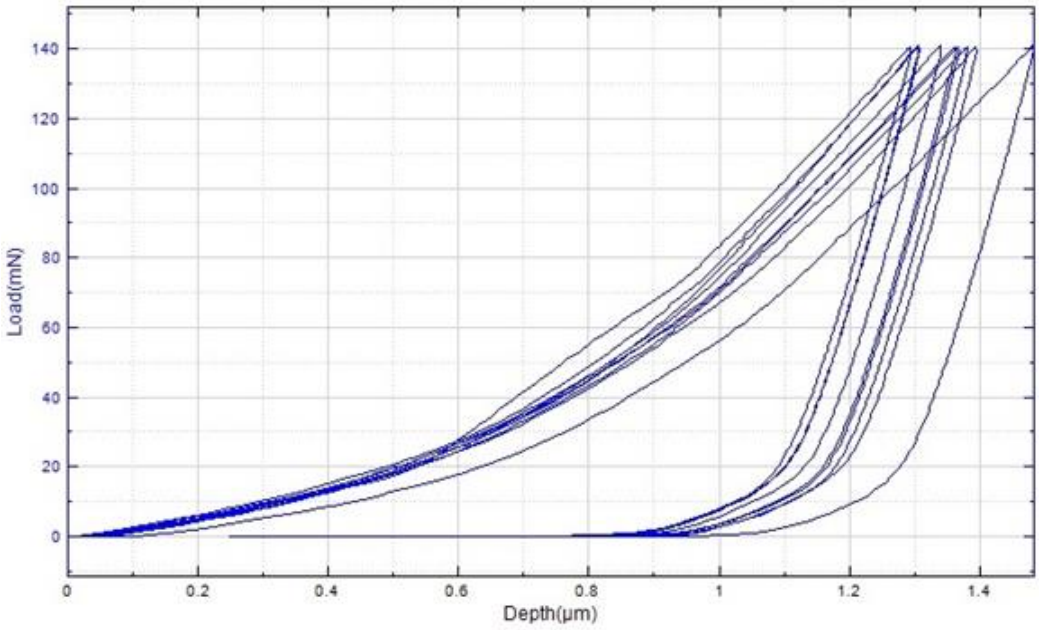

Figure 16: Second set of hardness tests EBM-x

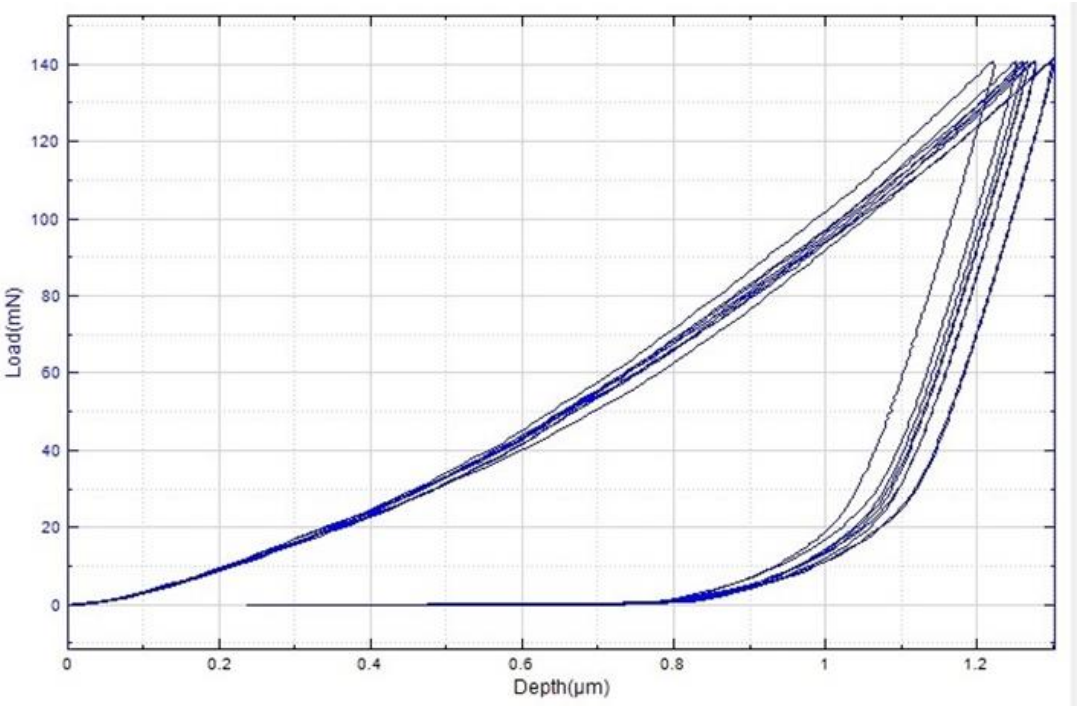

Figure 17: First set of hardness tests EBM-z

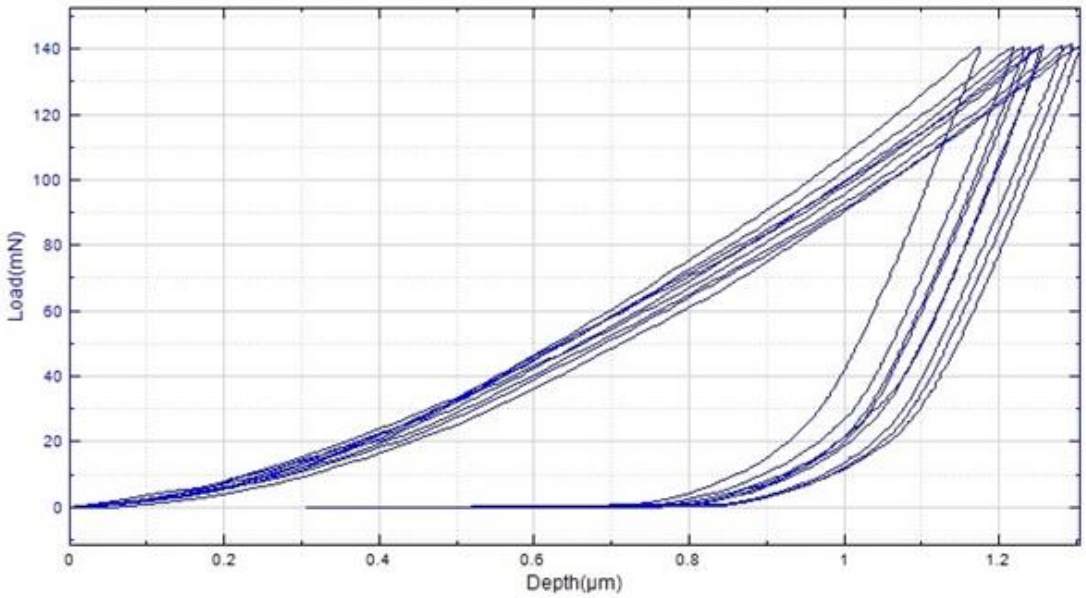

Figure 18: Second set of hardness tests EBM-z

The above curves were directly extracted from the Nanovea Nanoindetation software. Based on these curves the software calculated the elastic moduli and hardness values for the samples. These values are shown in the tables below, for both EBM-y and EBM-z samples for all the 9 tests performed at two different locations. In the end the averages of all the values for each of the EBM-y and EBM-z samples were calculated as the final results. These results are shown in the following table along with the standard deviations of the average values calculated.

Table 6: Elastic Modulus for EBM-x and EBM-z samples (GPa)

	EBM-x		EBM-z	
	Set 1	Set 2	Set 1	Set 2
Test 1	104.25	114.73	117.91	133.26
Test 2	114.89	108.98	124.12	143.46
Test3	110.381	113.98	116.06	126.76
Test 4	95.65	106.56	114.81	128.86
Test 5	102.16	106.86	116.11	119.33
Test 6	94.75	113.55	120.26	129.44
Test 7	102.425	107.82	114.71	128.73
Test 8	101.89	98.46	117.69	124.6
Test 9	103.48	108.21	118.17	127.68
Average	103.32	108.79	117.76	129.13
SD	5.97	4.73	2.8	6.2

So the overall values for the EBM-y and EBM-z are given below

Table 7: Comparison between EBM-x and EBM-z samples modulus values

	EBM-x	**EBM-z**	**Percentage difference**
Elastic Modulus (GPa)	106.05	123.43	+16.38% (EBM-z)
SD (GPa)	7.62	6.8	

From the results it is seen that the EBM-z has a higher elastic modulus value compared to the EBM-x sample by 16.3%.

2.3.2 4-point bending

After the nanoindentation tests performed the samples were prepared for the mircobending tests. First the 4-point bending tests were performed. Before performing these tests, the MicroSense capacitive sensor used was calibrated to be used for the measurement of the deflection for the test. The calibration curve was made using Microsoft Excel 2013, as shown below.

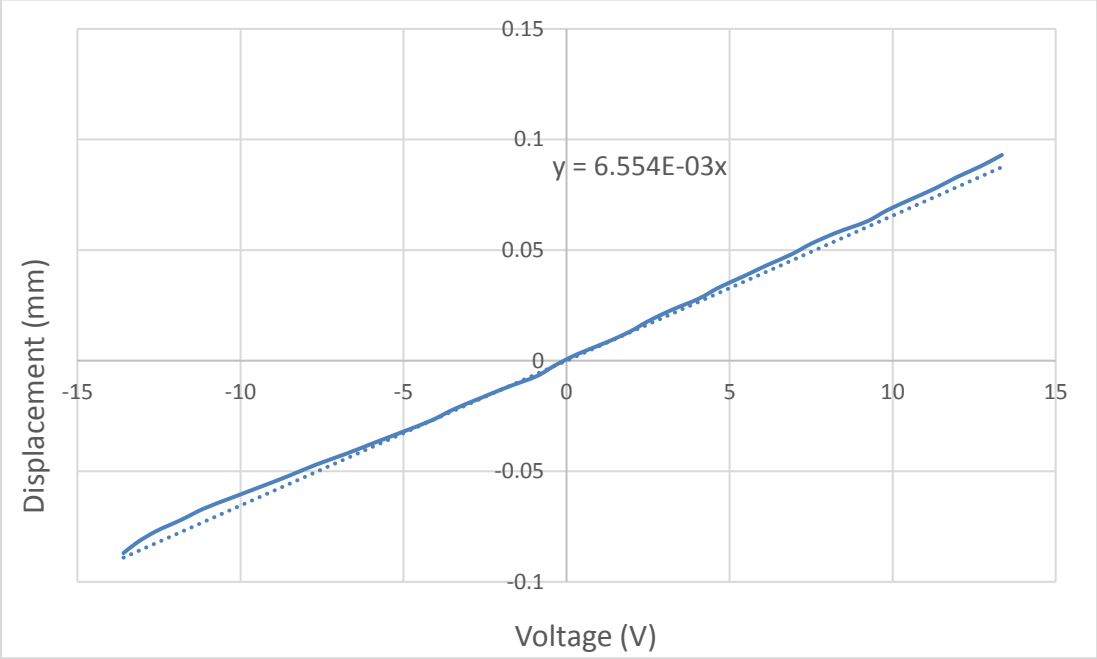

Figure 19: Voltage-Displacement curve for sensor

A linear trend was observed between the voltage and the distance from the sensor as expected. An equation was generated to generalize the sensor and to get exact deflection values using the voltage values measured. The equation is shown below.

$$d\ (mm) = 6.554\ x\ 10^{-3}\ V \qquad (14)$$

Using this equation, the deflection in the 4-point bending was calculated and then used to determine the modulus value of the samples.

These tests were performed on two combinations of different types of top and bottom parts for the experimental setup. These two sets of tests were performed for two samples of both EBM-y and EBM-z with 3 tests performed in each case. In every test different loads were applied at the center and measuring their corresponding deflections.

The tests gave the following results for the samples load-deflection plots for the two setups for both the EBM-y and EBM-z samples:

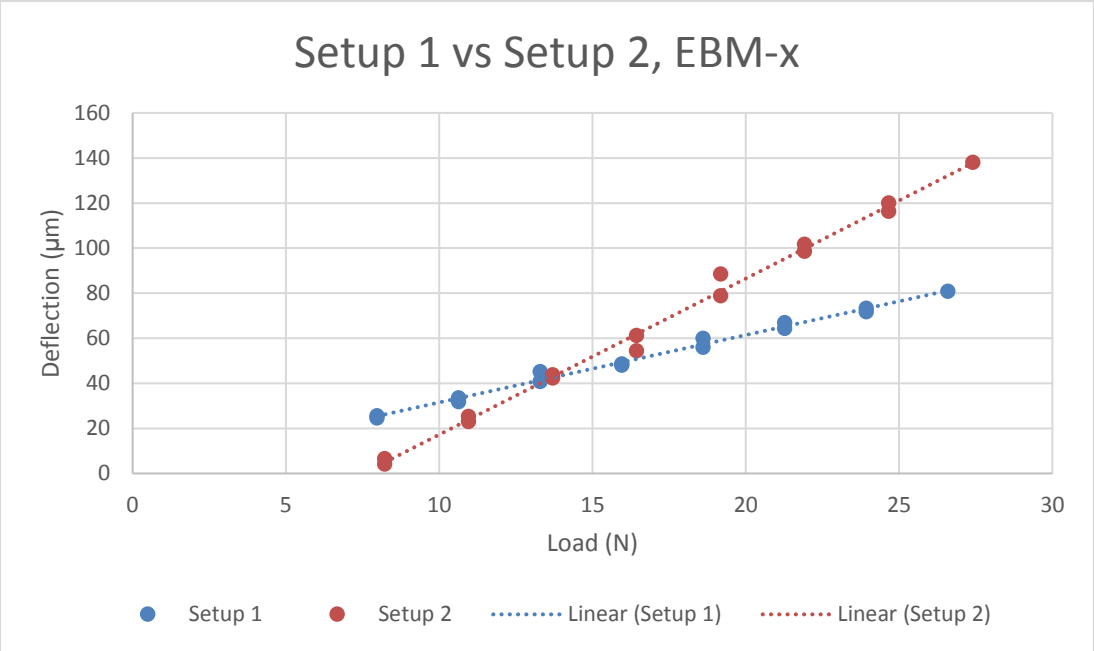

Figure 20: Load-deflection curve for EBM-x sample

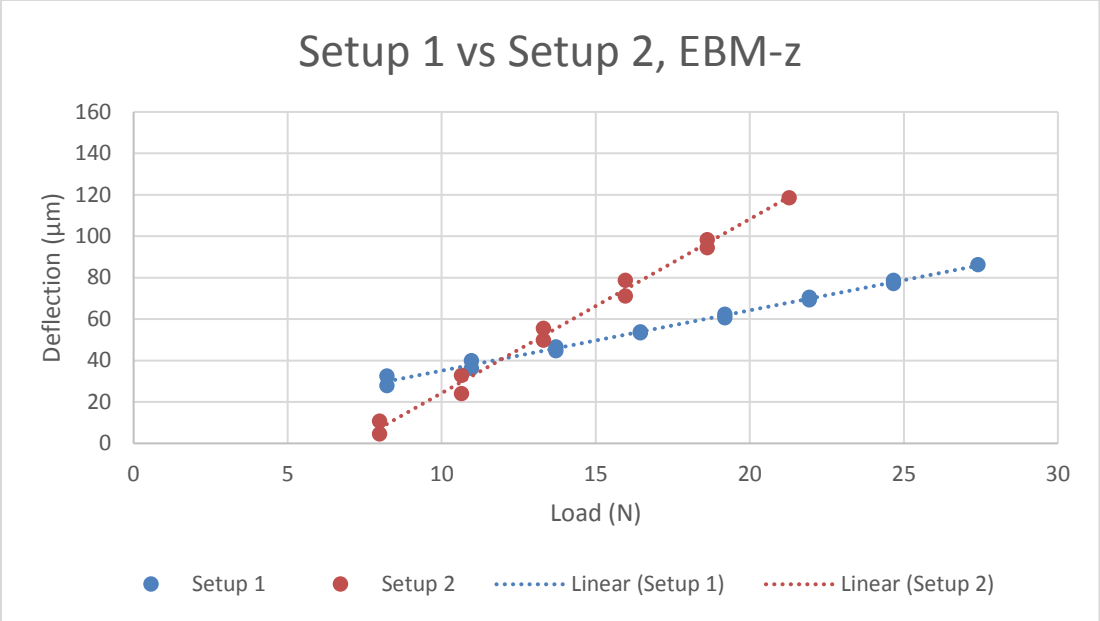

Figure 21: Load-deflection curve for EBM-z sample

For the 3 tests performed with every setup for each sample, the calculated values for the moduli of elasticity and their average and standard deviation are given in the tables below. The total length of all the samples was 50mm whereas the cross section dimensions, b and h are given in the table.

Table 8: Elastic Modulus for EBM-x and EBM-z samples (GPa)

	EBM-x		**EBM-z**	
b (mm)	3.18	2.92	3.2	3.02
h (mm)	2.11	1.95	2	1.77
a (mm)	5.5	8	5.5	8
L (mm)	35	40	35	40
Test 1	107.74	114.25	131.51	132.7
Test 2	118.66	116.94	134.56	130.043
Test 3	120.31	122.642	128.84	127.07
Average (GPa)	115.573	117.945	131.641	129.94
SD (GPa)	29.54	21.3	29.1	17.06

So the overall values for the EBM-x and EBM-z are given below

Table 9: Comparison between EBM-x and EBM-z samples modulus values

	EBM-x	**EBM-z**	**Percentage difference**
Elastic Modulus (GPa)	116.76	130.79	+12.09% (EBM-z)
SD (GPa)	36.41	33.73	

The results show that the elastic modulus value is higher for the EBM-z sample by 12.09%. That is consistent with the results from the nanoindentation tests.

2.3.3 3-point bending

After the 4-point bending tests there were 3-point bending tests conducted on an Instron 4206 universal testing machine. Three 3-point bending tests were performed for each of the sample EBM-x and EBM-z. The load-deflection curves for the three tests for both the samples are given below.

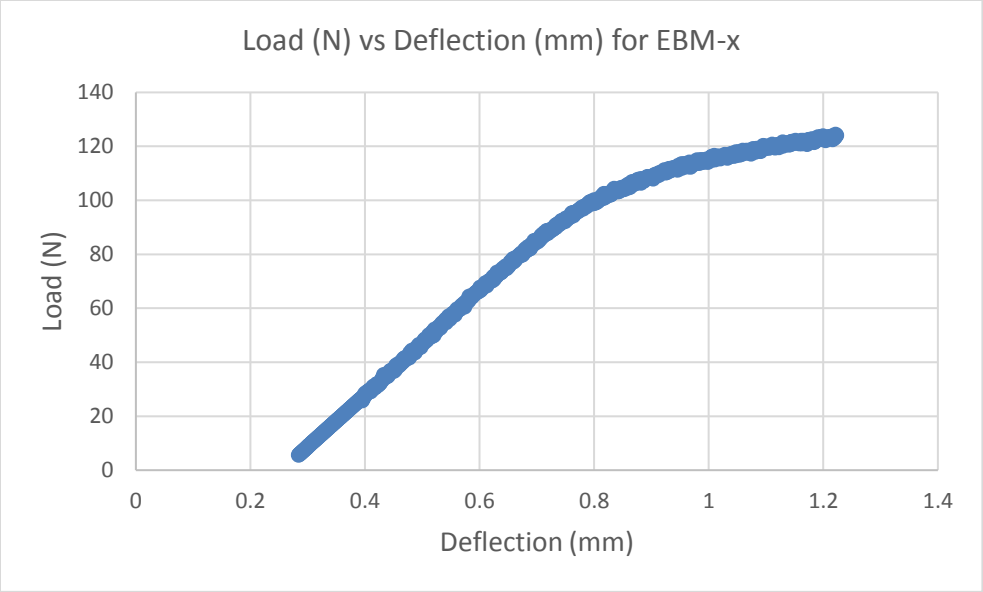

Figure 22: Load-deflection curve from 3-point bending for EBM-x

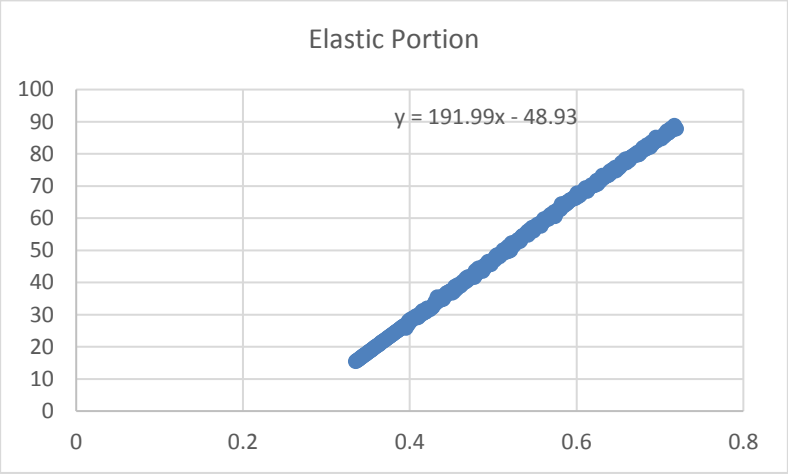

Figure 23: Linear elastic part of the3-point bending curve for EBM-x

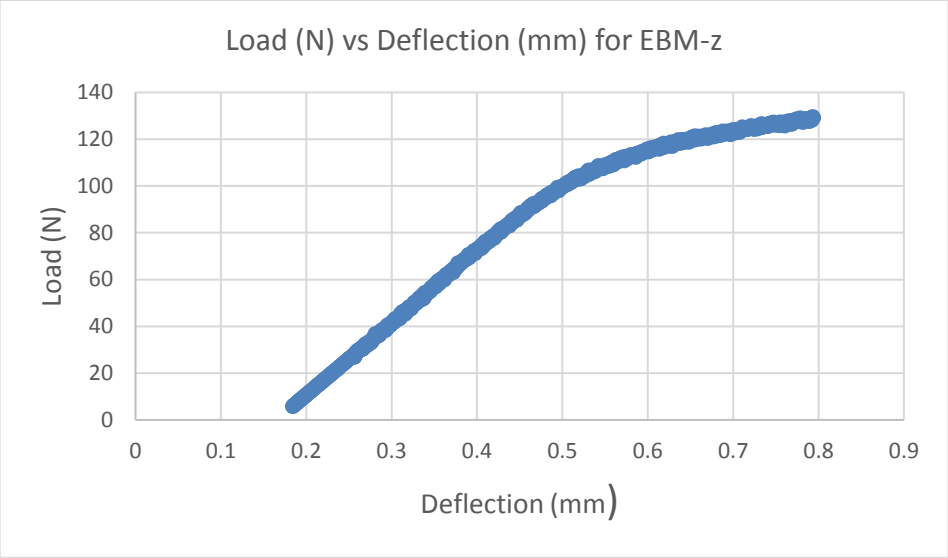

Figure 24: Load-deflection curve from 3-point bending for EBM-z

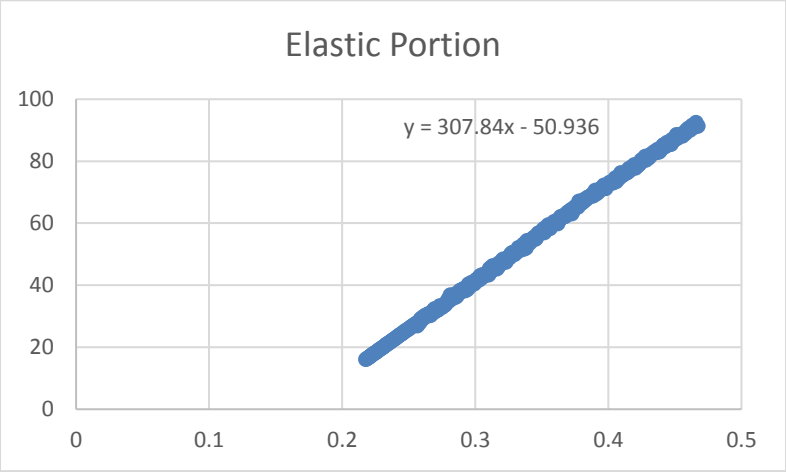

Figure 25: Linear elastic part of the3-point bending curve for EBM-z

Using the slope from the plots the following relation was used to determine the modulus of elasticity.

$$E = \frac{L^3}{48\,I} m \qquad (15)$$

Where L is the span length = 38.1 mm, I is the moment of inertia and m is the slope of load-deflection curve.

Table 10: Elastic Modulus for EBM-x and EBM-z samples (GPa)

	EBM-x	**EBM-z**	**Percentage difference**
Test 1	122.604	118.25	
Test 2	109.267	143.09	
Test 3	114.11	127.81	
Average (GPa)	115.327	129.71	+12.47% (EBM-z)
SD (GPa)	6.75	12.53	

2.3.4 Yield Strength Test

The yield strength of the samples was determined for two reasons. Firstly, to compare the anisotropic effect on the EBM-x and EBM-z samples and secondly to determine the load parameters for the wear tests to be conducted in chapter 4. The tests were done on the Nanovea M1 nanoindenter in the lab. A cylindrical flat tip indenter was used with tip diameter = 5 µm.

The indentation created on the samples is shown in the image below.

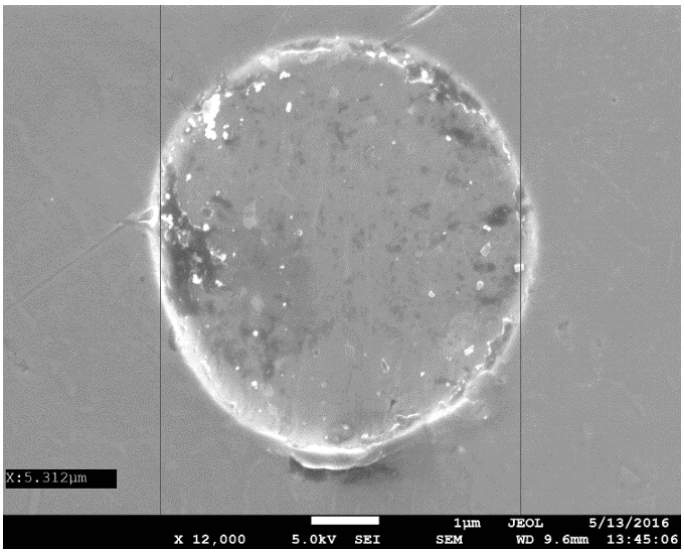

Figure 26: Flat tip indenter mark on EBM-x

There were 5 tests performed for each of the sample to determine the yield strength values. The point of inflexion was found on the loading part of the curve as the point with the maximum slope. This was done by creating a second plot between the slope and the load values. The load at that point was found and the yield strength was calculated using the force per unit area relation.

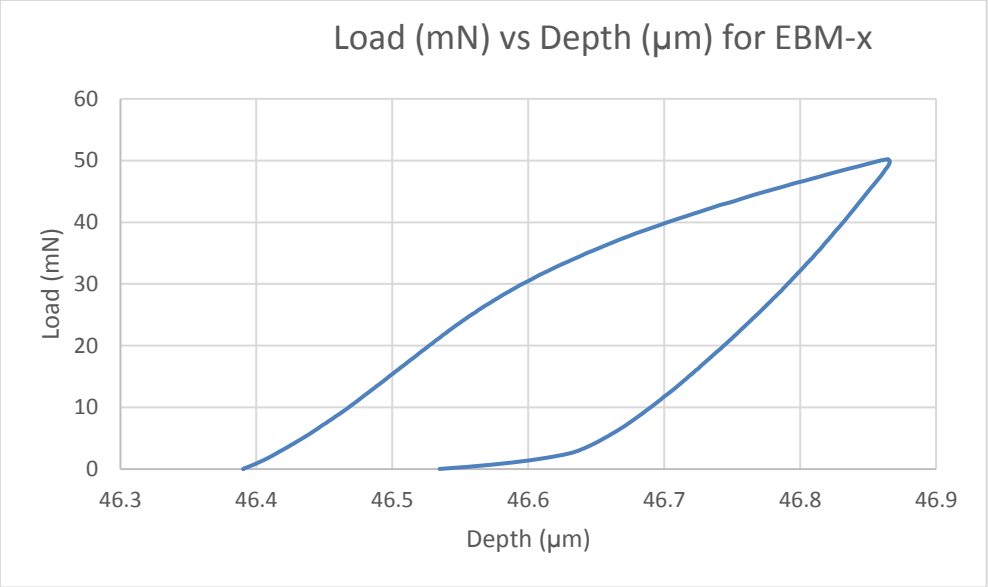

Figure 27: Load vs Depth for Yield Strength for EBM-x

The slope of the Load-Depth plot seems to increase in the beginning of the loading part of the test and then starts to decrease. The point where this slope is maximum is termed as the inflexion point. The material is believed to start to yield at the load at this point of inflexion so the load at this point was determined and the corresponding stress value was calculated. This test was repeated for 4 more times and a total of five values were taken for each sample.

To calculate the maximum slope, another plot was created showing the slope of the curve ($\Delta P/\Delta \delta$) vs the load. This is shown below.

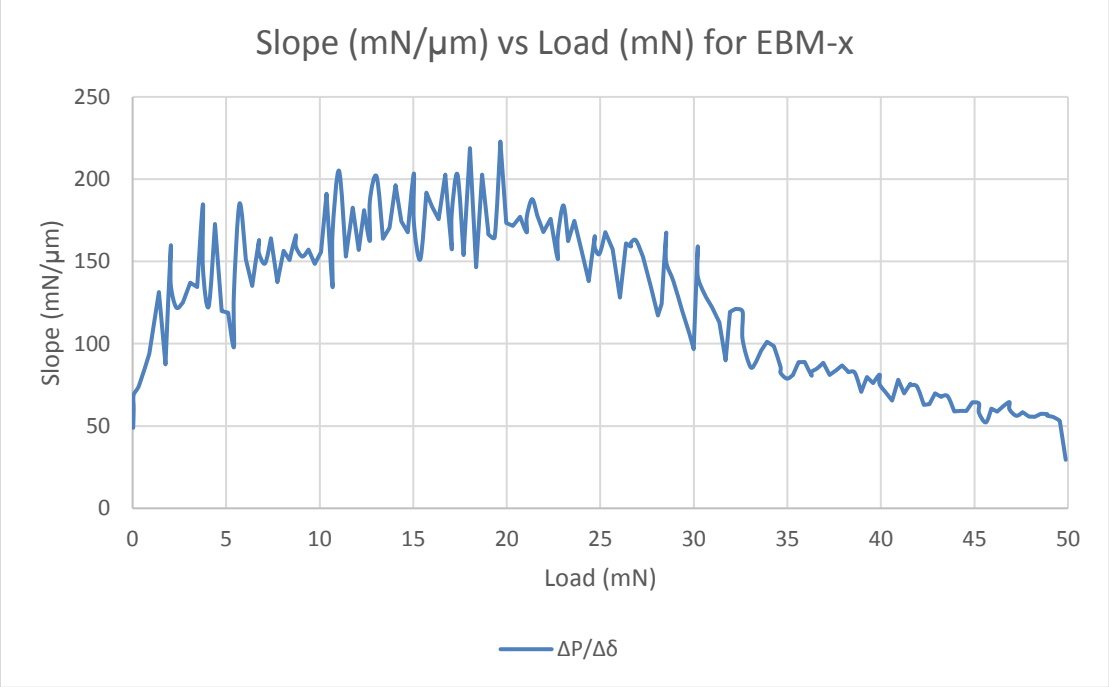

Figure 28: Slope vs Load for EBM-x

This test was then performed for the EBM-z sample to determine the yield strength for that. The plots for that are shown below.

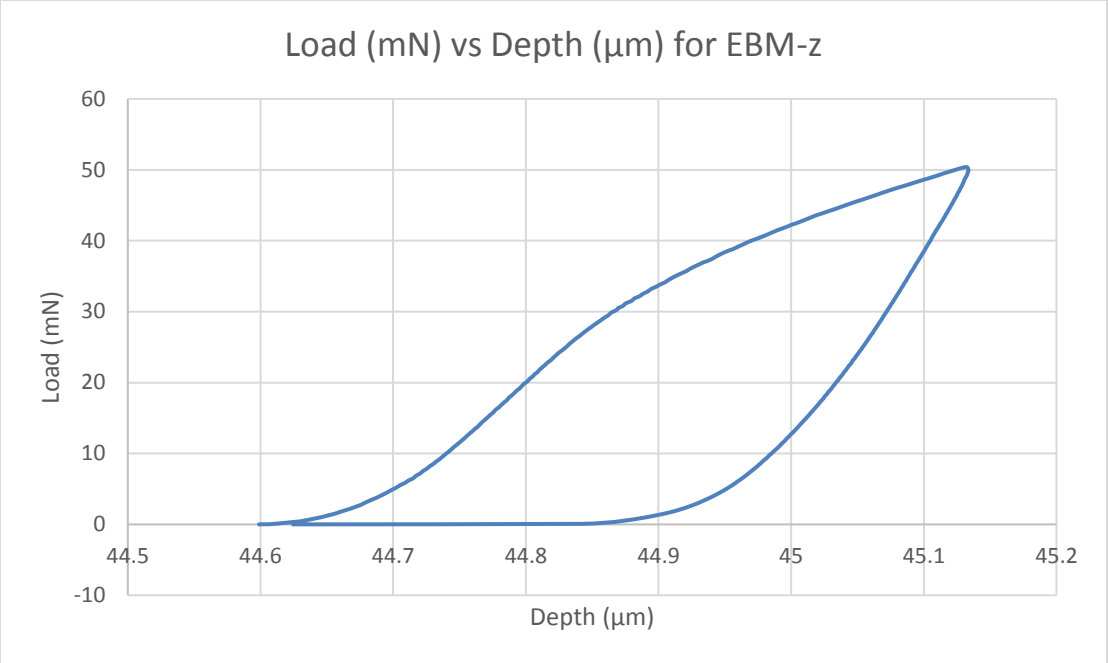

Figure 29: Load vs Depth for Yield Strength for EBM-z

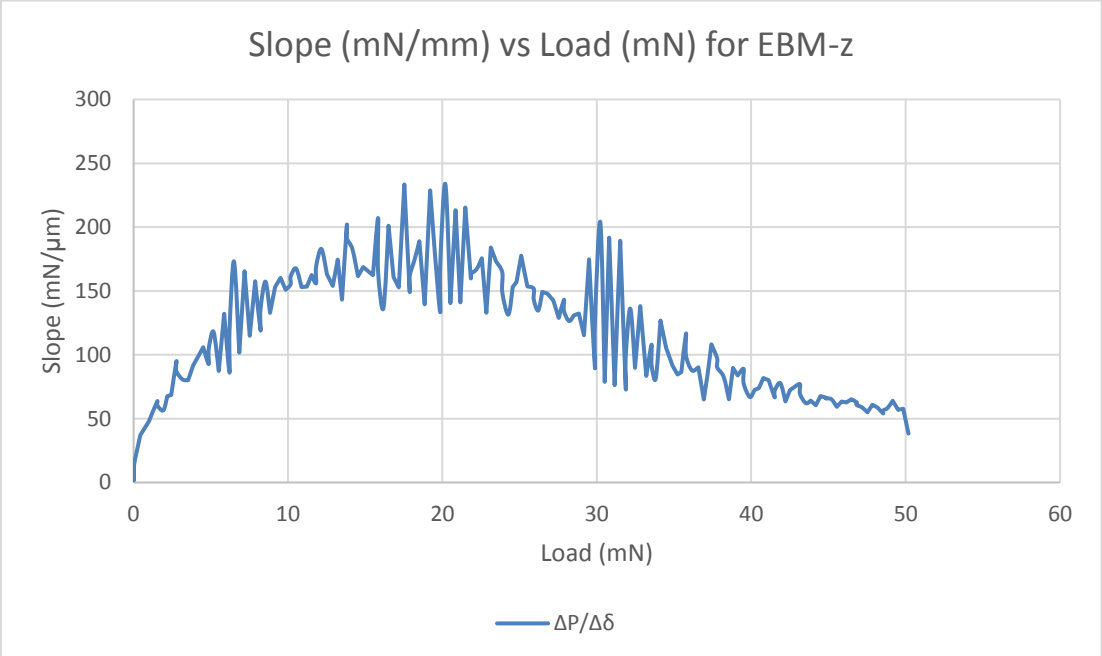

Figure 30: Slope vs Load for EBM-z

The load values at the yield point and their corresponding stress values are shown below in the table for all the 5 tests performed for each of the EBM-x and EBM-z samples.

Table 11: Yield strength values for EBM-x and EBM-z samples

	EBM-x		**EBm-z**		**Percentage difference**
	Yield Load (mN)	Yield Stress (MPa)	Yield Load (mN)	Yield Stress (MPa)	
Test 1	19.65	1000.76	20.19	1028.27	
Test 2	18.27	930.48	18.91	963.08	
Test 3	18.97	966.13	20.94	1066.46	
Test 4	19.05	970.21	21.56	1098.04	
Test 5	20.42	1039.98	20.72	1055.26	
Average		981.512		1042.22	+6.18% (EBM-z)
SD		41.102		50.82	

2.4 Conclusions

The purpose of this research was to determine and compare the mechanical properties of the Ti-6Al-4V samples manufactured by additive manufactured in two different orientations using different nano and micro-scale mechanical tests. The tests included nanoindentation, 4-point and 3-point bending setups.

The following chart shows the results from the mechanical tests performed on the samples EBM-x and EBM-z by all the three methods used.

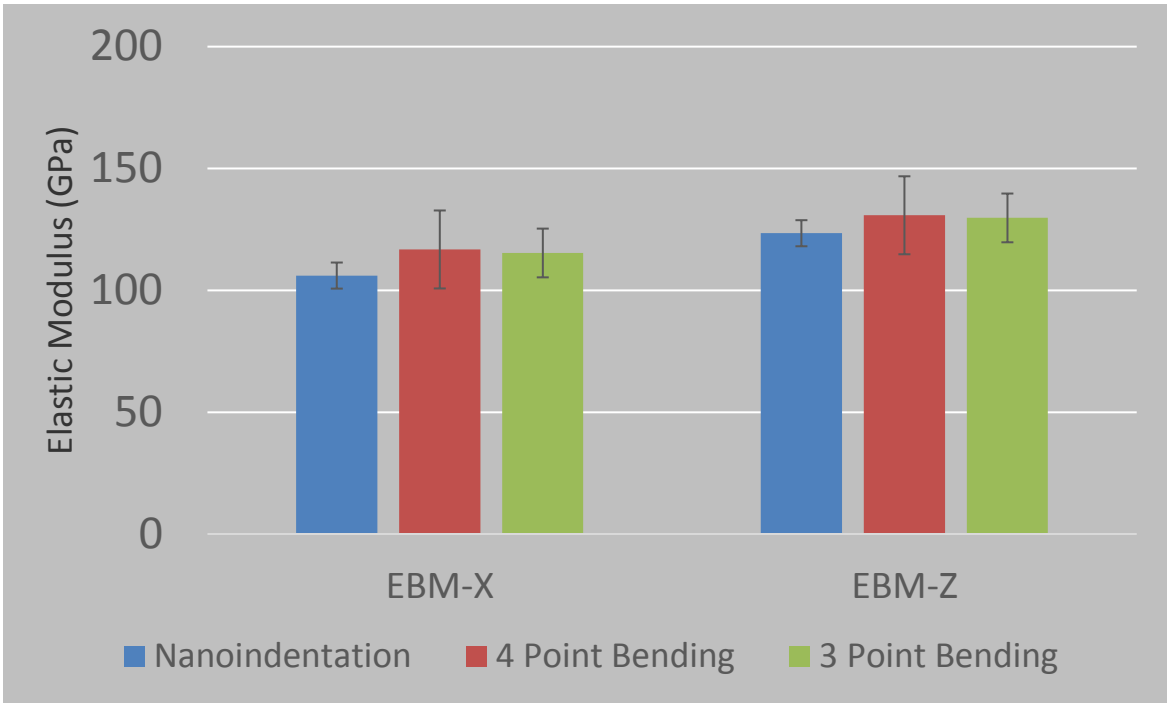

Figure 31: Bar chart with average results from mechanical tests

The chart above shows that the overall modulus values are higher for EBM-z samples relative to EBM-x. So the EBM-z Ti-6Al-4V can recommended for use in hip joint replacements being harder and stronger than EBM-x. Also it is seen that the 4-point bending tests have the highest standard deviation whereas the nanoindentation tests have the least. However, wear resistance also has to be analyzed to reach a final conclusion. That is done in chapter 4 of the research.

Chapter 3: Influence of Protein Concentration on Synovial fluids

Abstract

Unstable joint lubrication has been identified as a critical factor initiating the wear and corrosion that significantly limits the useful life of joint replacements. It occurs when the healthy synovial fluid is degraded by surgical wound healing and adverse physiological reaction of surrounding tissue against wear and corrosion products of implant materials. It is critical to know mechanical properties of the degraded unhealthy joint fluid to understand the joint implant lubrication. While a large number of studies have been undertaken to characterize the wear and corrosion behavior of artificial joints, the direct influence of biochemical conditions of synovial fluid on joint lubrication and implant surface damage mechanism are still not clearly understood. Titanium alloys are widely used for implant materials in the medical and dental fields because of their superior strength-to-weight ratio, greater ductility, and electrochemical stability compared to other metallic materials. Therefore, the objective is to identify the surface tension and viscosity evolution of unhealthy synovial fluid and implant surface fatigue wear responses.

In this chapter three synovial fluids were then prepared using different concentrations of bovine serum albumin (BSA) and chondroitin sulfate in phosphate buffered saline (PBS). A novel nanoindentation scheme in wet condition was employed to characterize properties of synovial fluids including surface tension and viscosity. The surface tension was observed to decrease and the viscosity to increase with the increase in BSA and chondroitin sulfate. In next chapter wear tests are performed using these three synovial fluids as

lubrication medium to see their influence on the wear to correlate their physical properties with their lubrication performance.

3.1 Introduction

3.1.1 Hip Joint

The hip is the body's second largest weight-bearing joint (after the knee). It is a ball and socket joint at the juncture of the leg and pelvis. The rounded head of the femur (thighbone) forms the ball, which fits into the acetabulum (a cup-shaped socket in the pelvis). Ligaments connect the ball to the socket and usually provide tremendous stability to the joint. The hip joint is normally very sturdy because of the fit between the femoral head and acetabulum as well as strong ligaments and muscles at the joint.

All of the various components of the hip mechanism assist in the mobility of the joint. Damage to any single component can negatively affect range of motion and ability to bear weight on the joint. Orthopedic degeneration or trauma – those conditions affecting the bones in the hip joint – can necessitate total hip replacement, partial hip replacement or hip resurfacing [23].

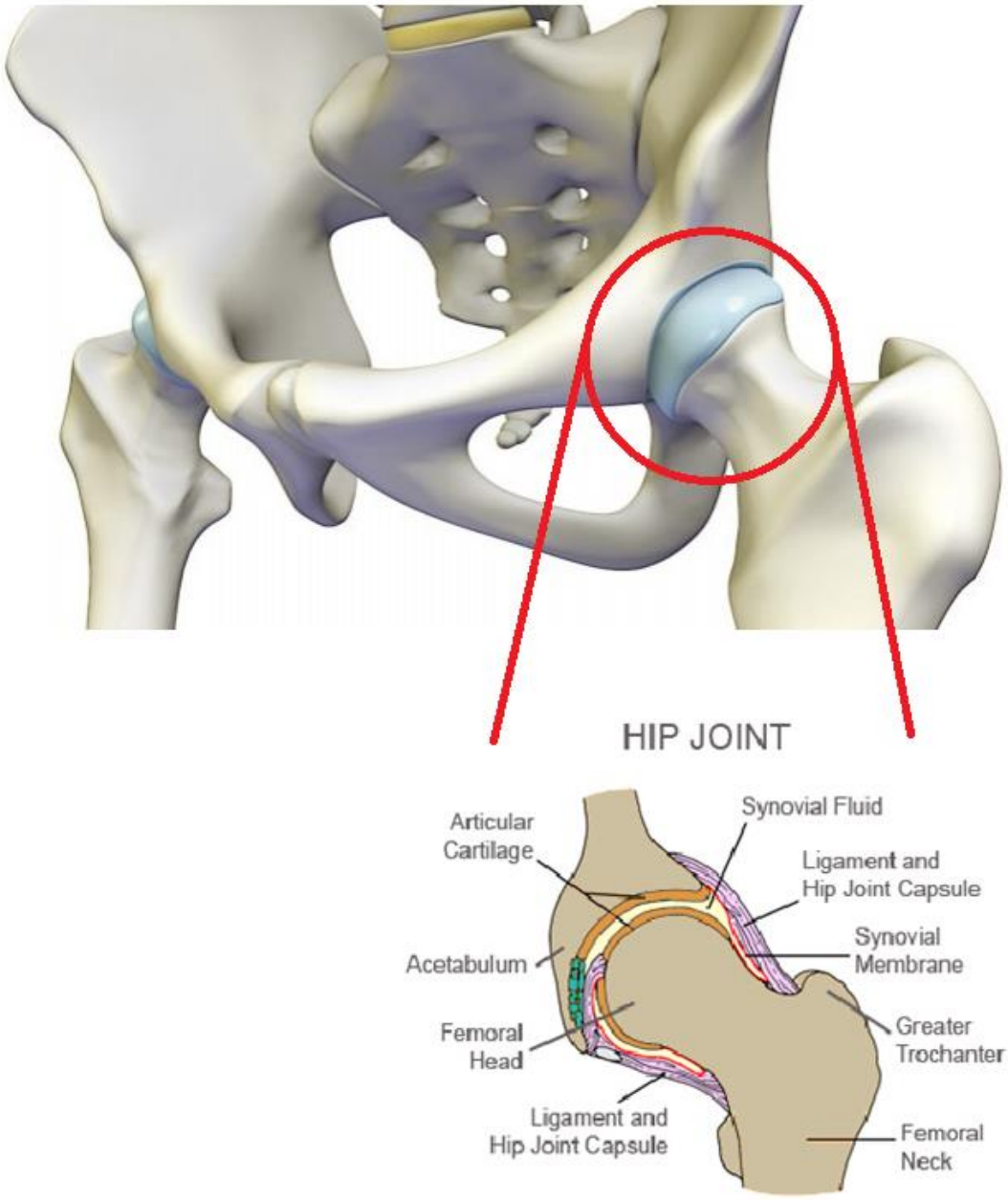

Figure 32: Normal hip joint [23]

3.1.1.1 Bones of hip joint

The femur is the upper leg bone or thigh. It is the largest bone in the body. At the top of the femur is a rounded protrusion which articulates with the pelvis. This portion is referred to as the head of the femur, or femoral head. There are two other protrusions near the top of the femur, known as the greater and lesser trochanters. The muscles involved in hip motion are attached to the joint at these trochanters. The acetabulum is a concave area in the pelvis, into which the femoral head fits. The bone surfaces of the femoral head and acetabulum have a smooth durable layer of articular cartilage that cushions the ends of the bones and allows for smooth movement [23].

3.1.1.2 Hip joint capsule

The joint capsule is a thick ligamentous structure surrounding the entire joint. Inside the capsule, the surfaces of the hip joint are covered by a thin tissue called the synovial membrane. This membrane nourishes and lubricates the joint [23]. The joint capsule is made up of an outer layer, the articular capsule, which keeps the bones together structurally, and an inner layer, the synovial membrane, which seals in the synovial fluid.

3.1.1.3 Synovial Fluid

Synovial fluid is a thick liquid that acts as a lubricant for the body's major joints. It is found in small quantities in the spaces between the joints, where the fluid is produced and contained by synovial membranes. Synovial fluid cushions bone ends and acts as shock absorber, reduces friction during joint movement in the knees, shoulders, hips, hands, and feet and also acts as a nutrient medium.

The synovial fluid fills the spaces between articular surfaces within the joints. Articular cartilage is also permeable to synovial fluid. This enables the two to work together to provide further joint protection

When articular cartilage is compressed, it pushes synovial fluid out and into the joint, where the fluid can lubricate the opposing surfaces. When compression is relieved, the fluid re-enters the articular cartilage. Similarly, synovial fluid acts as a shock absorber. Forces felt by the joints are spread across the synovial fluid, lessening stress on the articular surfaces [26].

Synovial fluid is an ultrafiltrate from plasma, and contains proteins derived from the blood plasma and proteins that are produced by cells within the joint tissues [27]. The fluid contains hyaluronan secreted by fibroblast-like cells in the synovial membrane, lubricin (proteoglycan 4; PRG4) secreted by the surface chondrocytes of the articular cartilage and interstitial fluid filtered from the blood plasma [28]. This fluid forms a thin layer (roughly 50 μm) at the surface of cartilage and also seeps into microcavities and irregularities in the articular cartilage surface, filling all empty space [29]. The fluid in articular cartilage effectively serves as a synovial fluid reserve. During movement, the synovial fluid held in the cartilage is squeezed out mechanically to maintain a layer of fluid on the cartilage surface.

3.2 Materials and Method

3.2.1 Synovial fluid characterization

Healthy synovial joints act as a lubricant providing very smooth motion between limb segments and greatly reduce wear. It is due to the articular cartilage and synovial fluid minimizing the sliding friction at the synovial interface. The viscous-elastic cartilage tissue that covers bone ends bears severe impact loadings and shear forces during high jerks or fast motion. However, total joint replacement removes the natural articular cartilage and replaces it with a synthetic joint material. It is inevitable to lose a smooth mobility and wear protection of the artificial joints. Its useful life is seriously restricted due to continuous surface fatigue and corrosion at the joint interface

Wear and fretting corrosion in the artificial joint result in the formation of soluble and particulate debris that can migrate in locally or systemically and may induce a cascade of inflammatory events that may ultimately result in bone loss by osteolysis and subsequent implant failure. The adverse tissue reaction lowers pH level and increase protein concentration in the synovial fluid, and therefore the unhealthy joint fluid further influences the tribo-corrosion of the joint. Wear tests were to be performed to replicate these conditions and determine their effect on the tribological response of the samples. The tests were to be done in both dry and wet conditions. For that three solutions were made, replicating the different concentrations of synovial fluid in human joints. The three solutions had the following compositions:

i. PBS (NaCl 9g/L + KH_2PO_4 0.144 g/L + Na_2HPO_4-$7H_2O$ 0.795 g/L)

ii. PBS + 19g/l Bovine Serum Albumin + 3g/l Chondroitin Sulfate Sodium (C1)

iii. PBS + 48g/l Bovine Serum Albumin + 3g/l Chondroitin Sulfate Sodium (C2)

The second fluid (C1) was the closest to the actual bodily synovial fluid [39]. The third fluid (C2) was made to replicate the infected fluid after the surgery or due to the wear debris spread throughout the joint after replacement [41].

So it was very important to understand how the metallic implant surface damage is affected by the change in composition of the synovial fluid. A series of experiments were conducted to understand mechanisms of fluid wettability and viscosity with variable biochemical constituents of synovial fluid to elucidate the ultimate synovial lubrication effect on knee joint implant surface damage. So the following experiments were setup to determine the physical properties including surface tension and viscosity of these concentrations and then see the wear of the samples in their corresponding wet tests.

3.2.2 Surface Tension Effect

The surface tension of a fluid affects its wettability and hence the wear of the material it's used for lubricating. To compare the surface tension values of the 3 fluid concentrations mentioned earlier a test was performed using the Nanovea nanoindenter M1. A series of cyclic indentations was performed with a slow indentation motion on soft polymer surface covered by the fluid. A conical tip indenter was selected to perform the test.

As the indenter broke the fluid surface it started to experience a negative (downward pulling) force due to the surface tension. The negative force (downward force) with tip displacement under the liquid surface during the slow motion was used to estimate the surface tension of fluids with different concentrations and pH levels. During the indentation motion, it was observed that as the indenter broke into the surface of the fluid, it experienced a downward force due to the surface tension of the liquid. That force was observed to linearly increase as the indenter went deeper into the liquid but before getting in contact with the sample. The slope of the force-displacement curve was used to determine the surface tension of the fluid [42]. It is shown in the following image:

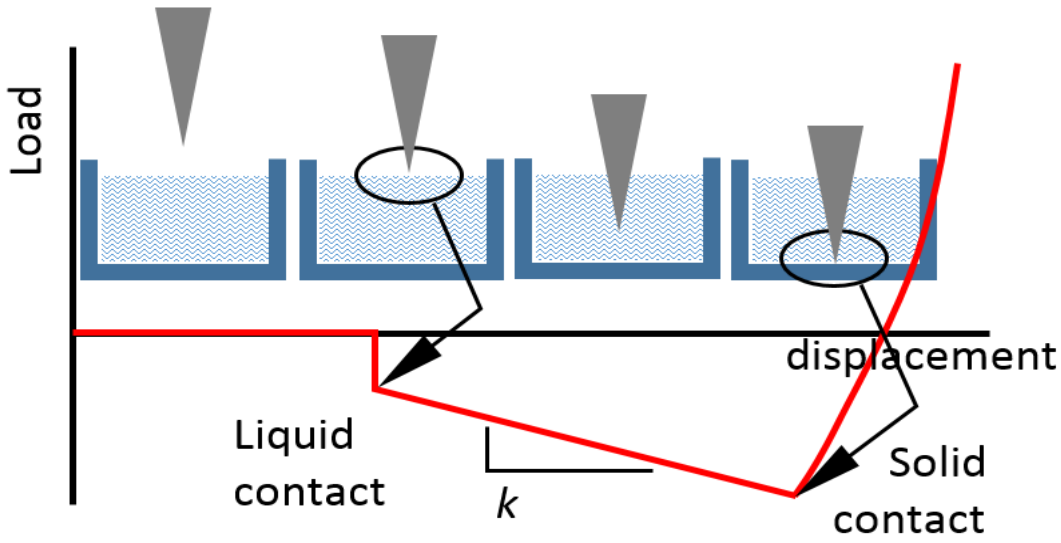

Figure 33: Surface tension measuring test setup

The surface tension was estimated using the following relations for the conical indenter.

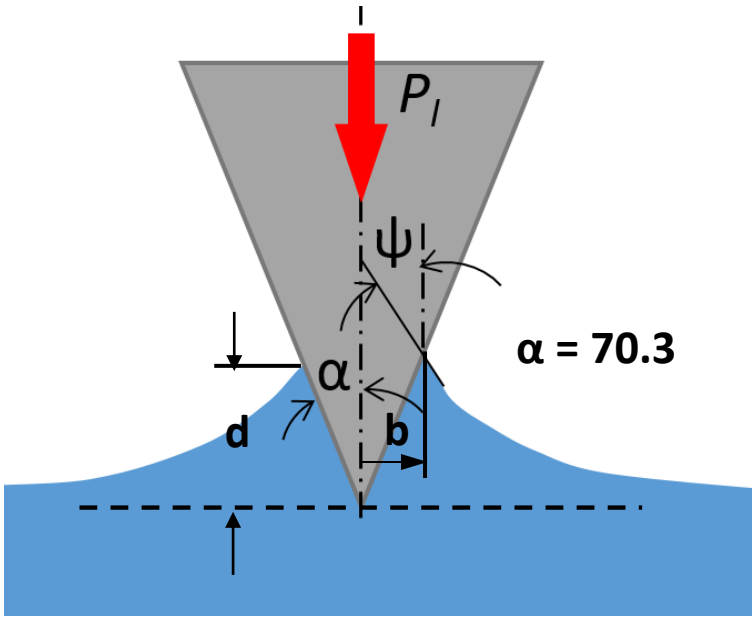

Figure 34: Schematic of conical indenter in surface tension test

By definition of surface tension [42]:

$$P_l = -\mathrm{K}\,\mathrm{d} \tag{16}$$

Also for a conical indenter:

$$P_l = -2\,\pi\,\mathrm{b}\,\gamma\cos\psi \tag{17}$$

Or

$$P_l = -2\,\pi\,(\mathrm{d}\tan\alpha)\,\gamma\cos\psi \tag{18}$$

So:

$$K = (-2\,\pi\tan\alpha)\,(\cos\psi)\,\gamma \tag{19}$$

Finally

$$K \propto (\cos\psi)\,\gamma \tag{20}$$

Where

P_l is the force experienced by the indenter

K is the slope of force-depth curve

d is the depth

γ is the surface tension of the fluid.

b is the contact length between indenter and fluid surface

ψ is the meniscus angle of the synovial fluid

α is the angle of the conical indenter

So this test was repeated for all the fluids to determine their corresponding values for surface tension to be used to relate with their corresponding wear in the wear tests.

3.2.3 Viscosity Effect

The viscosity of a fluid determines the shear stress and hence the shear force when sliding on a surface. Hence the viscosity is a very important factor in determining the tribological effect of a fluid. To determine the viscosity of the 3 fluid concentrations mentioned, the Nanovea M1 nanoindeter was used. Unlike the test for surface tension, for viscosity a flat cylindrical indenter was used. The indenter was moved inside the fluid at variable velocity. Viscosity is a time-dependent mechanical property, therefore, it was necessary to apply variable motion speeds to observe the viscosity effects at different rates. The flat indenter was immersed into the fluid at different velocities and a slight positive (upward) force was observed compared to that of surface tension. Different sets of load and depth values were

exported from the software for the tests of immersing the flat indenter into different liquids. Plots were made for every case to see the trend and behavior. The viscosity was mathematically approximated from the ratio between the slope of the force-depth curve and the indenter velocity.

To determine the surface tension effect, the test was firstly performed at a very low speed, eliminating the viscosity effect. Then to eliminate it, the measured liquid draft force observed at the slowest speed, was subtracted from the force data obtained in this viscosity measurement at higher velocities. Experimental results presented correlations between indentation rate and liquid friction. Also the load-depth curves obtained for the case of each speed were almost straight lines. The linear approximation was used to determine the viscosity parameter since the contact area increased linearly as the indenter went deeper into the fluid [43].

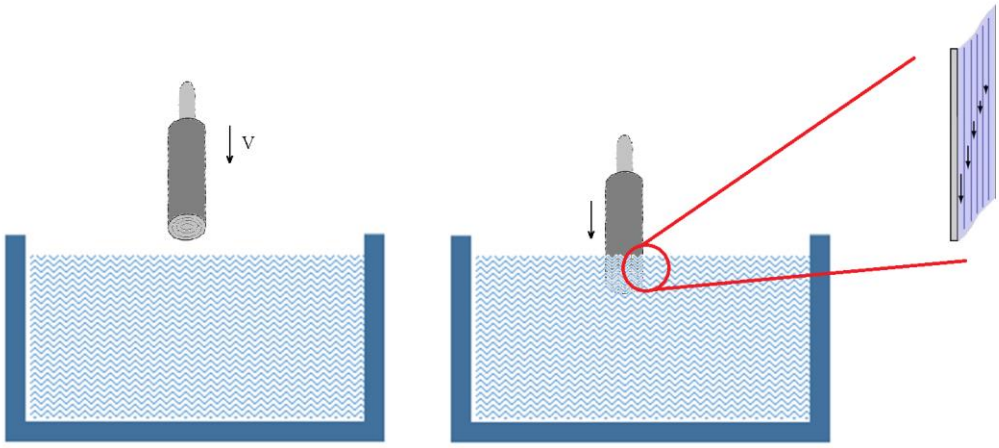

Figure 35: Viscosity measuring test setup

The following relations were used to approximate and compare the viscosities of the different fluid compositions:

$$\text{Shear Stress} = \tau = \mu \frac{du}{dy} \tag{21}$$

$$\tau = \mu \frac{\mathrm{d}}{\mathrm{dy}}\left(\frac{\mathrm{dz}}{\mathrm{dt}}\right) \tag{22}$$

$$\tau = \mu \frac{\mathrm{d}}{\mathrm{dt}}\left(\frac{\mathrm{dz}}{\mathrm{dy}}\right) = \mu \frac{\mathrm{d}}{\mathrm{dt}}\gamma_{\mathrm{z}} = \mu \dot{\gamma}_{\mathrm{z}} \tag{23}$$

$$\tau = \frac{\mathrm{P}}{\mathrm{A}} = \frac{\mathrm{P}}{2\pi \mathrm{r} z} \tag{24}$$

$$\dot{\gamma}_{\mathrm{z}} \propto \mathrm{v}_{\infty} \tag{25}$$

$$\frac{\mathrm{P}}{2\pi \mathrm{r} z} \propto \mu \mathrm{v}_{\infty} \tag{26}$$

$$\mu \propto \frac{1}{\mathrm{v}_{\infty}} \frac{\mathrm{P}}{z} \tag{27}$$

Where,

P is the upward force observed by the indenter

u is the downward motion speed of the indenter

z is the depth

A is the contact area

r is the indenter radius

$\dot{\gamma}_z$ is the shear rate

So using the final relation the viscosities of the different concentration synovial fluids were compared based on the ration of the slope of the load-depth curve and the velocity. Different values were calculated at different motion speeds of the indenter. In the end the mean was taken to approximate the viscosity of every fluid.

3.3 Results and Discussion

There were three different fluids prepared to replicate different concentrations of the bodily synovial fluid. Each of them was used as lubrication medium to see their effect on the mechanical wear of the bone implant material, Ti-6Al-4V. To see the trend of the concentration of the fluids with their lubrication tests were conducted to analyze the surface tension and viscosity of the fluids.

The tests gave the following results:

3.3.1 Surface Tension

The test performed for quantifying the surface tension of the three fluids and to see the effect of different protein concentrations on the surface tension was described in the earlier section. The following figure shows the plot of the force and the depth for the three fluids.

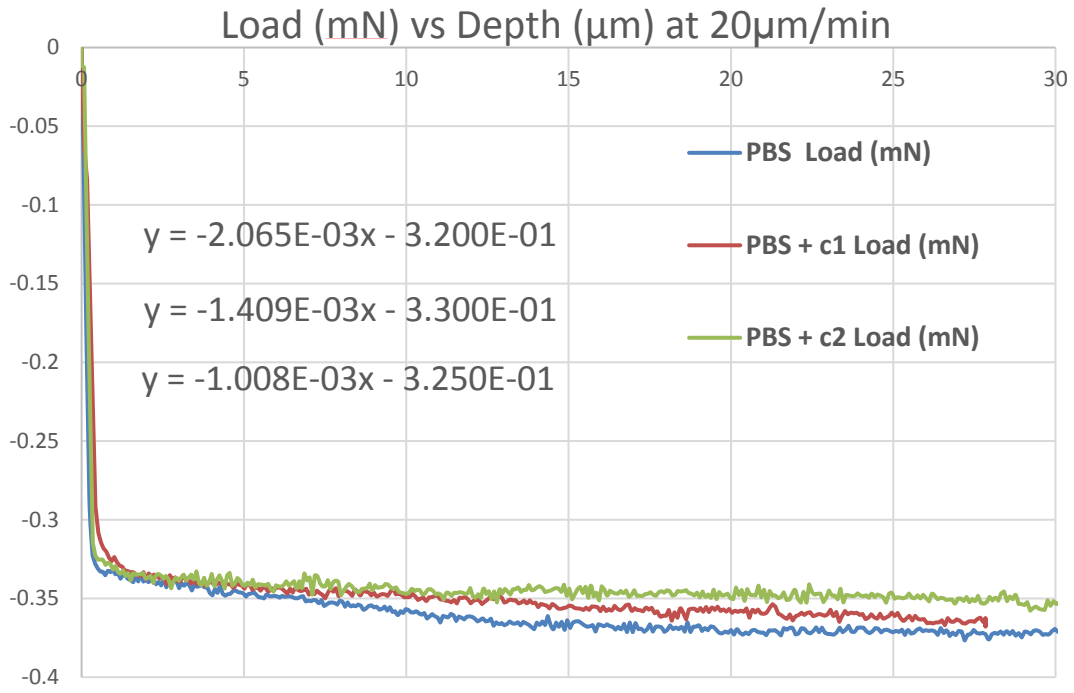

Figure 36: Load variation with depth for the 3 fluids

The plot shows that as the tip of the conical indenter broke into the liquid surface, it experienced a sudden pulling force. This force was due to the surface tension of the fluid. As the indenter was made to move deeper into the liquid, the force was observed to linearly increase. This increase was due to the increase in the contact length between the liquid and the indenter. This slope was used to quantify the surface tension of all the three fluids.

The first fluid i.e. PBS is observed to have the highest slope of all the three fluids. That shows that it has the highest surface tension of all the three. The second fluid (PBS + C1) has the intermediate slope and the third fluid (PBS + C2) has the least slope. In these three fluids the amount of protein is the major difference, with the largest in the third fluid. This shows that as the amount of protein increases in the synovial fluid the surface tension decreases.

These tests for the surface tension were performed a total of five times. For the estimate of the surface tension the slopes of the linear part of the plot, seen after the indenter breaks into the liquid was calculated. The average values of the constant K, takes as the ratio of the surface tension force, F and the depth of the indenter are mentioned below in the chart with the corresponding standard deviations.

Table 12: Surface tension values for three synovial fluids

	PBS	PBS + C1	PBS + C2
	K1 (mN/µm)	K2 (mN/µm)	K3 (mN/µm)
Average (x 10^{-3})	2.065	1.409	1.008
Standard Deviation (x 10^{-3})	0.15	0.11	0.13

3.3.2 Viscosity

Tests were performed on the Nanovea M1 Nanoindenter to compare the viscosity of the synovial fluids. These tests were similar to those performed for the surface tension. But for viscosity measurement a flat cylindrical indenter was used. The process is explained in the previous section.

The indenter was immersed into the liquids at different speeds to see the effect of the viscosity of the fluids. The indenter experienced an upward (positive) force compared to the surface tension at higher speeds. That was due to the shear stress of the fluid on the indenter. Firstly, the test was performed with PBS at a very slow speed to minimize the

effect of viscosity and to only observe the effect of surface tension. Then it was repeated at higher speeds. The first test was performed at 20 µm/min then at 100 µm/min, 200 µm/min, 400 µm/min, 600 µm/min, 800 µm/min and finally at 1000 µm/min. These tests were then repeated for the other two fluids.

To observe only the effect of viscosity, the curve for the surface tension, obtained at the lowest speed was subtracted from the following curves obtained at higher speeds, this is shown in the following figures. For these curves a linear trend was seen between the upward force and the depth of the indenter. The slope of this line was seen to increase with increasing speeds. The ratio of the slope of the load-depth curve and the speed was then calculated to estimate the viscosity of the fluids [43].

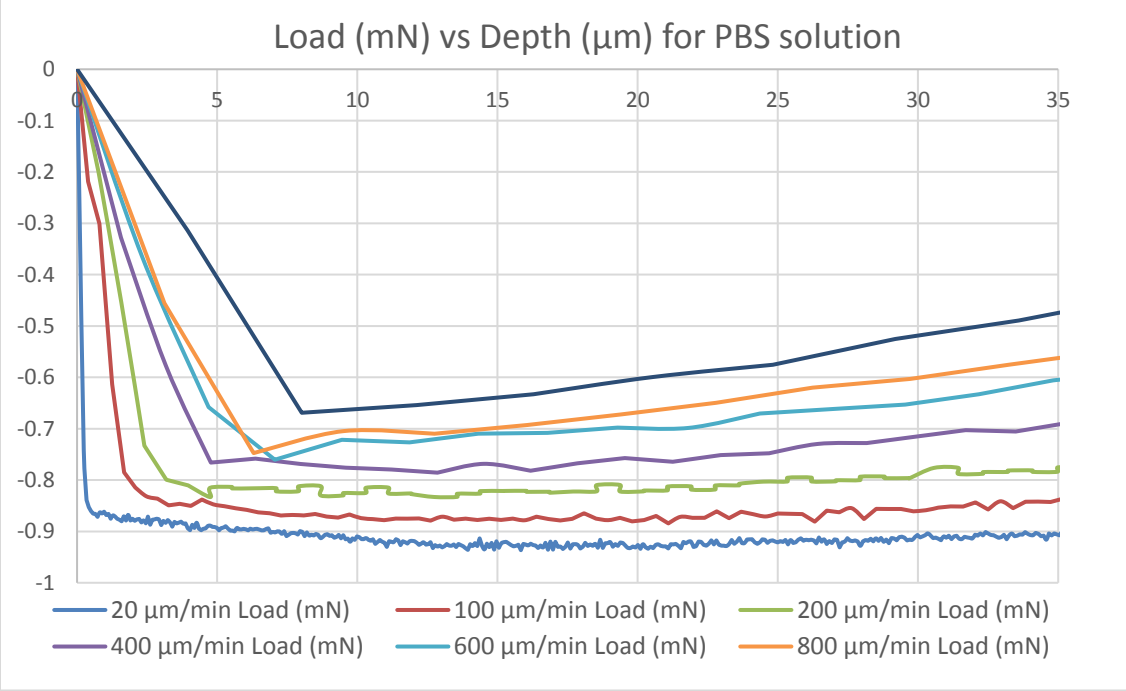

Figure 37: Load variation with depth for the PBS at different speeds

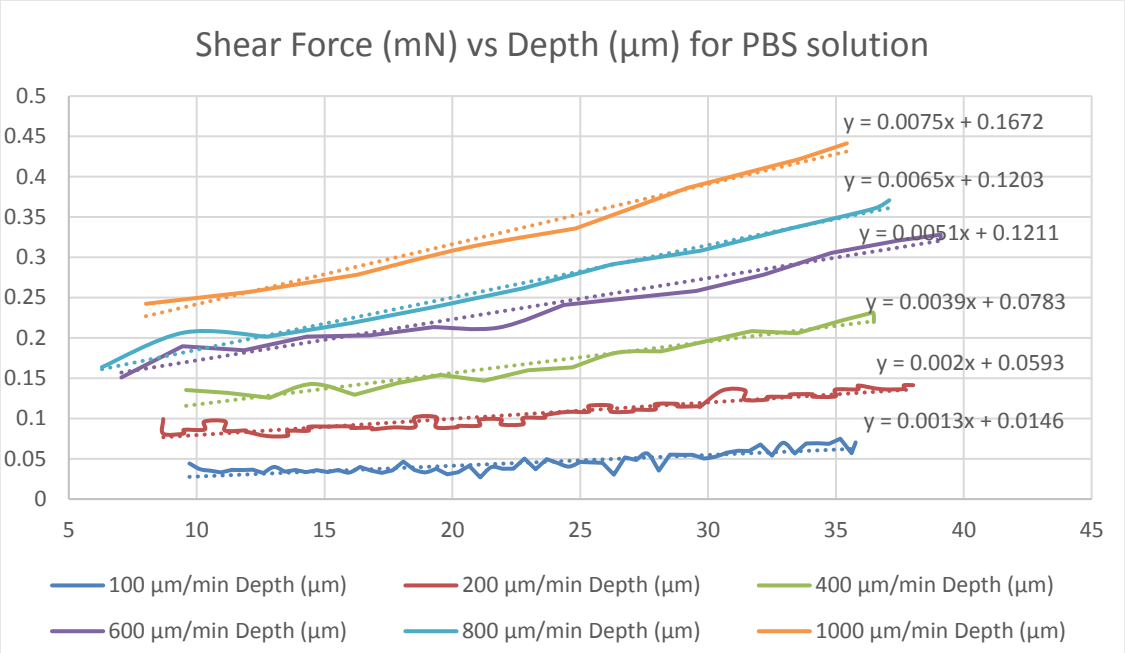

Figure 38: Viscosity effect of PBS at different speeds

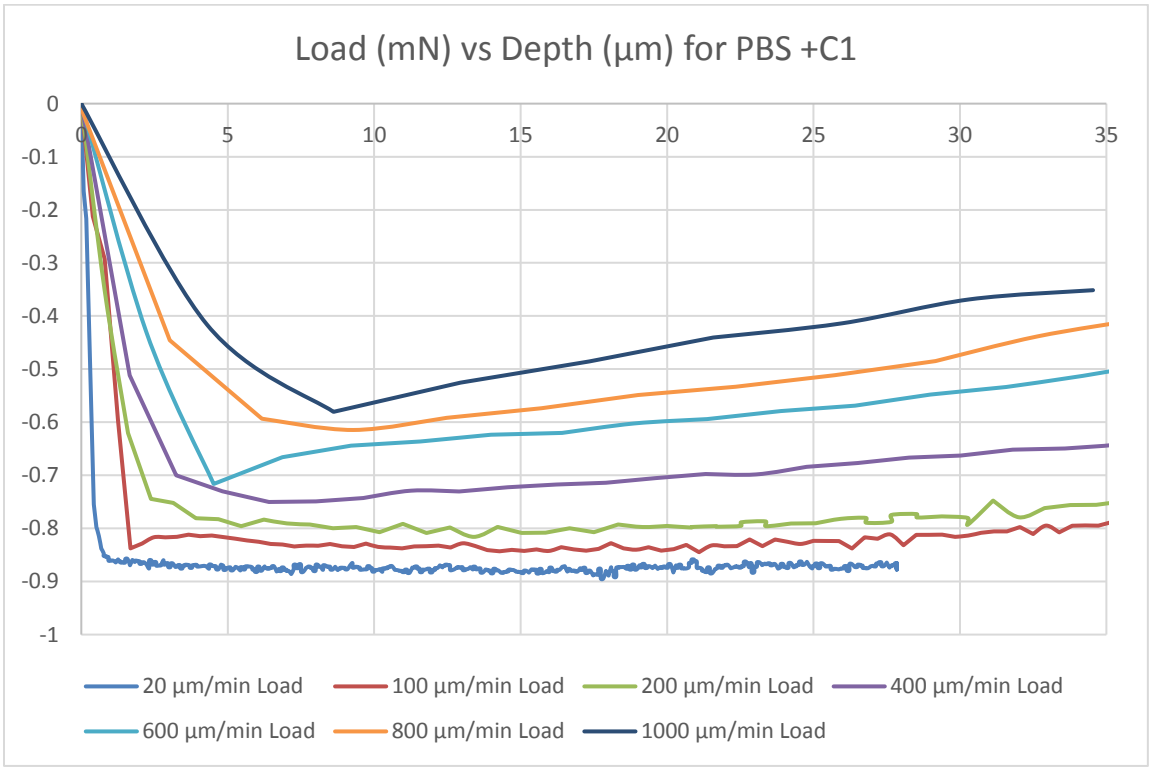

Figure 39: Load variation with depth for PBS + C1 at different speeds

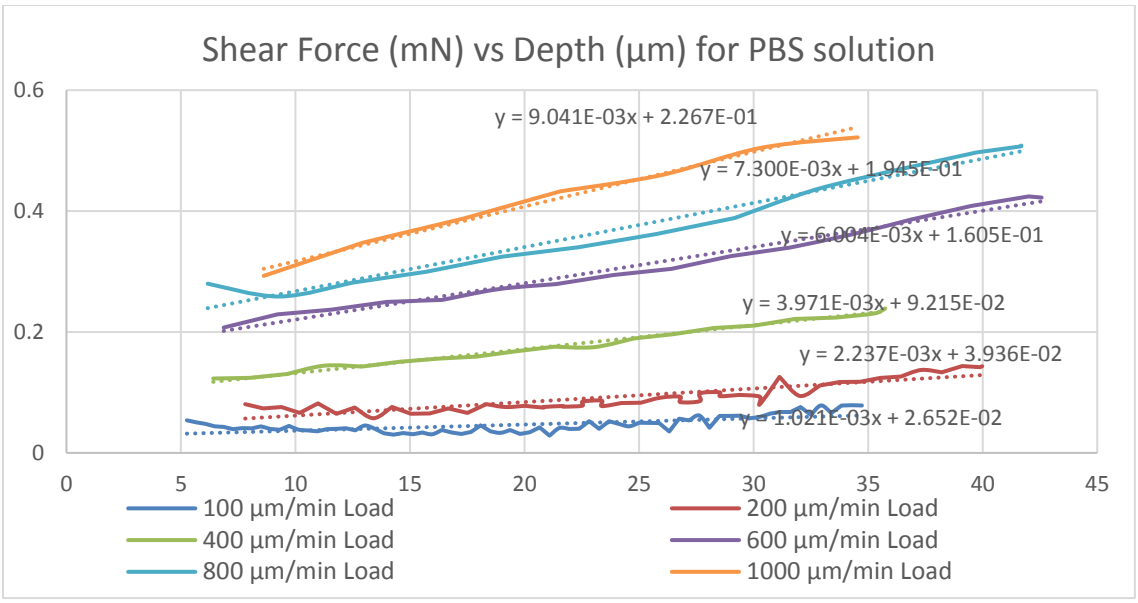

Figure 40: Viscosity effect of PBS + C1 at different speeds

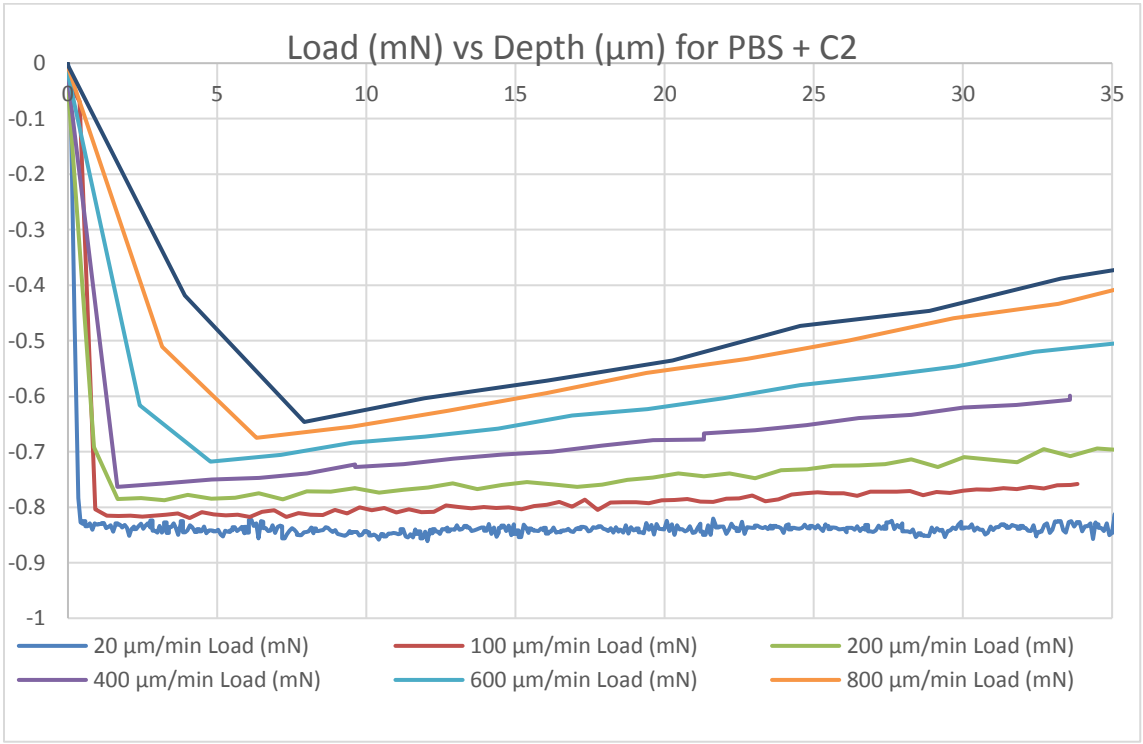

Figure 41: Load variation with depth for PBS + C2 at different speeds

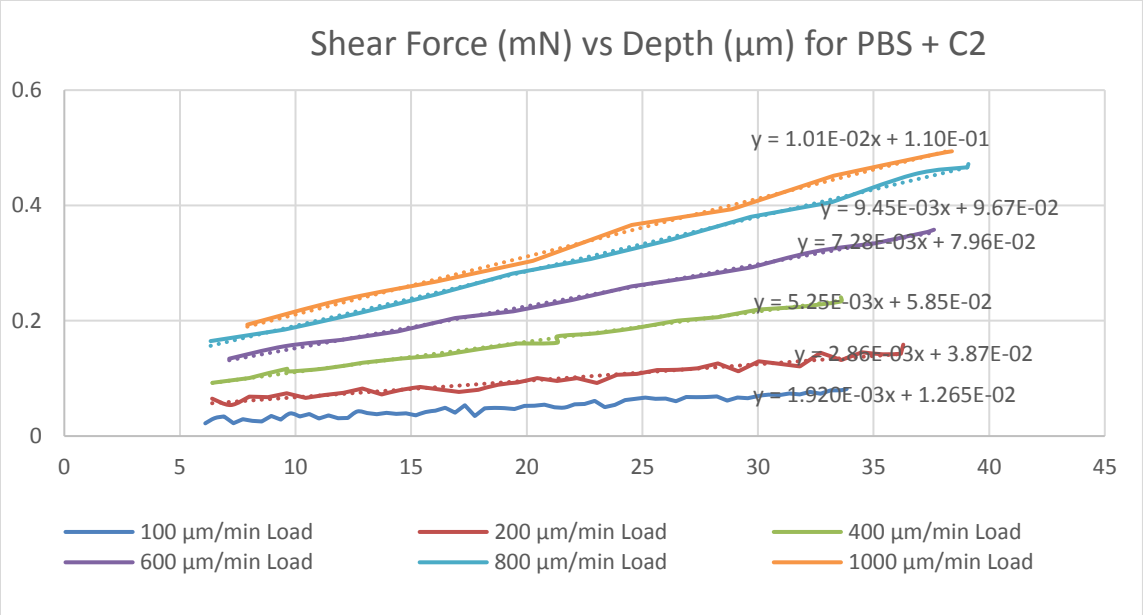

Figure 42: Viscosity effect of PBS + C2 at different speeds

The following table shows the average viscosity values estimated for the three fluids. The viscosity values were estimated by taking the ratio of the shear force-death linear plot and the speed. It gave a total of 6 values for each fluid. The table shows the average of those values and their standard deviation.

Table 13: Surface tension values for three synovial fluids

	PBS	PBS + C1	PBS + C2
	μ_1 (mN-min/µm^2)	μ_2 (mN-min/µm^2)	μ_3 (mN-min/µm^2)
Average (x 10^{-5})	0.95	1.05	1.35
Standard Deviation (x 10^{-3})	0.0012	0.0047	0.0054

3.4 Conclusions

From the results it is seen that adding protein into the synovial fluid reduces the surface tension and increases the viscosity. Surface tension is mostly due the hydrogen bonding between the water molecules, which is the attraction between the positively charged hydrogen atom and the negatively charged oxygen atom due to difference in their electronegativity. So it seems that adding protein weakens the hydrogen bonding between the water molecules, reducing the surface tension [48]. However, the increase in viscosity shows that the intermolecular attractions between the added constituents becomes stronger. This increase in the forces makes the fluid thicker and increasing resistance to flow, which makes sense. That could be due to stronger forces arising between the salts, protein and chondroitin sulfate in the fluids. Molecular size could be another important feature, since the protein molecules retain their larger sizes after being mixed in the PBS solution, so they appear to be increasing the viscosity and hindering the flow properties of the solution. That could be because proteins contain long chains of amino acids [50].

Chapter 4: Tribo-corrosion damage of AM made joint implants

Abstract

Metal on metal hip implants have become a very popular option for total hip joint replacement, the most common metal being Titanium and its alloys. The major reasons for that being stronger material and lesser wear. But even though after reduced wear, the small wear debris produced by the metal implants migrate locally and have a higher tendency of inducing inflammatory events in the body. Also the metal ions released is an electrochemical process which leads to corrosion. This also affects the synovial fluid lowering its pH and increasing the protein concentration, which influences its corrosion resistance, lubrication and immunological reactions. So in this chapter the effect of the change in the synovial fluid concentration is correlated to the tribological response of the Ti-6Al-4V samples. To generalize this impact, the physical properties of the different synovial fluids mentioned in the last chapter, including their surface tension and viscosity are correlated with the wear depth of the additive manufactured Ti-6Al-4V samples. Also the purpose of this chapter is to analyze and compare the wear response of EBM-x and EBM-z samples, and to study their anisotropic effects.

The increase in concentration of BSA in the synovial fluid resulted in better lubrication and lesser wear. Which could be related to better wettability of high protein synovial fluid due to lesser surface tension and also better lubrication due to high viscosity. Overall the EBM-x was observed to have a higher wear compared to EBM-z sample. This could be related to lesser modulus value of the EBM-x sample.

4.1 Introduction

4.1.1 Hip Joint

The hip is the body's second largest weight-bearing joint (after the knee). It is a ball and socket joint at the juncture of the leg and pelvis. The rounded head of the femur (thighbone) forms the ball, which fits into the acetabulum (a cup-shaped socket in the pelvis). Ligaments connect the ball to the socket and usually provide tremendous stability to the joint. The hip joint is normally very sturdy because of the fit between the femoral head and acetabulum as well as strong ligaments and muscles at the joint.

All of the various components of the hip mechanism assist in the mobility of the joint. Damage to any single component can negatively affect range of motion and ability to bear weight on the joint. Orthopedic degeneration or trauma – those conditions affecting the bones in the hip joint – can necessitate total hip replacement, partial hip replacement or hip resurfacing [23].

4.1.1.1 Hip joint replacement

In a hip replacement surgery, some damaged parts of the hip joint are replaced with artificial hip parts called an implant or prosthesis, a device that substitutes or supplements a joint. There are several conditions which can lead to chronic hip pain and disability, requiring hip replacement. The surgeon has to select the design of the hip replacement and size of femoral ball at the top to give the patient the range of motion and stability needed to function.

In a total hip replacement, also called total hip arthroplasty, both the thigh bone (femur) and the socket are replaced with implant prostheses. During the procedure the socket is

cleared of the worn cartilage and bone and a metal cup shaped shell put in its place. A liner is then inserted into this metal shell. A metal stem is inserted into the thighbone (femur). Attached to the neck of the stem is a hip ball (sizes vary from 28-58mm) which fits into the socket's liner. Together, the ball and liner create the new joint. In terms of fixation the hip implants could be fixed to the bone using either cement fixation or fixation by bone ingrowth [30].

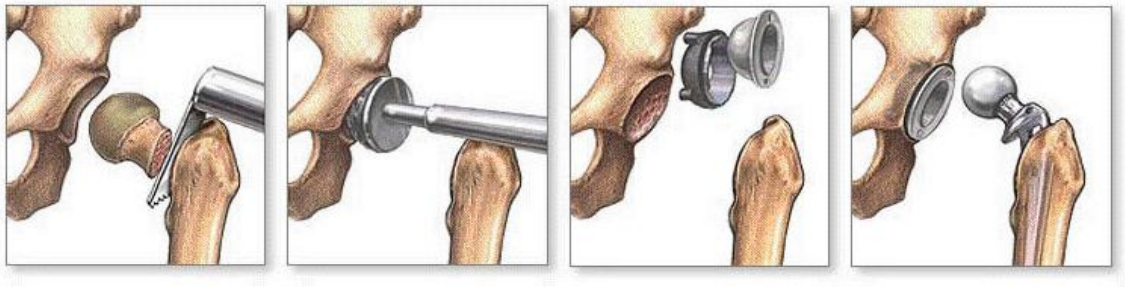

Figure 43: Total hip joint replacement [31]

4.1.1.2 Causes of hip joint replacement

The majority of hip replacement surgeries are necessitated by arthritis. The types of arthritis are given below:

(i) Osteoarthritis - it occurs when cartilage on the end of bone begins wearing away, causing pain and stiffness. When the cartilage wears away completely, the bones rub directly against each other causing decreased mobility and chronic pain. Osteoarthritis is most common in people 50 and older, but is also prevalent in those with a family history of arthritis or those with lifestyles that stress the hip joints, such as athletes and laborers.

(ii) Rheumatoid arthritis - it is an autoimmune disease in which the synovial membrane becomes inflamed. The membrane then produces too much synovial fluid, damaging the articular cartilage.

(iii) Traumatic arthritis - it results from a serious hip injury or fracture. The articular cartilage becomes damaged and, over time, causes hip pain and stiffness [24].

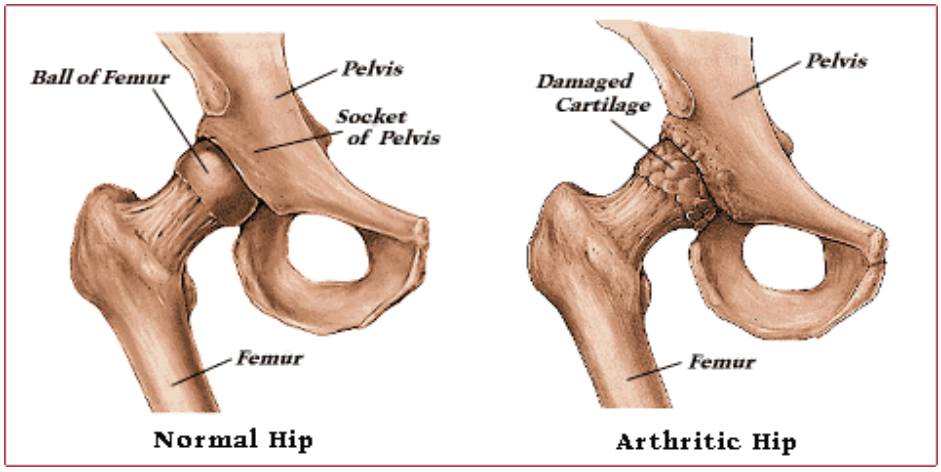

Figure 44: Normal Hip Joint vs. Arthritic Hip Joint [23]

4.1.1.3 Hip Implant materials

A total hip replacement replaces the arthritic hip joint and eliminates the damaged bearing surfaces that are causing pain. The design of the implant offers renewed stability and minimizes the wear process. The traditional metal and polyethylene implants have been in use since the 1960's but technological advances since then have made other materials such as ceramic increasingly popular [32].

One of most common problems with replacement hips is the wear and tear that takes place through normal use. Depending on the specifics of the patient's situation (age, weight, height, level of activity etc.), the hip replacement implant may be made of metal, polyethylene (plastic) or ceramic. For example, for a very active individual or a relatively young patient an all-ceramic hip joint or all metal hip joint would be preferred [32].

Overall the hip implants fall into the following four basic material categories [33]:

4.1.1.3.1 Metal-on-plastic

Metal-on-plastic (polyethylene) is the longest tried and tested bearing. The convex femoral stem is constructed of metal (usually a titanium or cobalt chrome alloy) and the concave cup liner is made of a plastic called polyethylene. The current plastic used in hip replacement implants is referred to as Ultra Highly Cross-Linked Polyethylene (UHXLPE) or Ultra High Molecular Weight Polyethylene (UHMWPE), a very stable and reliable plastic material with greatly reduced risk for wear.

Because of its durability and performance, metal-on-polyethylene has been the leading artificial hip component material chosen by surgeons since hip replacement surgeries were first been performed. It is also the least expensive bearing.

All implants shed debris as they wear. Over time, the body may see polyethylene wear particles as invaders or a source of infection. As the body starts to attack them, this leads to osteolysis, a "dissolving of the bone", which may result in having to replace the implant.

4.1.1.3.2 Metal-on-metal

Metal-on-metal bearings (cobalt chromium alloy, titanium alloy or sometimes stainless steel) were in use from as far back as 1955 though they were not approved for use in the U.S. by the FDA until 1999. They offer the potential for greatly reduced wear, with less inflammation and less bone loss. Some device recalls have brought negative attention to metal-on-metal.

Metal bearings are available in many sizes (28 mm to 60 mm); there are also several neck lengths available. Only metal-on-metal components allow the largest heads throughout the entire range of implant sizes. Large ball heads provide increased range of motion and greater stability, which can significantly reduce the risk of hip dislocation, a crucial factor in the long term success of an implant.

Because the human femoral head is naturally large, it makes sense to implant a large, anatomic replacement. This was not possible in the past because traditional design parameters made smaller femoral heads necessary. However, with the introduction of metal-on-metal implant components, liners may be eliminated, allowing surgeons to use large femoral heads [33].

Metal-on-metal implants have a potential wear rate of about 0.01 millimeters each year. Although wear is reduced with metal-on-metal implants, the wear products including sub-microscopic particulates, soluble metal ions are distributed throughout the body. This has raised concerns about long-term bio-compatibility. In 2011, the FDA issued a communication regarding metal-on-metal implants, indicating some concern and need for

further study or review. Some metal-on-metal hip implants have been recalled by their manufacturers [33].

4.1.1.3.3 Ceramic-on-ceramic

Ceramic is the latest material used for hip replacement as it is both hard and durable, it wears minimally and the material is widely deemed to have no toxic or side effects in the human body. However, two issues with ceramic hip replacement observed are catastrophic shattering and squeaking. Shattering is because of poor ductility of ceramics.

Ceramic is the hardest implant material used in the body, and has the lowest wear rate of all, to almost immeasurable amounts (1000 times less than Metal-on-polyethylene, about 0.0001 millimeters each year). Consequently, there is usually no inflammation or bone loss, nor systemic distribution of wear products in the body. New ceramics offer improved strength and more versatile sizing options [33].

4.1.1.3.4 Ceramic-on-plastic (UHMWPE)

Ceramic-on-UHMWPE (Ultra High Molecular Weight Polyethylene) is a good combination of two very reliable materials. Ceramic heads are harder than metal and are the most scratch-resistant implant material. The hard, ultra-smooth surface can greatly reduce the wear rate on the polyethylene bearing. The potential wear rate for this type of implant is less than metal-on-plastic.

Ceramic-on-polyethylene is more expensive than metal-on-polyethylene, but less than Ceramic-on-Ceramic. In the past, there had been incidents of fractures in ceramic

components, but newer, stronger ceramics have resulted in considerable reduction of fracture rates (0.01%) compared to the original, more brittle ceramics [33].

Ceramic-on-polyethylene implants have a potential wear at a rate of about 0.05 millimeters each year, i.e. 50% less than metal-on-polyethylene. The newer, highly cross linked polyethylene liners have shown potential wear rates as little as 0.01 millimeters each year.

4.1.1.4 Adverse effects of total hip replacement

The main issue that doctors and patients confront when choosing implant material revolves around the wear debris that is released into the body from any of the implant materials. Wear and fretting corrosion in the artificial joint result in the formation of soluble and particulate debris that can migrate in locally or systemically and may induce a cascade of inflammatory events that may ultimately result in bone loss by osteolysis and subsequent implant failure.

With metal implants, there has been some concern that, when the metal parts rub on each other, small bits of metal are shed into the joint space and bloodstream, causing inflammation and other problems. Metal ion release is an electrochemical process; generally denoted as corrosion which is a serious problem for medical metallic materials. For joint replacements, they perform under tribological contacts and load. Their performance (long-term durability) relies on both their corrosion resistance and wear resistance. Corrosion accelerates the wear rate and vice versa in many industries [34].

After the initiation of substantial litigation and media attention, in May 2011, the U.S. Food and Drug Administration (FDA) asked for increased monitoring of all 22 commercially available metal-on-metal hip implant replacement systems. The purpose of this post-

market surveillance was to determine the true likelihood of loosening of the joint, local inflammation caused by the implant, and the dangers of the release of metal ions into the bloodstream [33].

For ceramic implants the cases of catastrophic shattering and squeaking are observed. Shattering is because of poor ductility of ceramics and squeaking is caused by the noise. The poor ductility makes the implant liable to cracking when undergone sudden blow or impact. Also sometimes the noises abate over time but sometimes they don't, making the squeaking intolerable [33].

The adverse tissue reaction lowers pH level and increase protein concentration in the synovial fluid, making the joint fluid unhealthy. That can further accelerate the corrosion and affect the lubrication of the synovial fluid and weaken the immunological reaction. The joint fluid needs to be analyzed for that. Synovial fluid analysis consists of a group of tests that detect synovial fluid changes and may indicate the presence of diseases affecting joint structure and function. It includes the following tests [25]:

- Physical examination (e.g., appearance, to include color, viscosity, other physical characteristics)
- Chemical analysis (eg, glucose, total protein level, pH level)
- Microscopic evaluation (eg, cell count and differential count, crystal identification)
- Infectious disease tests—detect and identify microbes, if present

4.1.2 Wear Testing

Wear is the most important factor in the damage of hip joint replacements. The tribological effects on the materials are analyzed for their wear damage in different conditions. Wear is caused by the relative motion between two or more surfaces that are in close contact, causing deformation or removal of the material. Wear can also be caused by other sources such as harsh or reactive chemicals, or cavitation.

There are different types of wears based on the materials, type of motion and other factors. The types and effects of wear important for the research are discussed below.

4.1.2.1 Abrasive Wear

Abrasive wear occurs when a surface slides over another surface. One of the surfaces is mostly a hard surface and the other is soft. It results in a loss of material from the softer surface. Three body abrasive wear also occurs when there are particles between the sliding surfaces. The abrasive wear occurs in several processes.

- Plowing
- Microfatigue
- Wedge
- Microcracking
- Cutting

4.1.2.2 Fretting Wear

Fretting is the small amplitude oscillatory motion that occurs between two contacting surfaces. The motion is mostly due to one of the members being subjected to a cyclic stress, called fatigue. One of the immediate consequences is the production of oxide debris. This gives rise to fretting wear and fretting corrosion.

The phenomenon of fretting arises from the vibratory motion which produces alternating stress mostly the problem is of fatigue than wear. However, if the contact pressure between the bodies is not high then the major issue is fretting wear. It is really significant in case of metal-on-metal hip joint implants. Fretting occurs between the acetabular cup and the femoral head. It disrupts the protective layer releasing the metal ions into the body fluids particularly synovial joint fluid. This initiates the immunological reactions in the body disturbing the concentration of the fluids which tends to have adverse effects on the joints. Also the damage caused to the prostheses surface starts fretting corrosion which reduces the life of the implants.

4.1.2.3 Wear Damage

The following parameters affect the wear damage.

- Normal Load
- Amplitude of motion
- Speed of motion
- Contact type

- Material properties
- Surface finish
- Environment

So the above mentioned parameters make it crucial that the most appropriate material and size is selected for the hip implants. The size of the joint is determined on the basis of the patient's needs. It includes the weight and the level of activity as the basic parameters. These parameters affect the load and the motion of the joint which greatly affect the wear damage in the implants. This is one of the reasons that metals are a good material for conditions with wear, as they offer good strength and also their properties could be changed as needed by heating or by mixing with other metals, making alloys. The mechanical properties that show a correlation with the wear include the hardness, elastic modulus, yield strength. As these properties increase the wear rate is seen to decrease.

Wear also produces debris in the wear process. There is a lot of research being done to study the debris since it has both chemical and mechanical effects on the materials. It can build up between the sliding surfaces and increase the number of interfaces from one to two, causing more wear damage [53].

The environment or medium between the sliding materials also greatly affects the wear. This is due to the friction and corrosion effects. In dry conditions there is lesser lubrication causing more friction between the sliding materials, however the corrosion effect is lesser. In any wet or humid conditions, the friction is reduced but the corrosion effects are more significant. Therefore, it is critical to analyze the wear in both dry and different wet conditions.

4.1.2.4 *Measurement of Wear Damage*

There are several ways to measure the wear damage. Some are given below [54].

- Profilometry
- Holographic Interferometry
- Thin-layer Activation
- Measurement of Axial Distance

Optical profilometry was used in the research since the wear tests were performed at a micro-scale. The traditional ways to determine the wear by measuring the weight loss are not practical for the teste performed in the research. In profilometry the surface is surveyed using an optical instrument which plots out a projection of the surface and the computer the figure for the wear. Using the software, the wear parameters are calculated. These parameters include the wear depth, length and the volume. This method is also useful for scanning the surfaces before the wear tests. That helps to determine the surface parameters including the flatness or roughness.

4.1.2.5 *Corrosion*

The surface damage caused by wear tends to increase the corrosive effects. This is significant in case of metals in a wet medium, where the wear damages the oxide layer which exposes the fresh metal to the liquid which corrodes further metal. Also the corrosive conditions formed on the surface enhance the abrasive wear, so this creates a synergism between the wear rate and the corrosion. It was observed by Madsen that the synergism of wear and a corrosive component could be twice of their individual components added

together [55]. So It shows that the corrosive effects of wear are also significantly important. Especially in case of hip implants.

4.2 Materials and Methods

To simulate the wear of a femoral head inside the acetabular cup a pin on disk wear test was performed. It was done using the same Nanovea M1 Nanoindenter with a spherical Tungsten Carbide (WC) indenter with diameter of 3mm. The rotational motion of the indenter in the pin on disk test on the Ti-6Al-4V samples was the analogous of the joint motion of the femoral head after hip joint replacement. The wear test was performed on both the EBM-x and EBM-z samples in the following conditions.

i. Dry test

ii. Wet test

   a. PBS solution

   b. PBS + C1

   c. PBS + C2

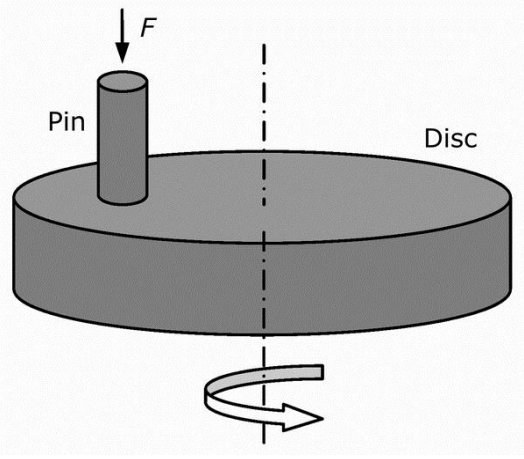

Figure 45: Pin on disk wear test schematic

The actual contact between the femoral head and acetabulum is a surface to surface contact but it could be taken as a point to surface contact for the test. At macroscopic level the surface contact seems a continuous contact but at a micro or nano scale it is just a multi asperity contact, which is a combination of several single asperity contact [44]. That is because there is always some non-zero average roughness value of every surface. This roughness prevents any continuous contact and thus it could be replicated as a single asperity contact as in a point contact. This is explained in the following image:

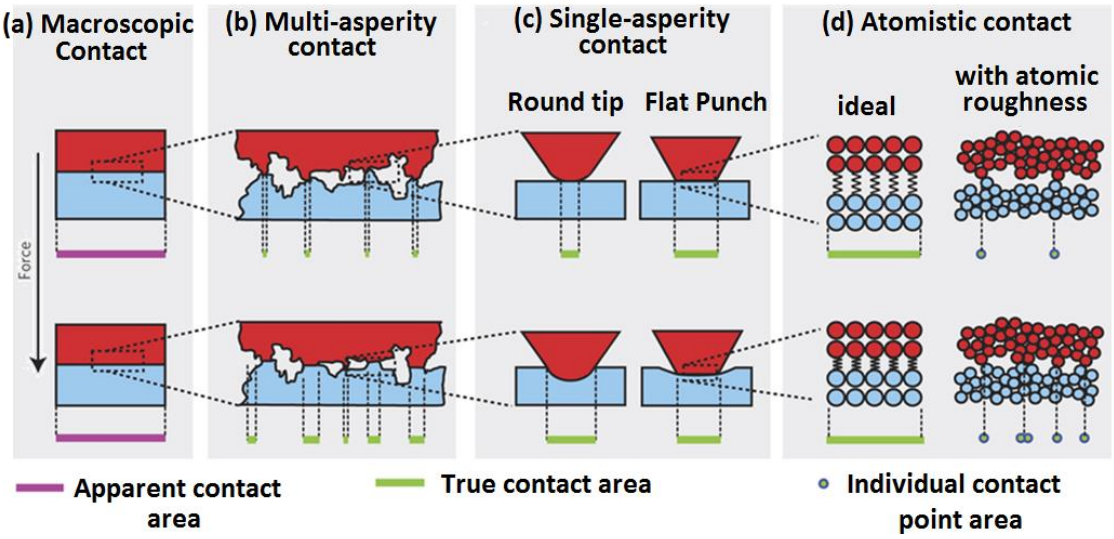

Figure 46: Contact models for macro and nano scale bodies [44]

The indenter contact with a surface is similarly a single asperity contact at a nanoscale as shown in the figure below.

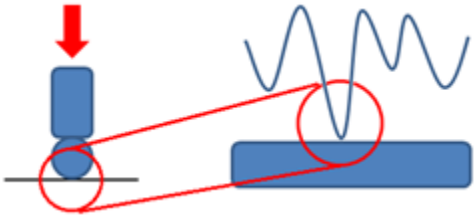

Figure 47: Spherical indenter contact

The pin on disk wear test was completed in the following steps:

4.2.1 Calculation of test parameters

The test parameters for the wear test are given in the following table

Table 14: Pin on disk test parameters

Parameter	Value
Indenter	Tungsten Carbide (WC)
Indenter diameter	3 mm
Load	30 mN
Test radius	1 mm
Test speed	60 rpm
Test duration	30 min

The test load was determined from the Hertzian Elastic Contact Theory using the case of a sphere on a flat surface. The stress values produced in the sample, by the contact of the spherical indenter were calculated for a set of loading values and the load for which the stress value was around 30% of the yield strength of the sample was chosen for the test load. The stress distribution in a typical Hertzian contact is showin below

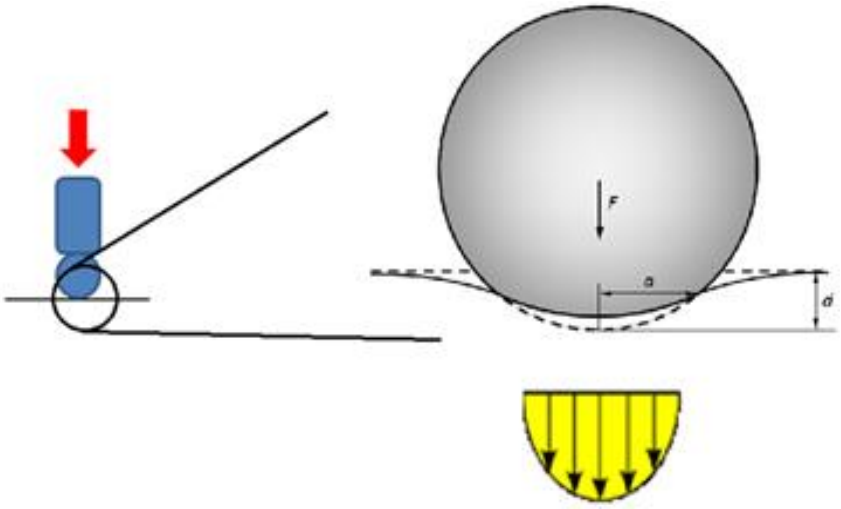

Figure 48: Hertzian contact stress

The equations are as follows [46]:

$$\text{Elastic contact radius, } a = \sqrt[3]{\frac{3\,F\,R}{4\,E^*}} \tag{28}$$

$$\text{Maximum pressure} = P_{max} = \frac{3\,F}{2\,\pi\,a^2} \tag{29}$$

$$\frac{1}{E^*} = \frac{1-{v_i}^2}{E_i} + \frac{1-{v_s}^2}{E_s} \tag{30}$$

Where R is the indenter radius, R= 1.5 mm

E_i and ν_i are the indenter elastic modulus and Poisson ratio respectively E_i = 640 GPa , ν_i = 0.21

E_s and ν_s are the sample elastic modulus and Poisson ratio respectively E_s = 120 GPa, ν_s = 0.3

The iterative calculation for the maximum contact stress using different load values is shown in the Table 6 below.

Table 15: Wear test load calculation

F (mN)		a (mm)	Max Cont Pressure (Mpa) (center)	Yield %
10		0.004667779	219.1395399	21.590102
20		0.005881033	276.0985191	27.201825
30		0.006732103	316.0539072	31.138316
40		0.007409638	347.8623361	34.272151
50		0.00798179	374.7233421	36.918556
60		0.008481918	398.2029706	39.23182
70		0.008929141	419.1988592	41.30038
80		0.009335559	438.2790797	43.180205

Based on the calculation in the table above, a load of 30mN was selected for the pin on disk wear test. It was chosen to keep the maximum stress value close to 30% of the yield stress and the safety factor at around 3.

To determine the test speed, the gait of an average patient with a hip replacement was analyzed. The basic gait parameters most frequently used are velocity, step length, and step

frequency. The flexion of the hip, knee and ankle joints in the stance and swing phases of a usual gait are given in the image below [45].

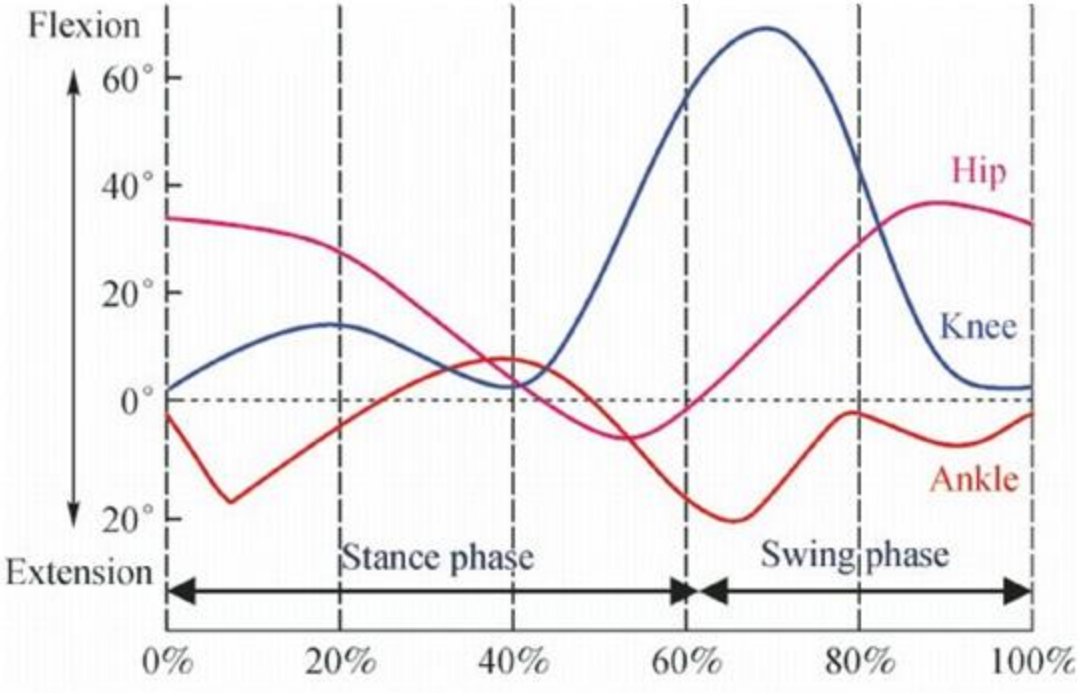

Figure 49: Sagittal-plane motion of lower extremity during one gait cycle [45]

The test radius and speed were determined for the following gait parameters after hip replacement:

Step angle = 40°

Step time = 1 sec

Femoral Head size = 25 mm

Femoral Head speed = 17.44 mm/s

For

Test radius = 1mm

Test speed = 60 rpm

Test duration = 30 min

4.2.2 Metallographic specimen preparation

The samples were cut into smaller cubes of 15mm x 15mm x 10mm. After that the samples were prepared for testing by metallographic sample preparation [37]. It was done by grinding and polishing the samples on a Planopol-2 polishing table using different grade polishing papers.

The process started with rough polishing with a 180 grit paper to make the surface flatter and then with 320, 800, 1000, 2400 and 4000 grit papers. During the polishing the samples were rotated 90^{o} to remove the scratches produced during the polishing to achieve a near mirror finish. After that final polishing was done using Chemomet micro fiber with 0.05 µm silica suspension. In the end the samples were cleaned with chemicals. The samples were thoroughly cleaned using acetone, methanol and distilled water to clear the surface from the residues. After finalizing the sample surfaces, they were inspected under a microscope before performing the tests.

4.2.3 Pre-test scan

Before the test the sample and the indenter were scanned using optical profileometer connected to the Nanovea M1 Nanoindenter. The profilometer used was a 300 µm range optical pen. The surface roughness was analyzed for both the sample and the spherical

indenter. Also the radius of curvature was calculated for the indenter. It was done to inspect the indenter after every wear test performed to make sure the indenter has a smooth surface finish for every test, replacing the indenter whenever needed.

The initial scans revealed the average roughness values of 0.012 µm and 0.005 µm for the sample surface and the indenter surface respectively. Also the radius of curvature was measured to be 1.5mm for the indenter before the tests.

4.2.4 Test performance

After the pre scan of the sample and the indenter ball, the wear tests were performed. The tests were performed on the same Nanovea M1 Nanoindenter using RS-0105 Rotary Stage according to ASTM G 99 and ASTM G 133 standards.

For both the EBM-x and EBM-z samples there were 4 type of wear tests performed with the test parameters mentioned in Table 5. The indenter used was 3mm diameter spherical Tungsten Carbide (WC). First was the dry test without any fluid lubricant. After that the 3 wet tests were performed with the fluid mentioned earlier. For each type there were 6 tests performed to get an accurate result regarding wear of the samples.

The samples were cleaned with acetone, methanol and then with distilled water after every wear test performed. Also for the wet tests the fluid was changed with fresh fluid after every 30min wear test performed.

4.2.5 Post-test scans

After the tests there were line scans performed on the samples and the indenter. The indenter was observed to wear significantly after every 2 tests so it was changed

accordingly. The roughness value measured for it was 0.021 µm with the radius of curvature as 4.3 mm after every 2 wear tests. On the samples the line scans were performed to determine the wear profiles and depths. To see the anisotropic effects (in the EBM-x sample) there were tests performed at both lateral and longitudinal points named as A and B as shown in the following image.

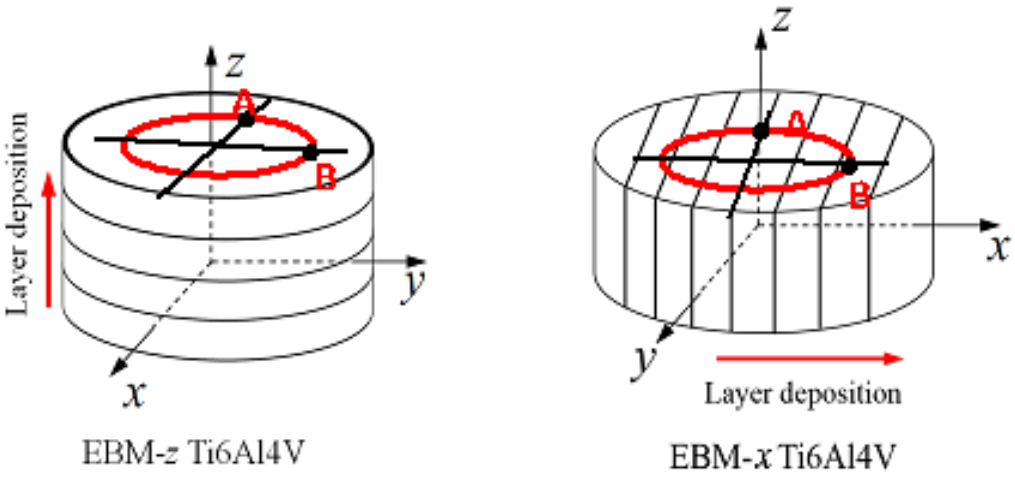

Figure 50: Post-test samples and scan points

The wear profiles were measured at both A and B on both the EBM-x and EBM-z samples for all the tests performed. The measured data was used to compare the wear rates for both the samples. The wear depths were then used to understand and explain the tribological response of the two samples. Also the wear depths were used to correlate the wear with the test conditions including dry and wet. And the impact of different lubrication fluids was observed on the wear of the samples on both the lateral and longitudinal points. The lubrication of the fluids was correlated with their surface tension and viscosity values to generalize their effects on the efficiency of lubricants.

4.3 Results and Discussion

Pin on disk wear tests were conducted on the Ti-6Al-4V samples. It was to analyze the tribological response of the additive manufactured samples and also to compare the anisotropic effects. The tests were performed under dry conditions and under the three synovial fluids prepared, constituting the wet tests. After completing the tests, the samples were scanned using optical profilometry. Line scans were made on the two points of the test to measure the wear depth for the test.

Also the tungsten carbide (WC) spherical indenter was scanned before the test and then after the tests to determine the surface roughness after every test. That was done to make sure the indenter is smooth enough for every test performed.

The wear was measured as the depth of the wear pattern formed on the sample surfaces after the tests. The digital surface data measured by the optical pen precisely determined the depth at the specified locations. After measuring the depths, it was correlated with the sample properties, their manufacturing parameters and the conditions of dry or wet test for the types of synovial fluids used.

The wear depths were measured at the following A and B points on both the EBM-x and EBM-z samples, as shown in figure 53.

4.3.1 Pre-test scans

After the preparation of sample surfaces for the wear tests, they were inspected under the microscope and the surface was scanned using optical profilometry to inspect for the surface finish and roughness. Also the WC indenter was scanned for its flatness and to compare the radius of curvature before and after the test. That was done in order to make sure the worn out indenter was changed whenever needed. The sample scan before the tests is shown below.

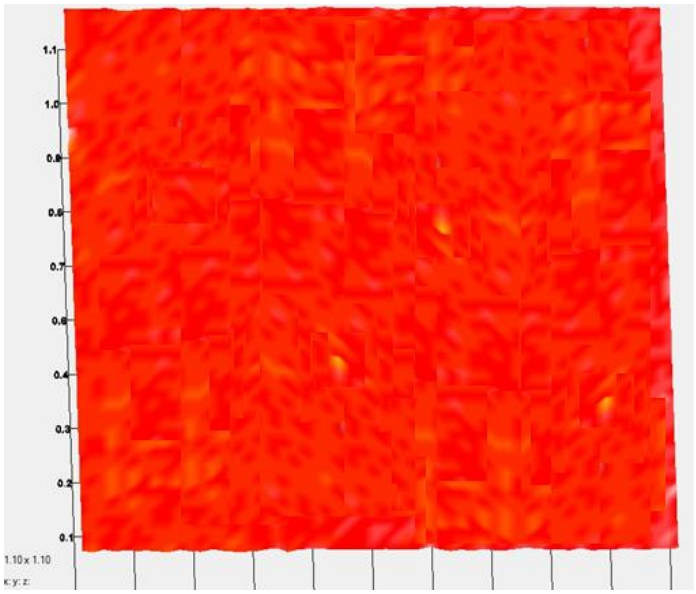

Figure 51: Pre-test sample surface scan

The roughness value before the scan was R_a = 0.012 µm. That shows a very smooth and flat surface after the metallographic sample preparation. The indenter was also scanned i.e. a line scan to find the radius of curvature of the spherical indenter. The roughness value for the indenter was R_a = 0.005 µm with the radius of curvature as 1.5 mm. That scan is shown below.

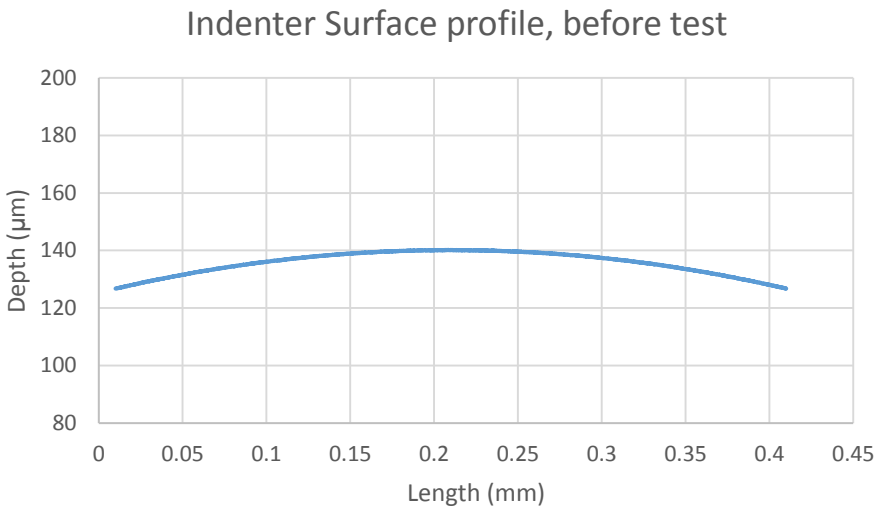

Figure 52: Indenter line scan before test

4.3.2 Post-test scans

After performing two tests the sample and the indenter were scanned again. The results were as follows

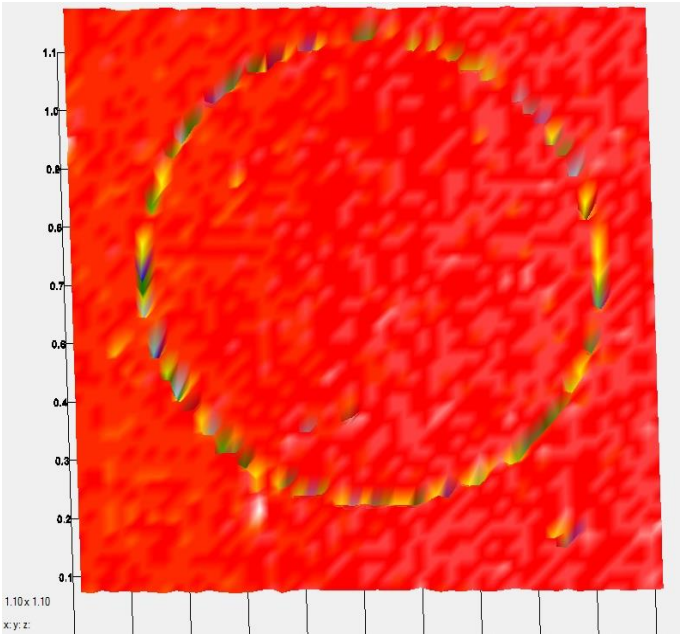

Figure 53: Post-test sample surface scan

The scan shows the pin on disk test performed on the sample. The indenter scan is as follows.

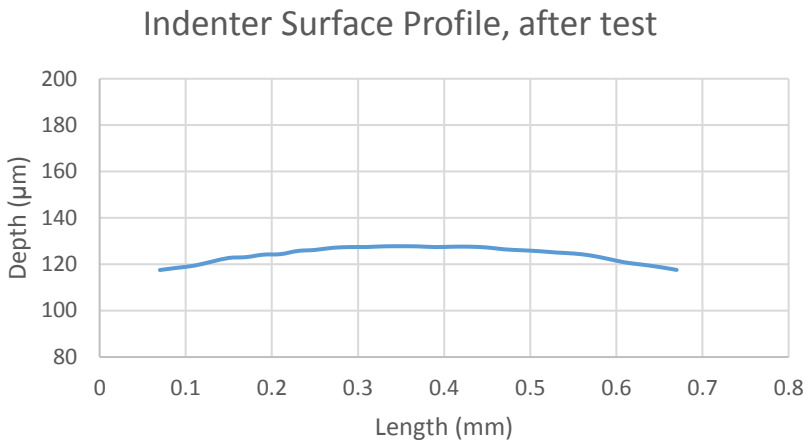

Figure 54: Indenter line scan after test

After the test the roughness value came was found to be R_a = 0.21 µm with the new radius of curvature as 4.3mm. After this the indenter was replaced with a new fresh indenter and that was repeated after every two tests.

Also the samples were scanned after the wear tests performed to measure their wear depths to analyze the overall wear. The wear tests gave the following wear profiles on the points A and B on the EBM-x sample.

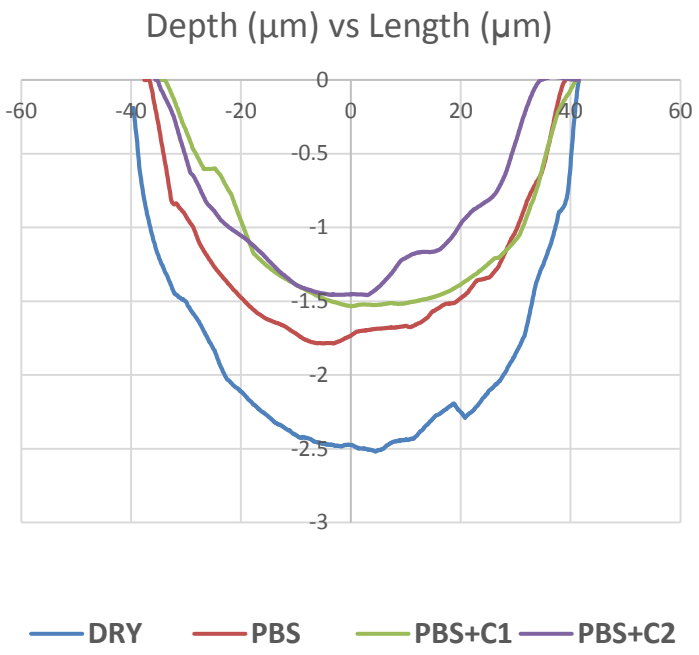

Figure 55: Wear profile EBM-x sample (point A)

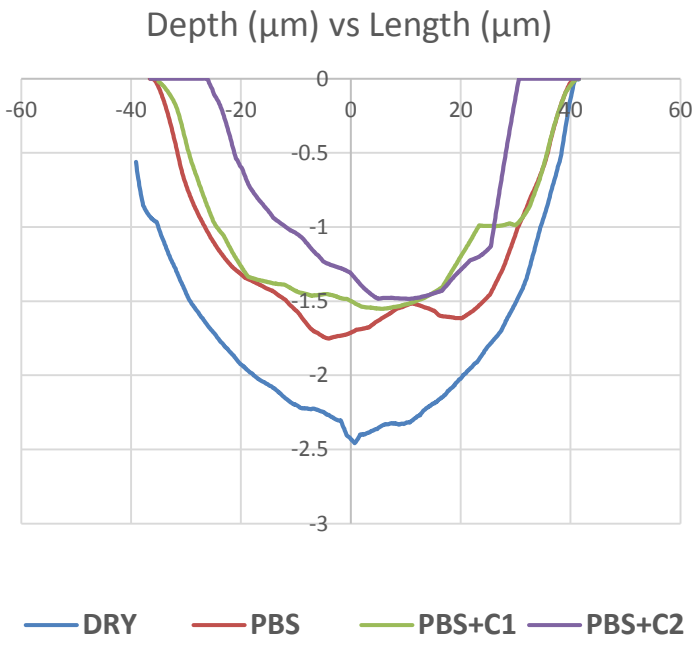

Figure 56: Wear profile EBM-x sample (point B)

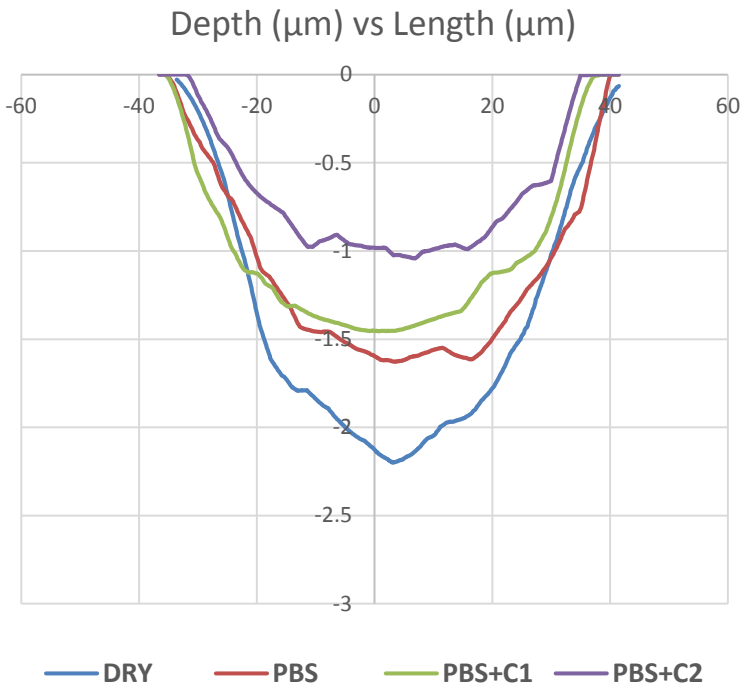

Figure 57: Wear profile EBM-z sample (point A)

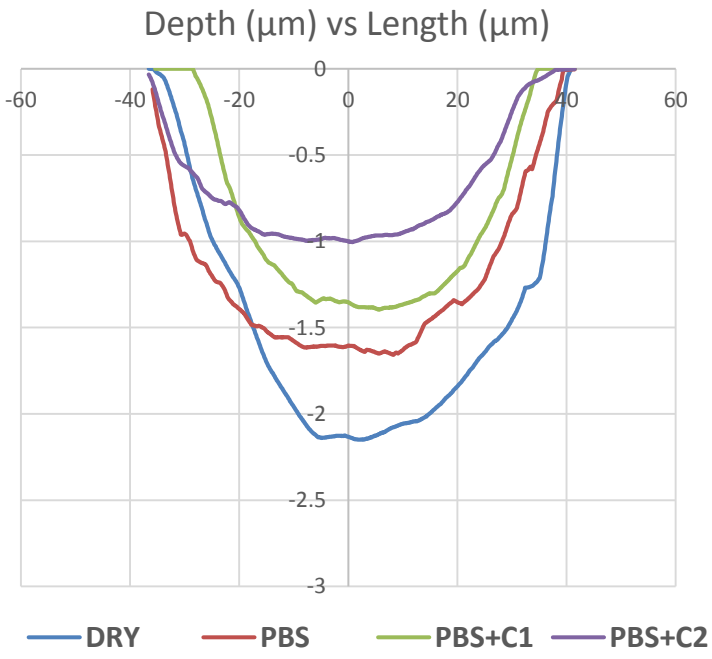

Figure 58: Wear profile EBM-z sample (point B)

The wear results in the last pages show that the highest wear was in the dry conditions for both the samples. That was expected since the lubrication is minimum in dry conditions. Overall a higher wear is seen in EBM-x samples. That is in accordance with the mechanical properties measured for that sample. The modulus of elasticity was measured to be higher for the EBM-z sample in all the three tests performed, the nanoindentation test, 4-point bending test and 3-point bending test.

The bar chart for the dry test is shown below.

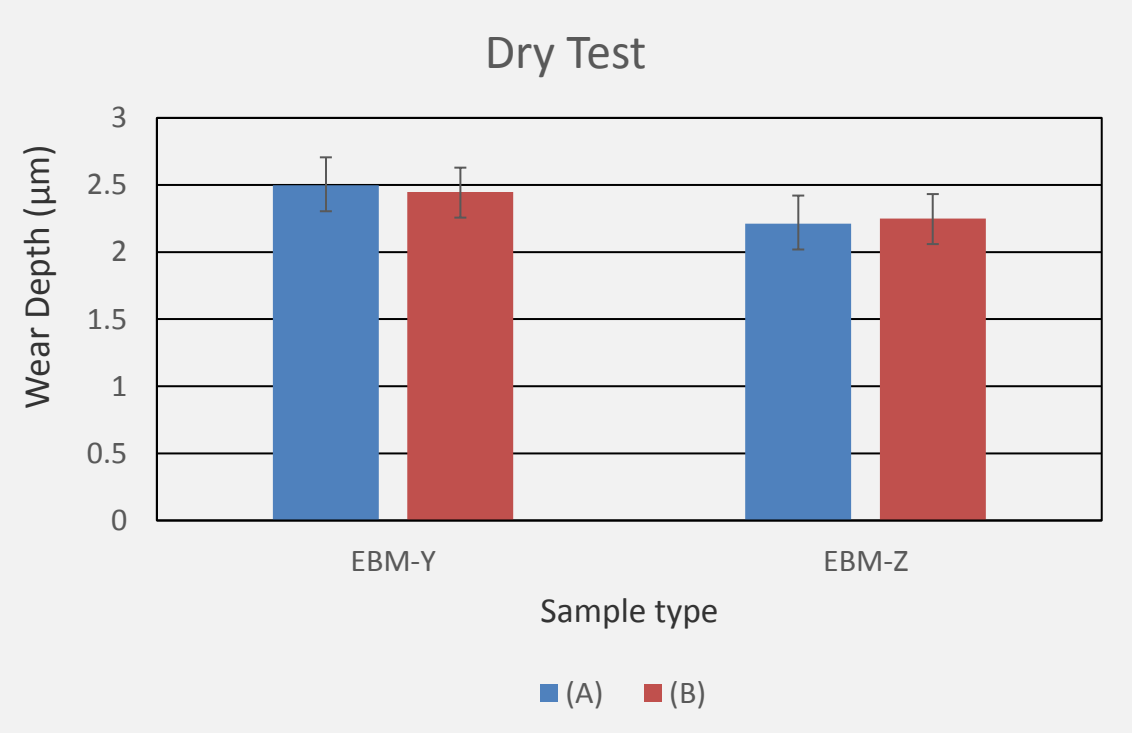

Figure 59: Wear depth for Dry tests EBM-x and EBM-z samples

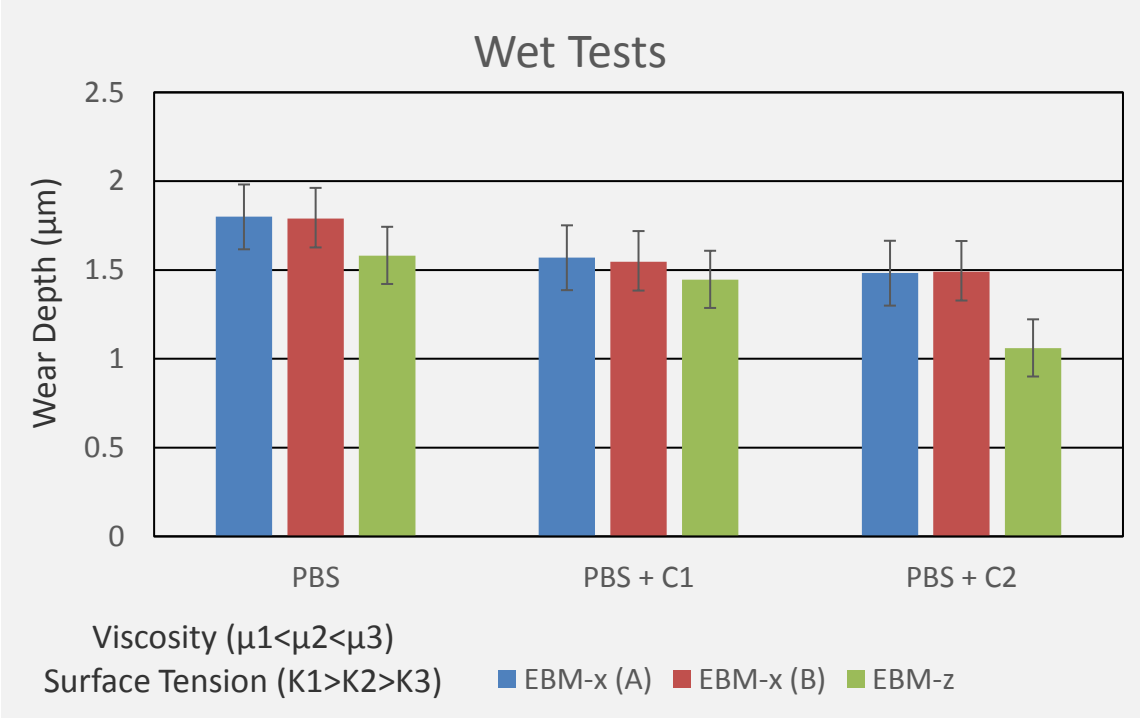

Figure 60: Wear depth for wet tests EBM-x and EBM-z samples

In the wet tests it is observed that the wear depth decreased with increase in the protein concentration in the synovial fluid, with the highest wear being in PBS. Regarding the physical quantities found earlier it was observed that as the surface tension of the fluid decreased the lubrication got better, in turn the wear decreased. For viscosity it was the opposite trend observed. The viscosity increased with the increase in the protein concentration and the wear decreased, making the lubrication better.

The anisotropic effects were, however not very clearly seen. For EBM-x sample the wear observed at the points A and B was not having significant difference to conclude any meaningful results.

4.3.3 Conclusion

Table 16: Wear depths for pin-on-disk test (µm)

Sample	**EBM-x**		**EBM-z**	
Point	A	B	A	B
Dry	-2.498 (+12.8%)	-2.447 (+8.75%)	-2.213	-2.25
PBS	-1.80 (+11.9%)	-1.79 (+14.7%)	-1.608	-1.56
PBS + C1	-1.57 (+8.8%)	-1.547 (+6.8%)	-1.443	-1.448
PBS + C2	-1.483 (+40%)	-1.491 (+54%)	-1.059	-0.965

The table above gives the comparison of the wear depth values for each test for both the lateral (A) and longitudinal points on the samples. It is seen that for the dry tests the wear in the EBM-x sample is observed to be an average 10.7% more than the EBM-z samples. In the PBS solution this wear is the highest, i.e. 13.3% higher. It is lowest in the PBS + C1 fluid i.e. 7.8% and then in the last case it is drastically high i.e. 47% high for EBM-x sample compared to EBM-z sample.

Overall it is seen that the addition of protein reduces the wear by a significant amount. Also the viscosity of the fluid is increasing so there is a good chance that the lubrication is entering the mixed lubrication from the boundary lubrication, decreasing the friction by a large part [49]. Which means that the fluid is being drawn in between the indenter and the sample surface and hence it is taking a part of the load showing fluid film lubrication, whereas the other part is taken by the asperity contact which shows boundary lubrication.

This effect is seen to increase as the protein concentration is increased meaning more part of the load is taken by the fluid, lowering the friction [49]. Another important part is being played by the surface tension, since it is observed to decrease with addition of BSA it can be improving the surface wettability, that draws more of the fluid between the indenter and the sample surface, which takes part of the load and reduces the friction [51]. Also the sample and indenter surfaces are pretty smooth which promotes more fluid-film lubrication and lesser boundary lubrication.

Chapter 5: Numerical model of spherical indentation on anisotropic surface

Abstract

The nanoindentation of a spherical rigid indenter on a surface has been simulated by finite element model. Models for both anisotropic and transversely isotropic samples were made to understand the stress distribution in the samples. The mechanical properties used were the same as determined through the mechanical testing in chapter 1. The models used were linear elastic models showing the depth and the stress only within the elastic range.

5.1 Introduction

Joints are the common regions for two bones in our body. They transmit motion and load when there is a motion. They have either a direct or an indirect contact based on the joint type. The load transmitted can be simulated as a contact problem to understand the stress profile and its distribution within the joints. Finite element analysis has been very popular in the contact mechanics problems. It is used to simulate the problem using linear or nonlinear models to analyze the elastic and plastic behavior of the materials. It gives the stress and depth within the materials based on the model type.

In this chapter the finite element model made for the spherical indentation on the sample surfaces is explained. To understand the effect of elastic contact stress on wear behavior, FEA models were created using ANSYS Workbench 17.1. The first model simulated a rigid spherical contact on perfect elastic isotropic surface as control. Averaged elastic modulus from moduli values in x, y and z direction found from the indentation and bending tests were used to characterize the contact surface. The second model was developed to

simulate contact problem on anisotropic surface (EBM-x). The third surface contact model aims to determine contact stress transversely isotropic surface (EBM-z). A series of contact simulations has been made on ANSYS Workbench. Each elastic modulus for x, y and z directions obtained from indentations and bending tests was used to formulate properties of respective EBM-z and EBM-x surfaces. Since the samples were made using EBM, they have directional properties for moduli and hardness. The results of the simulation gave the theoretical values for stresses established within the samples.

5.2 Description of Finite Element Model

In the end an FEA model was made for a contact problem having a sphere in contact with a flat surface. The model was made on ANSYS Workbench 17.1. This model was made to understand the stress distribution within the sample to better link it to the wear results observed in the pin-on-disk tests. Also the anisotropic effects were better understood with the model showing the displacement in the samples with anisotropic and transversely anisotropic properties.

5.2.1 Formulation of surface

The mechanical properties used were the average of the values determined from the mechanical tests performed earlier in the Chapter 2. The calculations are shown below.

Table 17: Mechanical Testing results

Test\Sample	(EBM-x)	(EBM-z)
	E (GPa)	E (GPa)
3 Point Bending	115.33	129.71
4 Point Bending	116.76	130.79
Nanoindentation	106.05	123.43

EBM-x sample

$$E = \frac{115.33 + 116.76 + 106.05}{3} = 112.71 \text{ GPa}$$

EBM-z sample

$$E = \frac{129.71 + 130.79 + 123.43}{3} = 118.07 \text{ GPa}$$

EBM-x sample

$$E_Y = E_Z = 112.71 \text{ GPa}$$

$$E_X = 127.98 \text{ GPa}$$

$$\nu_{YZ} = \nu_{ZY} = \nu_{YX} = \nu_{ZX} = 0.33$$

$$\nu_{XY} = \nu_{XZ} = \frac{127.98}{112.71} \text{ x } 0.33 = 0.374$$

$$G_{YZ} = G_{XY} = \frac{E_Y}{2(1 + \nu_{YZ/XY})} = \frac{112.71}{2\ (1 + 0.33)} = 42.37\text{GPa}$$

$$G_{XZ} = \frac{E_X}{2(1 + \nu_{YZ})} = \frac{127.98}{2\ (1 + 0.372)} = 46.64 \text{ GPa}$$

EBM-z sample

$$E_X = E_Y = 112.71 \text{ GPa}$$

$$E_Z = 127.98 \text{ GPa}$$

$$\nu_{XY} = \nu_{YX} = \nu_{YZ} = \nu_{XZ} = 0.33$$

$$\nu_{ZY} = \nu_{ZX} = \frac{127.98}{112.71} \text{ x } 0.33 = 0.374$$

$$G_{XY} = G_{XZ} = G_{YZ} = \frac{E_{X/Y}}{2(1 + \nu_{XY/XZ/YZ})} = \frac{112.71}{2\ (1 + 0.33)} = 42.37 \text{ GPa}$$

Using the above calculated values the stiffness and compliance matrices were made as follows.

EBM-x sample

$$\text{Compliance Matrix: } \begin{bmatrix} \frac{1}{127.98} & -\frac{0.33}{112.71} & -\frac{0.33}{112.71} & 0 & 0 & 0 \\ -\frac{0.374}{127.98} & \frac{1}{112.71} & -\frac{0.33}{112.71} & 0 & 0 & 0 \\ -\frac{0.374}{127.98} & -\frac{0.33}{112.71} & \frac{1}{112.71} & 0 & 0 & 0 \\ 0 & 0 & 0 & \frac{1}{2x42.37} & 0 & 0 \\ 0 & 0 & 0 & 0 & \frac{1}{2x46.64} & 0 \\ 0 & 0 & 0 & 0 & 0 & \frac{1}{2x42.37} \end{bmatrix} \frac{1}{\text{GPa}}$$

$$\text{Stiffness Matrix: } \begin{bmatrix} 202.26 & 99.26 & 99.26 & 0 & 0 & 0 \\ 99.26 & 175.15 & 90.33 & 0 & 0 & 0 \\ 99.26 & 90.33 & 175.15 & 0 & 0 & 0 \\ 0 & 0 & 0 & 84.74 & 0 & 0 \\ 0 & 0 & 0 & 0 & 93.28 & 0 \\ 0 & 0 & 0 & 0 & 0 & 84.74 \end{bmatrix} \text{GPa}$$

EBM-z sample

$$\text{Compliance Matrix: } \begin{bmatrix} \frac{1}{112.71} & -\frac{0.33}{112.71} & -\frac{0.374}{127.98} & 0 & 0 & 0 \\ -\frac{0.33}{112.71} & \frac{1}{112.71} & -\frac{0.374}{127.98} & 0 & 0 & 0 \\ -\frac{0.33}{112.71} & -\frac{0.33}{112.71} & \frac{1}{127.98} & 0 & 0 & 0 \\ 0 & 0 & 0 & \frac{1}{2x42.37} & 0 & 0 \\ 0 & 0 & 0 & 0 & \frac{1}{2x42.37} & 0 \\ 0 & 0 & 0 & 0 & 0 & \frac{1}{2x42.37} \end{bmatrix} \frac{1}{\text{GPa}}$$

$$\text{Stiffness Matrix: } \begin{bmatrix} 175.15 & 90.33 & 99.26 & 0 & 0 & 0 \\ 90.33 & 175.15 & 99.26 & 0 & 0 & 0 \\ 99.26 & 99.26 & 202.26 & 0 & 0 & 0 \\ 0 & 0 & 0 & 84.74 & 0 & 0 \\ 0 & 0 & 0 & 0 & 84.74 & 0 \\ 0 & 0 & 0 & 0 & 0 & 84.74 \end{bmatrix} \text{GPa}$$

5.2.2 Indentation Scheme

The following model was made in the ANSYS using the mechanical properties calculated above.

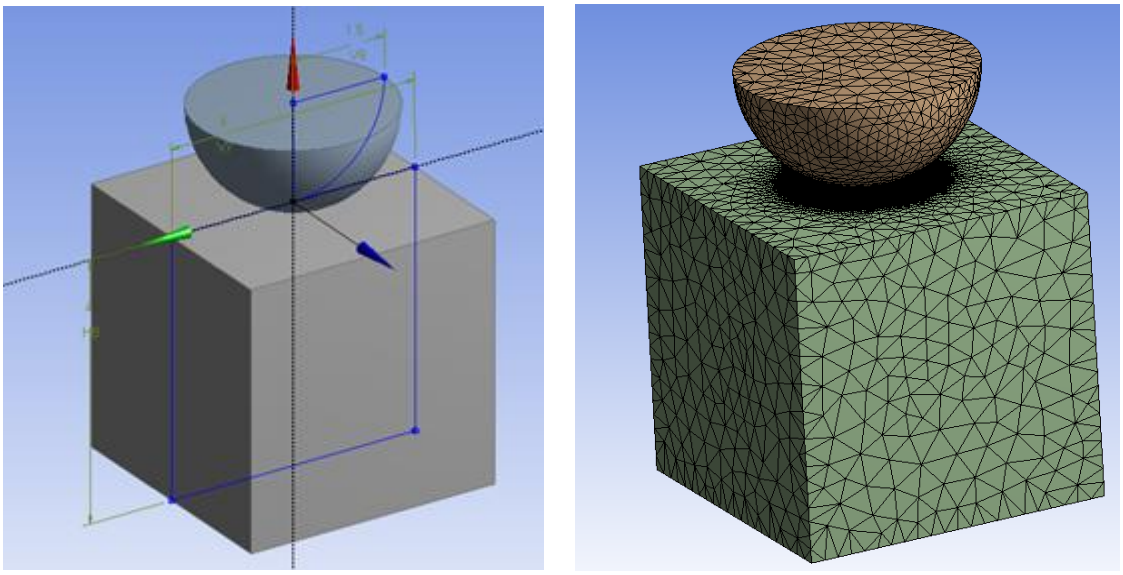

(a) **(b)**

Figure 61: FEA Model (a) overall, (b) with mesh

The following table shows the model parameters for the finite element analysis

Table 18: Model parameters

FEA Model Parameters	
Specimen Size	4 mm x 4 mm x 4 mm
Material	Ti-6Al-4V
Indenter Diameter	3 mm
Indenter Material	1.0 N
Normal Force	Tungsten Carbide (WC)
Number of Nodes	2938757
Number of Elements	2180491

Table 19: Mechanical properties for the model

	EBM-x	EBM-z	WC Indenter
Elastic Modulus (GPa)	$E_X = E_Y$ =112.71 E_Z = 127.98	$E_X = E_Z$ = 112.71 E_Y = 127.98	640
Yield Strength (MPa)	1042.2	981.51	-
Poisson ratio	$\nu_{XY} = \nu_{YZ} = \nu_{XZ}$ = 0.33	$\nu_{XZ} = \nu_{ZX} = \nu_{XY} = \nu_{ZY}$ = 0.33	0.21

Model Conditions

- The bottom surface of the sample is made fixed
- The indenter is made to move only in the vertical, z direction, fixing it in the x and y axes
- Bonded contact is used between the spherical indenter and the sample

5.3 Results and Discussion

The model gave the following results for the von Mises stress (MPa) distribution. The results were extracted at the points similar to the lateral (A) and longitudinal (B) points on the anisotropic sample (EBM-x).

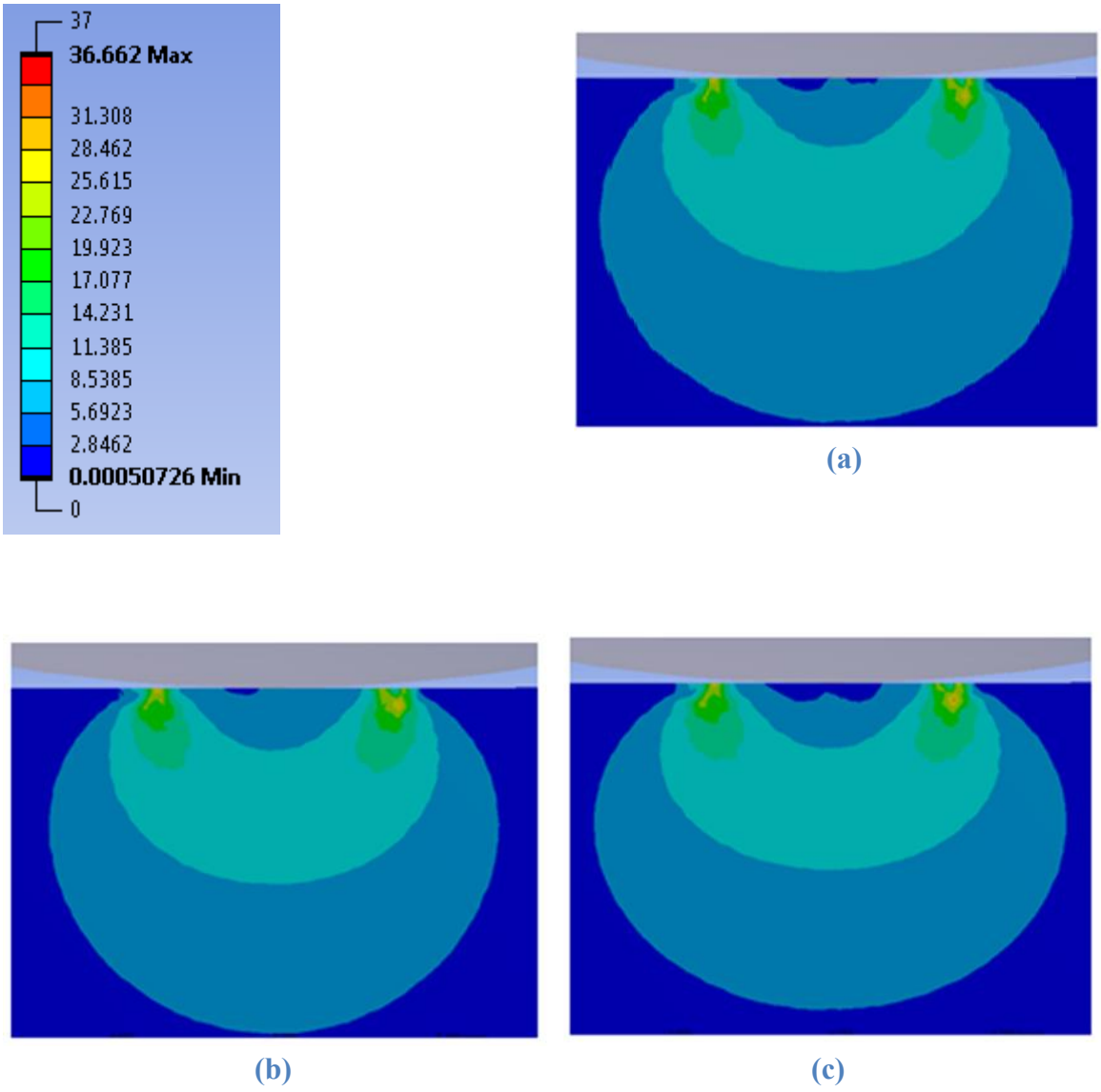

Figure 62: Von Mises stress distribution (a) EBM-x point A, (b) EBM-x point B, (c) EBM-z

The following results show the depth at the same points

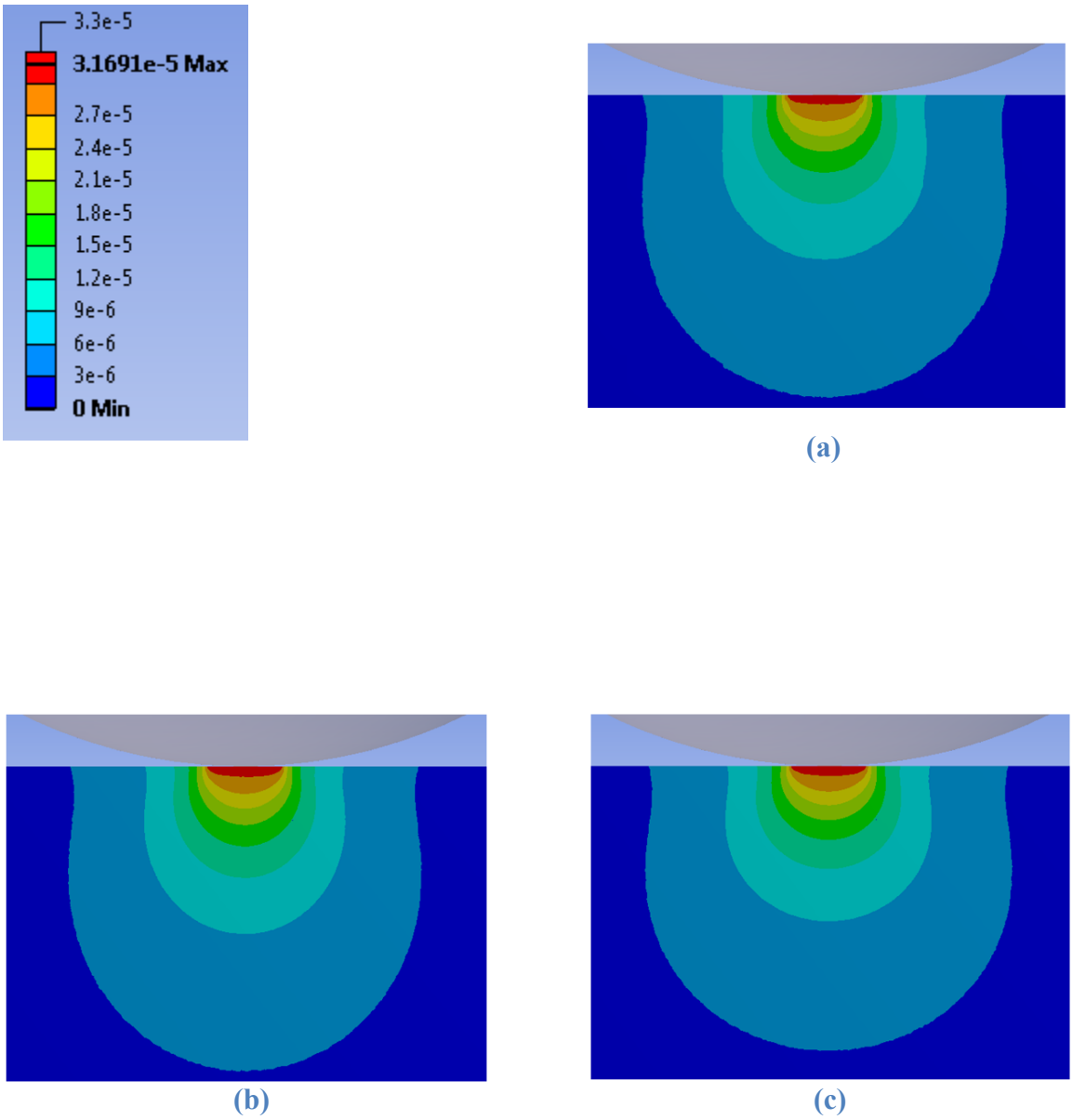

Figure 63: Von Mises stress distribution (a) EBM-x point A, (b) EBM-x point B, (c) EBM-z

Table 20: FEA results

	EBM-x (A)	EBM-x (B)	EBM-z
Max Stress (MPa)	36.62	36.62	32.41
Max Depth x 10^{-5} (mm)	3.169	3.169	2.804

The stress distribution in the EBM-z model is lesser deep due to higher modulus value in the vertical direction. That was also observed in the wear tests, seeing lesser depth for the EBM-z sample.

The wear test gave the following overall results for the wear depths in different test conditions for both the samples. The maximum depth values are given in the following table.

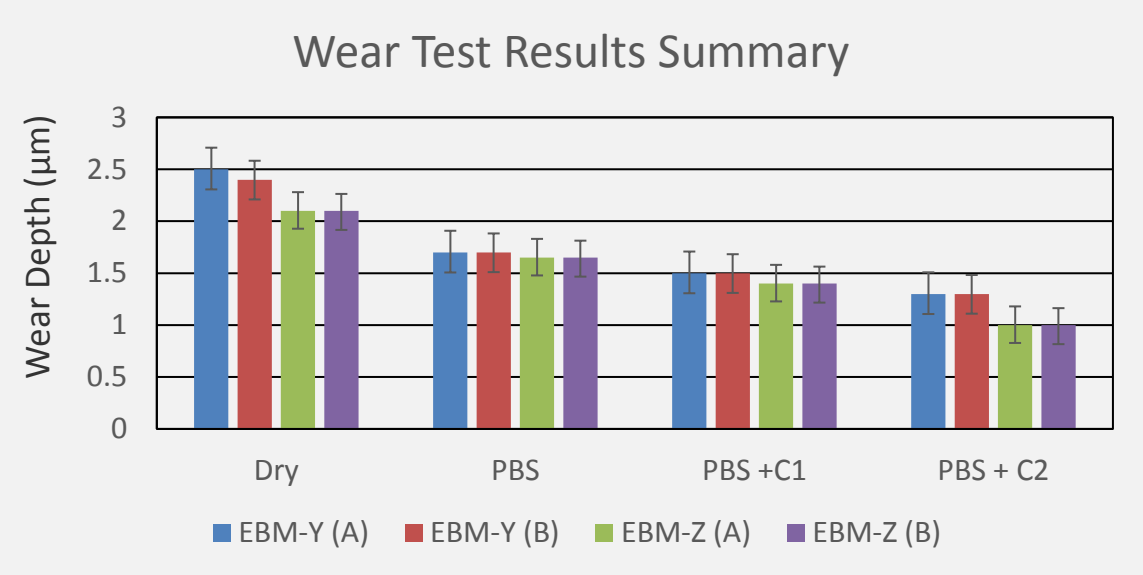

Figure 64: Wear test results summary

The results seen in the above figure can be correlated to the stress distribution observed in the FEA model. Showing the deepest stress in the EBM-x samples, which showed more wear in the test. The opposite is seen for the EBM-z sample.

Chapter4: Conclusions and Future Work

The purpose of the research was to determine the difference in the mechanical properties of the Ti-6Al-4V samples manufactured by additive manufactured in two different orientations and their wear response under different conditions of bodily synovial fluid. The parts were manufactured by EBM by Arcam EBM system. They were tested to determine their mechanical properties. The tests included nanoindentation, 4-point and 3-point bending setups. Then they were tested for wear response in three concentrations of human joint fluid. The wear results were then compared.

The mechanical properties were observed to be higher for EBM-z sample and so was the wear resistance, so it can be concluded that EBM-z could be better for bone replacement materials. Regarding the wear tests it had better wear resistance compared to EBM-x sample. However, the anisotropic effects were not very obvious in the EBM-x sample.

For the impact of the fluid concentration on the wear of the materials it was observed that high protein concentration proves to be better for lubrication of the joints and reducing the friction. That is the exact opposite of the expected results for the overall damage to the bones and hip replacement joint in the human body [33,34]. According to the reported behavior of the bones, when hip joint replacement is done (with particularly metal-on-metal joints) the articular cartilage reacts to the metal debris produced from the wear. This reaction involves an increase in the protein concentration of the synovial fluid. This increase is reported to be harmful to the bone and the joint, as it causes osteolysis. That causes damage to bone tissue and to the joint causes it to wear at a faster rate. But that seems to involve the chemical effects of the fluid on the implant materials. In the present research only the mechanical effects were taken into consideration. So a future work could

be recommended to analyze the chemical effects of the fluids in general and protein concentration in particular on the wear and corrosion of the implant materials such as Ti-6Al-4V.

References

1. Niinomi, M., *Mechanical properties of biomedical titanium alloys*, Department of Production Systems Engineering, Toyohashi Uni6ersity of Technology, 1 -1 Hibarigaoka, Tempaku-cho, Toyohashi 441, Japan, 1998
2. Facchini, L., *Microstructure and mechanical properties of Ti-6Al-4V produced by electron beam melting of pre-alloyed powders*, Department of Materials Engineering and Industrial Technologies, University of Trento, Trento, Italy, 2009
3. Khalid Rafi, H., Karthik, N.V., Thomas, L. Starr., Brent, E. Stucker., *Mechanical property evaluation of Ti-6Al-4V parts made using Electron Beam Melting*, Department of Industrial Engineering, Department of Chemical Engineering, J. B. Speed School of Engineering, University of Louisville, Louisville, KY, 2012
4. Schwerdtfeger, Jan, Robert F. Singer, and Carolin Körner. *In situ flaw detection by IR-imaging during electron beam melting*." Rapid Prototyping Journal 18, no. 4,(2012), pp: 259-263.
5. "Electron Beam Melting", *Powder bed fusion*, thre3d.com, Web https://thre3d.com/how-it-works/powder-bed-fusion/electron-beam-melting-ebm
6. Jacobs, Paul Francis, *Rapid Prototyping & Manufacturing: Fundamentals of Stereolithography.* Society of Manufacturing Engineers. ISBN, 1992
7. "Additive Manufacturing", *The basics*, Additivemanufacturing.com, Web http://additivemanufacturing.com/basics/
8. "Metal additive manufacturing processes", *Introduction to metal additive manufacturing and 3d printing*, Metal-am.com, Web

http://www.metal-am.com/introduction-to-metal-additive-manufacturing-and-3d-printing/metal-additive-manufacturing-processes/

9. "DMLS vs SLM 3D Printing for Metal Manufacturing", *Advanced Materials*, Element.com, Web https://www.element.com/nucleus/2016/06/29/dmls-vs-slm-3d-printing-for-metal-manufacturing
10. Tengvall, P., Lundstrom, I., *Physicochemical considerations of titanium as a biomaterial*. Clin. aterials, vol. 9, p. 115- 134, 1992
11. Mohsen, S., *Evaluation of Orientation Dependence of Fracture Toughness and Fatigue Crack Propagation Behavior of As-Deposited ARCAM EBM Ti-6Al-4V,* Department of Materials Science and EngineeringCase Western Reserve UniversityCleveland. USA, 2015
12. Khalid Rafi, H., *Defect formation in EBM parts built in horizontal orientation,* Department of Industrial Engineering, *Department of Chemical Engineering,
13. "Metal Additive Manufacturing", *A game changer for the manufacturing industry?*, sirris.com, Web sirris.com
14. Dowling, N.E., *Mechanical Behavior of Materials*, Third edition, Chap:5
15. Crips, F., "*Nanoindentation*", Mechanical Engineering Series, Third edition, 2011
16. Duanjie Li, *YIELD & TENSILE STRENGTH OF STEEL & ALUMINIUM USING MICROINDENTATION,* California, USA
17. Pierre Leroux , *An Indentation Test That Measures Yield Strength*, Nanovea, Irvine, California, USA, 2011

18. “How to Perform a 3 Point Bend Test on a Universal Testing Machine”, admet.com, Web *http://www.admet.com/how-to-perform-a-3-point-bend-test-on-a-universal-testing-machine/*
19. “Flexure test”, instron.us, Web http://www.instron.us/en-us/our-company/library/test-types/flexure-test
20. Christos C. Chamis, *ANALYSIS OF THE THREE-POINT-BEND TEST FOR MATERIALS WITH UNEQUAL TENSION AND COMPRESSION PROPERTIES*, Lewis Research Center Cleveland, Ohio, 1974
21. “File: Three point flexural test.jpg”, Three point flexural test, Wikipedia.org, Web https://en.wikipedia.org/wiki/File:Three_point_flexural_test.jpg
22. “Torsion test”, testresources.com, Web http://www.testresources.net/applications/by-test-type/torsion-test
23. “About the hip joint”, bonesmart.org, Web http://bonesmart.org/hip/about-the-hip-joint/
24. “Conditions leading to hip replacement surgery”, bonesmart.org, Web http://bonesmart.org/hip/conditions-leading-to-hip-replacement-surgery/
25. “Synovial Fluid Analysis”, labtestsonline.org, Web https://labtestsonline.org/understanding/analytes/synovial/tab/sample/
26. “Synovial Fluid Analysis of Hip Joint”, dovemed.com, Web http://www.dovemed.com/common-procedures/procedures-laboratory/synovial-fluid-analysis-hip-joint/

27. Bennike, T., *A Normative Study of the Synovial Fluid Proteome from Healthy Porcine Knee Joints,* Ugur, A., Haslauer, C.M, Froehlich, J.W., Proffen, B., Barnaby, O.S., Birkelund, S., Murray, M.M., Warman, M.L., Journal of Proteome Research. 13, 2014
28. Jay G.D., Waller, K.A., *The biology of Lubricin: Near Frictionless Joint Motion,* Matrix Biology 39, 2014
29. Edwards, J., *Normal Joint Structure*, Notes on Rheumatology. University College London, UK, 2012
30. "About Hip Replacement", bonesmart.org, Web http://bonesmart.org/hip/about-hip-replacement/
31. "Hip Joint Replacement", hendrick-medical.adam.com, Web http://hendrick-medical.adam.com/content.aspx?productId=26&pid=26&keyword=hip%20joint%20replacement&searchScope=Article&lang=en&count=20
32. "Total Hip Replacement", bonesmart.org, Web http://bonesmart.org/hip/total-hip-replacement-implants/
33. "Hip Replacement Implant Materials", bonesmart.org, Web http://bonesmart.org/hip/hip-replacement-implant-materials/
34. Yan, Y., *Tribo-corrosion properties of cobalt-based medical implant alloys in simulated biological environments*, School of Mechanical Engineering, University of Leeds, Leeds 2007
35. "Types of Wear in machines", xyobalancer.com, Web http://www.xyobalancer.com/xyo-balancer-blog/types-of-wear-in-machines

36. Arcam EBM system, *Ti6Al4V Titanium Alloy,* www.arcam.com

37. Zipperian, D.C., *Metallographic Specimen Preparation Basics,* Pace Technologies

38. Morris, D., Smith, D., *State of Standardization in Nanoindentation*, ASTM Strength and Fracture Standards at Micro and Nano Scales, National Institute of Standards and Technology, 2007

39. Bortel, E.L., *Development of a Synthetic Synovial Fluid for Tribological Testing,* Charbonnier, B., Heuberger, R., RMS Foundation, Switzerland, 2015

40. Roberts, J.C., *Development of a human cranial bone surrogate for impact studies,* Merkle, A.C., Carneal, C.M., Voo, L.M., Johannes, M.S., Paulson, J.M., Tankard, S., Uy, O.M., Applied Physics Laboratory, MD, USA, 2013

41. Kung, M.S., *The Synovial Lining and Synovial Fluid Properties after Joint Arthroplasty,* Markanronis, J., Nelson, S.D., Campbell, P., UCLA, California, 2015

42. Tang, B., Ngan, A.H.W., *Nanoindentation measurement of mechanical properties of soft solid covered by a thin liquid film*, Department of Mechanical Engineering, The Univeristy of Hong Kong, China, 2007

43. Paoli, D.F., *Measuring Polydimethylsiloxane (PDMS) Mechanical Properties Using Flat Punch Nanoindentation Focusing on Obtaining Full Contact,* University of South Florida, Florida, USA, 2015

44. Mo, Y., Szlufarska, I., *Nanoscale heat transfer: Single hot contacts*, Nature Materials, 2013

45. Luengas, L.A., *Modeling and simulation of normal and hemiparetic gait*, Camargo, W., Sanchez, G., Technological Faculty, Universidad Distrital Francisco José de Caldas, Bogotá, Colombia, 2015

46. Johnson, K.L., *Contact mechanics*, University of Cambridge, UK, 1985

47. Oberg, T., *Basic gait parameters: Reference data for normal subjects, 10-79 years of age*, Karsznia, A., Oberg, K., University College of Health Sciences, Jonkoping, Sweden, 1993

48. Wei, R., *On the Relationship Between Viscosity and Surface Tension,* Chen, J.H., Huizinga, J.D., Hillfield Strathallan College, Ontario, Canada, 2014

49. Curran, S., *Does surface wettability influence the friction and wear of large-diameter CoCrMo alloy hip resurfacings?,* Hoskin, T., Williams, S., Scholes, S.C., Kinbrum, A., Unsworth, A., Institution of Mechanical Engineering, Journal of Engineering in Medicine, 2013

50. Cooke, A.F., *The rheology of synovial fluid and synthetic lubricants for degenerate synovial joints,* Dowson, D., Wright, V., Engineering in Medicine 1978

51. Spikes HA. *The half-wetted bearing. Part 1 – extended Reynolds equation*, Proc IMechE, Part J: J Engineering Tribology 2003; 217: 1–14.

52. "2.5 Million Americans Living with an Artificial Hip, 4.7 Million with an Artificial Knee", aaos.org, Web http://newsroom.aaos.org/media-resources/Press-releases/25-million-americans-living-with-an-artificial-hip-47-million-with-an-artificial-knee.htm

53. Doget, M., *The Third Body Approach: Mechanical View of Wear*, Wear, Vol 100, 1984, p437 -452

54. ASM, "Friction, Lubrication and Wear technology", Waterhouse, R.B., University of Nottingham, UK, pp. 245-251

55. Levy, A.V., “The Platelet Mechanism of Erosion of Ductile Metals”, *Wear*, Vol 108, 1986, pp. 1-21